Identification of a
Lipid Oxygen Radical Defense pathway and its epigenetic control

Francisco S. Mesquita[1,3†*], Laurence Abrami[1†], Romain Forey[1], Béatrice Kunz[1], Charlène Raclot[1], Lucie Bracq[1], Filipe Martins[1], Danica Milovanovic[1], Evarist Planet[1,2], Olga Rosspopoff[1], Didier Trono[1], and F. Gisou van der Goot[1*]

[1]Global Health Institute, School of Life Sciences, EPFL, Lausanne

[2]Nexco Analytics, Epalinges, Switzerland

[3] Lee Kong Chian School of Medicine, Nanyang Technological University, Singapore, Singapore (present address)

†These authors contributed equally

*Corresponding Authors: F. Gisou van der Goot (gisou.vandergoot@epfl.ch), Francisco S. Mesquita (francisco.mesquita@epfl.ch) / (francisco.m@ntu.edu.sg)

Keywords: ZNF354A, ATF2, KAP1/TRIM28, GPX4, KRAB-zinc finger protein, Oxidative stress, Lipid Peroxidation, ferroptosis, ZDHHC20, NRF2.

ABSTRACT

Membrane phospholipids are vulnerable to oxidative radicals, and uncontrolled lipid peroxidation affects cell viability. Cells have evolved quality control and defense mechanisms, of which the genetic regulation is not fully understood. Here, we identify what we have coined the Lipid Oxygen Radical Defense (LORD) pathway. It is epigenetically repressed by a complex comprising the KRAB-zinc finger protein ZNF354A, the scaffold protein KAP1/TRIM28, the histone methyltransferase SETDB1, and the transcriptional activator ATF2. Upon lipid peroxide accumulation, p38- and JNK-dependent phosphorylation of ATF2, KAP1/TRIM28, and ZNF354A leads to disassembly of the repressive complex, releasing ZNF354A from specific DNA loci and activating a network of protective genes, including NRF2 targets. The pathway affects the cellular sensitivity to oxidative stress and ferroptosis, revealing a novel layer of epigenetic control in lipid quality control and damage repair. This positions the LORD pathway as a promising therapeutic target for diseases linked to chronic inflammation, neurodegeneration and cancer.

INTRODUCTION

Reactive oxygen species (ROS) are inevitable byproducts of aerobic metabolism [1,2]. These molecules play a dual role in cellular physiology: they are vital for signaling pathways [1,2], but excessive ROS accumulation leads to oxidative stress and cellular damage [1–3]. Elevated hydrogen peroxide (H_2O_2) levels can trigger Fenton reactions with transition metals, such as ferrous iron (Fe^{2+}), producing highly reactive hydroxyl radicals that inflict severe oxidative damage to biomolecules such as DNA, proteins, and lipids [1,2], particularly phospholipids containing polyunsaturated fatty acids (PUFAs) present in cellular membranes [4–6]. Accumulation of lipid peroxides and their deleterious by-products is a hallmark of oxytosis or ferroptosis, a non-apoptotic form of cell death increasingly recognized for its importance in aging, cancer, cardiovascular disease, neurodegeneration, and chronic inflammation [4,5,7–11]. Cells have evolved sophisticated antioxidant defense systems to protect against membrane lipid peroxidation, both selenium/thiol-dependent and independent pathways [7,9,12,13]. How these quality control mechanisms are regulated at a transcriptional level, particularly in complex organisms like mammals [14], is not fully understood, and is the focus of the present study.

A complex network of transcription factors coordinates oxidative stress responses, with NRF2 (NF-E2-related factor 2) as the principal regulator [2,9,14–16]. Controlled by the redox-sensitive cytoplasmic inhibitor Keap1, NRF2 binds to antioxidant response elements (ARE) in the 5′ UTR, driving the expression of antioxidant genes, xenobiotic transporters, and iron homeostasis regulators [15–18]. NRF2 controls various detoxification systems [7,15,17,19], including the thiol-independent oxidoreductase FSP1 (ferroptosis suppressor 1)[20–22] and factors required for glutathione (GSH) synthesis, such as SLC7A11, the cystine/glutamate antiporter crucial for cystine uptake [23,24]. GSH is essential for the activity of GPX4 (glutathione peroxidase-4), the primary enzyme that reduces lipid hydroperoxides[13,25]. GPX4 is regulated by NRF1, highlighting functional overlap among transcription factors while maintaining distinct cellular targets [26]. Other factors like NF-κB, HIF-1, FOXO1, p53, YAP/TAZ, and ATF4 are also involved in maintaining redox balance, influencing lipid peroxidation, inflammation, and hypoxia responses, ultimately affecting cellular sensitivity to oxidative stress [2,14,27–31]. Redox-

71 driven epigenetic modifications can further shape the expression of specific antioxidant
72 genes[32–34]. However, despite this wealth of information, major gaps in understanding the
73 transcriptional regulation of lipid quality control remain. The existence of a master regulator
74 remains uncertain, and the mechanisms controlling specific antioxidant gene programs are yet
75 to be elucidated.
76 In this study, we uncovered a defense pathway against ROS-triggered lipid damage, which we
77 have termed the LORD pathway, for Lipid Oxygen Radical Defense. This pathway is under
78 epigenetic regulation. DNA recognition is mediated by ZNF354A, a member of the largest
79 family of mammalian transcriptional modulators, the Krüppel-associated box (KRAB) domain
80 zinc finger proteins (KZFP) [35,36]. We found that ZNF354A is part of a repressive complex
81 containing the global repressor KAP1/TRIM28 (hereafter referred to as KAP1), the histone
82 methyltransferase SETDB1, but also the transcriptional activator ATF2, which plays a crucial
83 regulatory role. Under homeostatic conditions, the ZNF354A-containing complex represses
84 transcriptional programs involved in lipid quality control, antioxidant defenses, and other
85 response pathways. Accumulation of lipid peroxides leads to phosphorylation-dependent
86 disassembly of the repressive complex, and release of ZNF354A from specific DNA loci,
87 allowing activation of the antioxidant response pathway. This work highlights the
88 underexplored dynamics of epigenetic repressive complexes and the genetic response to
89 oxidative lipid damage. It also paves the way towards the identification of potential targets for
90 therapeutic intervention in a variety of conditions such as chronic inflammation, infections,
91 cancer, and aging-related disorders.
92

93 **RESULTS**

94 **ZDHHC20L as a readout for the stress response pathway**

95 In previous work on the S-acylation of the SARS-CoV-2 Spike protein by the acyltransferase
96 ZDHHC20[37,38], we found that infection induces a transcriptional shift in the *ZDHHC20* gene,
97 generating N-terminally extended isoforms of the protein, which we here collectively term
98 ZDHHC20 Long (ZDHHC20L). These longer isoforms are also expressed in cells exposed to
99 the pore-forming toxin aerolysin and *in vivo*, upon chemical-induced colitis[37]. We additionally
100 documented the presence of ZDHHC20L in untreated hepatocellular carcinoma cell line
101 HepG2[37], a finding we extended here to MCF7 breast cancer and HCT116 human colorectal
102 carcinoma cells (Fig. 1a). We also investigated whether ZDHHC20L expression could be
103 induced by aging, a process where increased stress pathways are linked to the gradual decline
104 of repair mechanisms[39]. While in total cell extracts (TCEs) from primary lung epithelial cells
105 of young donors only the canonical form of ZDHHC20 was detected, ZDHHC20L became
106 increasingly expressed in cells from donors above 60 (Fig. 1b). ZDHHC20L expression is thus
107 induced under a variety of conditions, ranging from some cancers to aging, viral infection, and
108 other stresses. This study aimed to identify the stress response pathway that leads to
109 ZDHHC20L expression.

110

111 **Activation of the transcription factor ATF2 triggers ZDHHC20L expression**

112 To elucidate the molecular mechanisms underlying ZDHHC20L expression, we mined
113 experimental gene occupancy data from ENCODE-3 (Encyclopedia of DNA Elements)[40,41]
114 hosted in the UCSC Genome Browser (Transcription Factor ChIP-seq Clusters)[42]. We
115 previously found that ZDHHC20L is translated from upstream in-frame AUGs, generating
116 longer transcripts. We also showed that FOXA1 and SP1 are transcription regulators, which
117 bind approximately 5 kb upstream of the in-frame start codons, in HepG2, human liver cancer,
118 cells[37]. Here, we found that the stress-regulated transcriptional activator ATF2[43] was recruited
119 ~5 kB further upstream (Fig. 1c) and evaluated its role in ZDHHC20L expression. In Hela cells,
120 where ZDHHC20L can be induced by aerolysin[37], we found that siRNA-silencing of ATF2

121 (Supplementary Fig. 1a) significantly reduced the toxin-induced ZDHHC20L expression (Fig.
122 1d).
123 Different kinases activate ATF2 in response to stress or growth signals[44–50] and aerolysin
124 treatment also led to ATF2 (both endogenous and over-expressed) phosphorylation, on Thr-69,
125 within its transactivation region[46] (Fig. 1d, Supplementary Fig. 1b). The presence of multiple
126 phospho-bands at around >55 kDa suggests phosphorylation on several residues and/or of
127 various ATF2 isoforms[51]. ATF2 phosphorylation could be detected under all tested conditions
128 leading to ZDHHC20L expression: in primary lung epithelial cells from older donors or
129 subjected to SARS-CoV-2 infection (Supplementary Fig. 1c), in the duodenum of mice (where
130 ZDHHC20L is constitutively expressed[37] - Supplementary Fig. 1d), and in the colon of mice
131 upon chemical-induced colitis (Supplementary Fig. 1e). Thus, ATF2 phosphorylation is
132 consistently associated with ZDHHC20L expression.
133 To assess the importance of ATF2 phosphorylation in regulating ZDHHC20L expression, we
134 generated ATF2 phospho-site mutants, either mimicking phosphorylation by aspartic acid
135 substitution or preventing it by alanine substitution, targeting four residues in the N-terminal
136 activation domain Thr-52, 69, 71 and 73 [50] (to D or A - coined 4D and 4A), two in the C-
137 terminal regulatory domain Ser-490 and 498 [44] (2D and 2A), or all six combined (6D and 6A).
138 Using bone-derived U2OS cells, which only express the canonical form of ZDHHC20,
139 overexpression of any of the ATF2 phospho-mimetic mutants was sufficient to induce
140 ZDHHC20L expression, in the absence of any stimulus (Fig. 1e, Supplementary Fig. 1f). This
141 process still required FOXA1 and SP1, as it was blocked by the combined depletion or
142 pharmacological inhibition of these transcription factors with JQ1 and mithramycin
143 respectively (Supplementary Fig. 1g). Consistently, wild-type ATF2, but not ATF2-6A, when
144 co-expressed with FOXA1 and SP1, also led to ZDHHC20L expression (Fig. 1e), which did
145 not occur when only two of these factors were over-expressed (Supplementary Fig. 1h). To
146 explore an additional functional outcome beyond controlling expression of ZDHHC20L during
147 stress, we investigated whether ATF2 activation is protective against exposure to aerolysin,
148 which like other pore-forming toxins disrupts plasma membrane integrity that can lead to cell

149 death through various pathways[52,53]. Silencing ATF2 increased cell sensitivity to aerolysin (Fig.
150 1f), which was rescued by expressing wild type (WT) or the phosphomimetic 6D ATF2 but not
151 the 6A mutant (Fig. 1f). Thus, activated ATF2 drives ZDHHC20L expression and has a
152 protective effect towards aerolysin-induce cell death.
153
154 ***ZDHHC20L* is repressed by a heterochromatin-inducing complex**
155 We further analyzed ENCODE ChIP-seq data and identified reported binding sites for the
156 protein scaffold KAP1 (KRAB domain-associated protein 1) and the histone methyltransferase
157 SETDB1 (SET Domain Bifurcated Histone Lysine Methyltransferase 1), near the ATF2
158 binding regions in U2OS and K562 lymphoblast cells (Fig. 1c) [54,55]. These two proteins are part
159 of a chromatin-modifying complex that mediates histone 3 lysine 9 trimethylation (H3K9m3),
160 leading to the formation of heterochromatin[54] and transcriptional repression[54–57] (Fig. 1g, top
161 panel). In U2OS cells, SETDB1 silencing (Supplementary Fig. 1a) alone induced ZDHHC20L
162 expression (Fig. 1h), which was suppressed by wild-type SETDB1 but not by a catalytically
163 inactive mutant (Fig. 1i), confirming the need for its enzymatic activity. KAP1 silencing
164 (Supplementary Fig. 1a) or knockout in haploid HAP1 cells (Fig. 1j) similarly triggered
165 ZDHHC20L expression (Fig. 1j) and the emergence of extended ZDHHC20 mRNA transcripts,
166 as shown by qPCR (Fig. 1k)[37]. KAP1 and SETDB1 therefore repress ZDHHC20L expression,
167 in contrast to ATF2 that is required for stress-induced ZDHHC20L expression.
168 Given the involvement of SETDB1 and KAP1, we analyzed ENCODE ChIP-seq data to assess
169 whether histone modifications had been reported at the ZDHHC20 locus. In U2OS cells,
170 repressive H3K9me3 marks were detected around the SETDB1, KAP1, and ATF2 peaks (Fig.
171 1c). Additional H3K9me3 marks within the first intron overlapped a second SETDB1 peak,
172 potentially reinforcing ZDHHC20L silencing. Active promoter marks H3K27Ac and
173 H3K4me3 (Fig. 1g, lower panel) were found flanking these repressive regions and co-localizing
174 with both the short-canonical and long ZDHHC20 transcription start sites (Fig. 1c). The
175 enhancer mark H3K4me1 (Fig. 1g) aligned with FOXA1 and SP1 ChIP-seq peaks in HepG2
176 cells (Fig. 1c), which constitutively express ZDHHC20L even without stimulation[37].

177 Altogether, these data show that under homeostatic conditions the expression of ZDHHC20L

178 isoforms is repressed by the heterochromatin-inducing KAP1/SETDB1 complex.

179

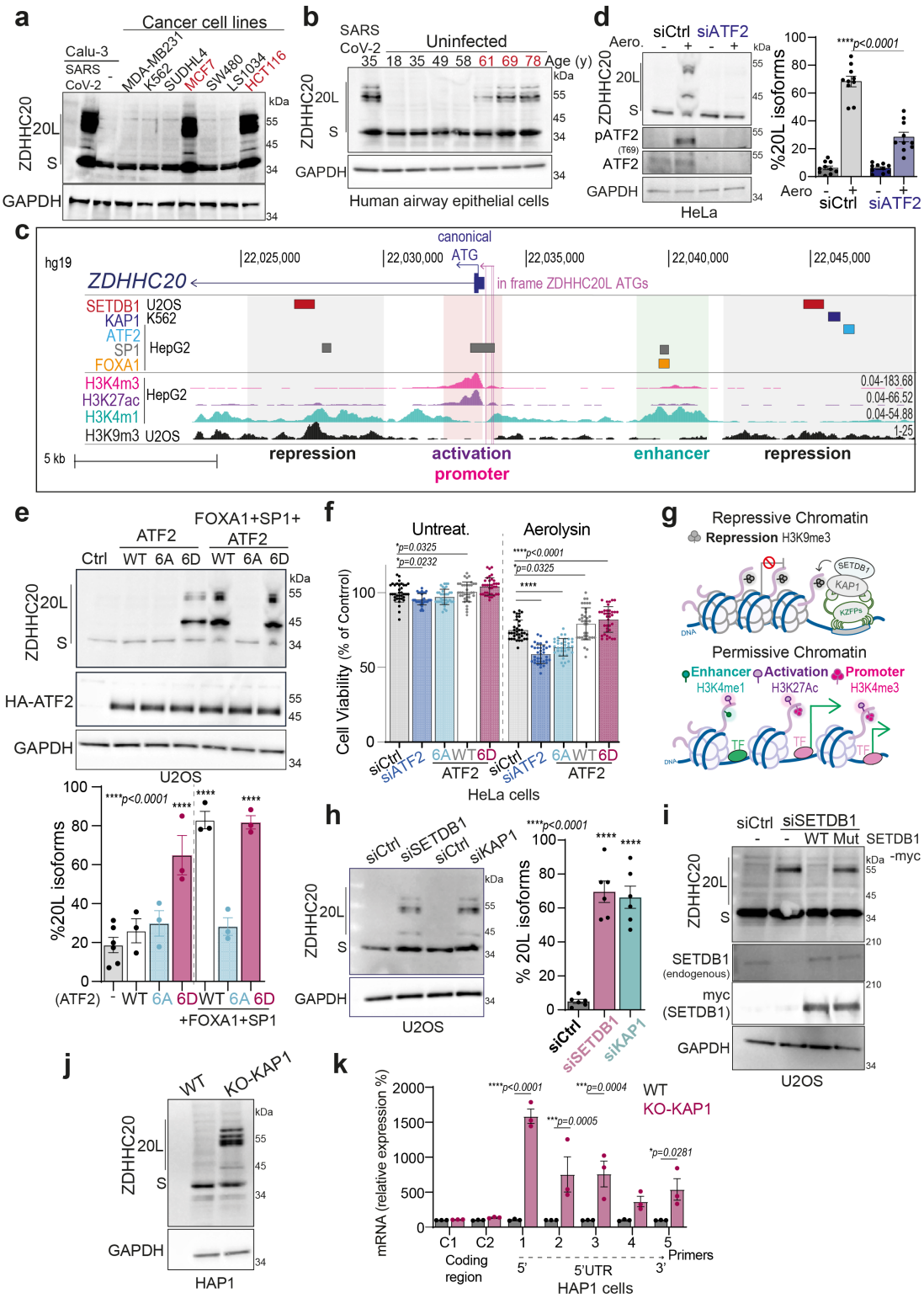
a
Cancer cell lines
Calu-3
SARS CoV-2
MDA-MB231
K562
SUDHL4
MCF7
SW480
LS1034
HCT116
ZDHHC20
20L
S
GAPDH
kDa
b
SARS CoV-2
Uninfected
35 18 35 49 58 61 69 78 Age (y)
Human airway epithelial cells
d
siCtrl siATF2
Aero.
pATF2 (T69)
ATF2
HeLa
%20L isoforms
****p<0.0001
c
hg19
canonical ATG
ZDHHC20
in frame ZDHHC20L ATGs
SETDB1 U2OS
KAP1 K562
ATF2
SP1 HepG2
FOXA1
H3K4m3
H3K27ac HepG2
H3K4m1
H3K9m3 U2OS
5 kb
repression
activation promoter
enhancer
repression
e
FOXA1+SP1+ ATF2
Ctrl WT 6A 6D WT 6A 6D
HA-ATF2
U2OS
(ATF2) - WT 6A 6D WT 6A 6D
+FOXA1+SP1
f
Untreat.
Aerolysin
Cell Viability (% of Control)
siCtrl siATF2 6A WT 6D
ATF2
HeLa cells
g
Repressive Chromatin
Repression H3K9me3
SETDB1
KAP1
KZFPs
DNA
Permissive Chromatin
Enhancer H3K4me1
Activation H3K27Ac
Promoter H3K4me3
TF
h
siCtrl siSETDB1 siCtrl siKAP1
U2OS
% 20L isoforms
siCtrl siSETDB1 siKAP1
i
siCtrl siSETDB1
WT Mut SETDB1 -myc
SETDB1 (endogenous)
myc (SETDB1)
U2OS
j
WT KO-KAP1
HAP1
k
mRNA (relative expression %)
WT
KO-KAP1
C1 C2 1 2 3 4 5 Primers
Coding region
5' 5'UTR 3'
HAP1 cells

185 **Figure 1. ATF2 and SETDB1-KAP1 dependent induction of ZDHHC20L expression.**

186 **a, b**, Western blot (WB) of ZDHHC20 isoforms (Short-S, 42 kDa; 20L, ~49, 62, 69 kDa) and GAPDH
187 (loading control) in a, indicated cancer cell lines and SARS-CoV-2-infected Calu-3 cells (MOI 0.1, 24
188 h); b, primary human airway epithelia from donors of different ages, untreated or SARS-CoV-2-infected
189 (MOI 0.1, 48 h). **c,** Overview of the ZDHHC20 locus (first intron, exon, 5′ UTR; hg19). Tracks show
190 in-frame start codons (ATGs), transcript (GENCODE), histone modifications (ENCODE: H3K9me3,
191 repression; H3K4me1, enhancer; H3K27Ac, activation; H3K4me3, promoter), and SETDB1/KAP1,
192 ATF2, SP1, FOXA1 ChIP-seq peaks. **d,** WB as in a, total and phospho-ATF2 in HeLa cells (siCtrl or
193 siATF2), untreated or treated with proaerolysin (10 ng/ml, 1 h at 37 °C, incubated further 8 h).
194 Quantification of 20L isoforms shown as mean ± SEM, dots represent independent experiments (n = 10);
195 *p* values by two-way ANOVA, Sidak's correction. **e,** WB as in a, in U2OS expressing ATF2 (WT, 6D,
196 6A), or FOXA1 and SP1. Results mean ± SEM, independent experiments (Ctrl, n = 6; others, n = 3); *p*
197 values versus Ctrl, two-way ANOVA, Dunnett's correction. **f,** Cell viability of HeLa cells (ATP assay),
198 normalized to untreated siCtrl (100%), mean ± SD from one of three representative assays (n = 34
199 replicates); *p* values vs. siCtrl, two-way ANOVA, Dunnett's correction. **g,** Schematic: KAP1-KZFPs
200 recruit SETDB1, promoting H3K9me3-mediated repression and active histone mark removal (adapted
201 from ref. 36). **h**, WB as in d, U2OS cells siCtrl, siSETDB1, or siKAP1-depleted (72 h). Results mean ±
202 SEM, independent experiments (n = 6); *p* values vs. Ctrl, two-way ANOVA, Dunnett's correction. **i,** WB
203 as in h, siSETDB1 cells expressing WT or catalytically inactive SETDB1 mutant (Mut). **j,** WB as in a,
204 in HAP-1 wild-type or KAP1-knockout cells. **k,** mRNA quantification across ZDHHC20 transcripts
205 (coding regions: C1, C2; 5'UTR positions: 1–5) in HAP-1 wild-type or KAP1-knockout cells, mean ±
206 SEM, independent experiments, *p* values vs. normalized WT, two-way ANOVA, Dunnett's correction.
207
208

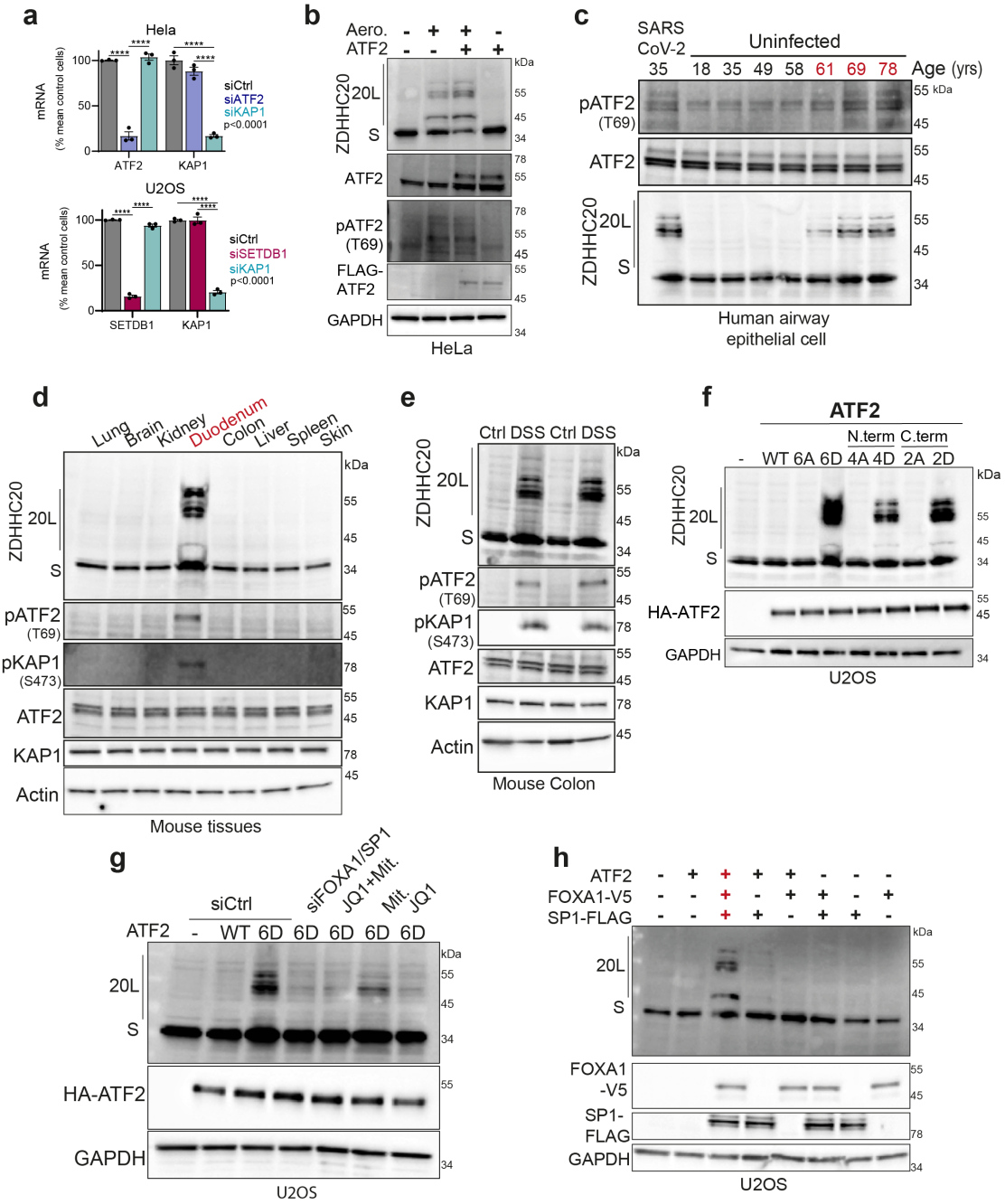

Supplementary Figure 1. ATF2 and SETDB1-KAP1 dependent induction of ZDHHC20L expression. a, mRNA quantification validating efficiency of ATF2, KAP1 and SETDB1 siRNA depletion in U2OS and HeLa cells. **b–f,** Western blots (WB) for ZDHHC20 isoforms (Short-S, 20L), total/phospho-ATF2 in lysates from: b, HeLa cells overexpressing ATF2-FLAG (24 h), untreated or treated with proaerolysin toxin (10 ng/ml, 1 h at 37 °C, washed, further 8 h incubation); c, primary human airway epithelia (see Fig. 1b); d, mouse tissue extracts (as indicated); e, colon extracts from mice treated ± DSS (7 d) followed by 3 d recovery (d,e blots include total/phospho-KAP1); f, U2OS cells overexpressing ATF2 WT or indicated phospho-mutants (6A, 6D, 4A, 4D, 2A, 2D). **g,** WB as in f, in U2OS cells treated (24 h) with FOXA1 inhibitor (JQ1, 100 nM), SP1 inhibitor (mithramycin, 100 nM), or siRNA-depleted (72 h) for FOXA1 and SP1. **h,** WB analysis as in f, U2OS cells expressing ATF2-HA, SP1-FLAG, and FOXA1-V5, individually or combined.

223 **ZNF354A recruits the repressive complex to the ZDHHC20L regulatory region**

224 KAP1/SETDB1 complexes are generally tethered to DNA by KRAB-containing zinc finger
225 proteins (KZFPs) (Fig. 1g), of which approximately 380 are encoded by the human
226 genome[54,55,57]. To identify the KZFP responsible for docking KAP1 at the *ZDHHC20* locus, we
227 mined KRABopedia, a published ChIP-seq dataset generated from HEK293T cells
228 overexpressing HA-tagged forms of each KZFP individually[58,59]. The binding sites of several
229 KZFPs map to the promoter region of ZDHHC20 (Fig. 2a, Supplementary Fig. 2a), a pattern
230 that is not uncommon for this class of proteins[58,59]. In contrast, ZNF317, ZNF354A, ZNF677,
231 and ZNF793 have binding sites within the "repression" region of the acyltransferase gene.
232 ZNF354A binding sites co-localize with the SETDB1 and H3K9me3 peaks upstream and
233 downstream of the *ZDHHC20* TSSs (Fig. 2a, Supplementary Fig. 2a). We silenced each of the
234 four KZFPs individually in U2OS cells using mixes of siRNAs (Supplementary Fig. 2b). Only
235 the ZNF354A knockdown led to the expression of ZDHHC20L (Fig. 2b), which could be
236 reverted by the expression of ZNF354A-HA (Supplementary Fig. 2c). Importantly, silence of
237 ZNF354A did not lead to a decrease of the mRNA of its paralogue ZNF354B, with which it
238 shares 86% identity (Supplementary Fig. 2de), and consistently ZNF354B silencing did not
239 trigger ZDHHC20L expression (Supplementary Fig. 2f).

240 We next tested the specificity for ZNF354A versus other KZFPs by immunoprecipitation (IP)
241 experiments. Upon IP of KAP1 from U2OS cells overexpressing ZNF354A or two irrelevant
242 KZFPs, all three KZFPs co-precipitated with KAP1, as the presence of canonical KRAB
243 domains would predict [60]. Interestingly, the interaction between KAP1 and ZNF354A was
244 disrupted by aerolysin treatment, which was not the case for the two other KZFPs (Fig. 2c).
245 Thus, under basal conditions, ZNF354A recruits the KAP1 repressive complex to the 5′
246 regulatory region of DNA loci such as the ZDHHC20 locus. This interaction is disrupted upon
247 aerolysin treatment, leading to the dissociation of ZNF354A and KAP1.

248

249

250

251 **Dynamics of the KAP1-ZNF354A containing repressive complex**

252 Since ATF2, KAP1 and ZNF354A bind to the same region within the *ZDHHC20* 5'UTR, we
253 tested whether they could be part of a single complex. We immunoprecipitated KAP1 from
254 ZNF354A-FLAG-expressing cells, which were depleted or not of endogenous ATF2 using
255 siRNA, and recomplemented with wild-type or ATF2 phosphorylation mutants (6A and 6D).
256 Under resting conditions, KAP1 co-precipitated ZNF354A, as well as ATF2 (Fig. 2d). The co-
257 precipitation between the three proteins was also observed when performing IPs against the
258 ZNF354A HA tag (Supplementary Fig. 2g). Despite the disruption of the complex, ATF2 –
259 especially its endogenous phosphorylated form–remained associated with KAP1 (Fig. 2d).
260 These results indicate that a subset of ATF2-KAP1 interactions occurs independently of
261 ZNF354A-mediated chromatin association. Since ATF2 has not previously been found to
262 associate with KAP1-nucleated repressive complexes, we tested whether it also interacts with
263 other KAP1–KZFP complexes. IP of ZNF317, ZNF677, and ZNF793 did not lead to the co-IP
264 of ATF2 (Supplementary Fig. 2g, j). Thus, ATF2, KAP1 and ZNF354A are part of a somewhat
265 non-canonical repressive complex. Interestingly, expression of the phospho-mimetic ATF2-6D
266 mutant was sufficient to disrupt the KAP1–ZNF354A interaction even in the absence of
267 aerolysin (Fig. 2d), indicating that ATF2 acts as an upstream, stress-sensitive regulator of the
268 complex. The mechanisms underlying ATF2 recruitment to ZNF354A-specific KAP1
269 complexes remain to be elucidated.

270 Since ATF2 undergoes phosphorylation upon stress, we wondered whether the same occurs for
271 KAP1 and ZNF354A. KAP1 is known to undergo phosphorylation on Ser-824 and Ser-473 in
272 response to DNA damage[61–64,65] and on Ser-473 under oxidative stress[66]. Using an anti-
273 phospho-Ser-473-KAP1 antibody, we detected KAP1 Ser-473 phosphorylation during SARS-
274 CoV-2 infection, concomitant with ATF2 activation (Fig. 2e). KAP1 Ser-473 phosphorylation
275 was also observed upon aerolysin treatment (Supplementary Fig. 2h), detected in the duodenum
276 of mice (Supplementary Fig. 1d), and in the colon of mice upon chemical-induced colitis
277 (Supplementary Fig. 1e). To determine whether Ser-473 is the major phosphorylation site, we
278 expressed WT KAP1 or the S473A phospho-deficient mutant in cells silenced for the

279 endogenous protein and exposed them to aerolysin. Western blot analysis of KAP1 IP fractions,
280 using anti-phospho-Ser/Thr antibodies, showed no signal for the S473A mutant (Fig. 2f),
281 validating Ser-473 as the primary phosphorylation site under our conditions. Finally, we
282 verified that Ser-473 phosphorylation was necessary to trigger ZDHHC20L expression upon
283 aerolysin treatment (Supplementary Fig. 2i). As with ATF2, expression of a phospho-mimetic
284 S473D KAP1 mutant was sufficient to trigger ZDHHC20L expression without any stimulus
285 (Fig. 2g).
286 We next probed for the potential phosphorylation of ZNF354A. Aerolysin treatment and SARS-
287 CoV-2 infection both induced serine/threonine phosphorylation of ZNF354A, detected by
288 phospho-Ser/Thr antibodies in ZNF354A-IPs (Fig. 2h). This phosphorylated band
289 corresponded to ZNF354A, as it was absent in ZNF354A-silenced cells (Fig. 2h). Aerolysin
290 did not induce the phosphorylation of a control KZFP, ZNF793 (Supplementary Fig. 2j).
291 Finally, aerolysin-induced phosphorylation of KAP1 and ZNF354A depended on ATF2
292 phosphorylation, which alone was sufficient to drive all these events (Fig. 2i).
293 Together, these findings demonstrate that ZDHHC20L expression is repressed by a complex
294 comprising ATF2, SETDB1, KAP1, and ZNF354A. Upon stress, ATF2 is phosphorylated,
295 followed by phosphorylation of KAP1 and ZNF354A, leading to dissociation of the KAP1–
296 ZNF354A complex and induction of ZDHHC20L expression (Fig. 2j).
297
298
299

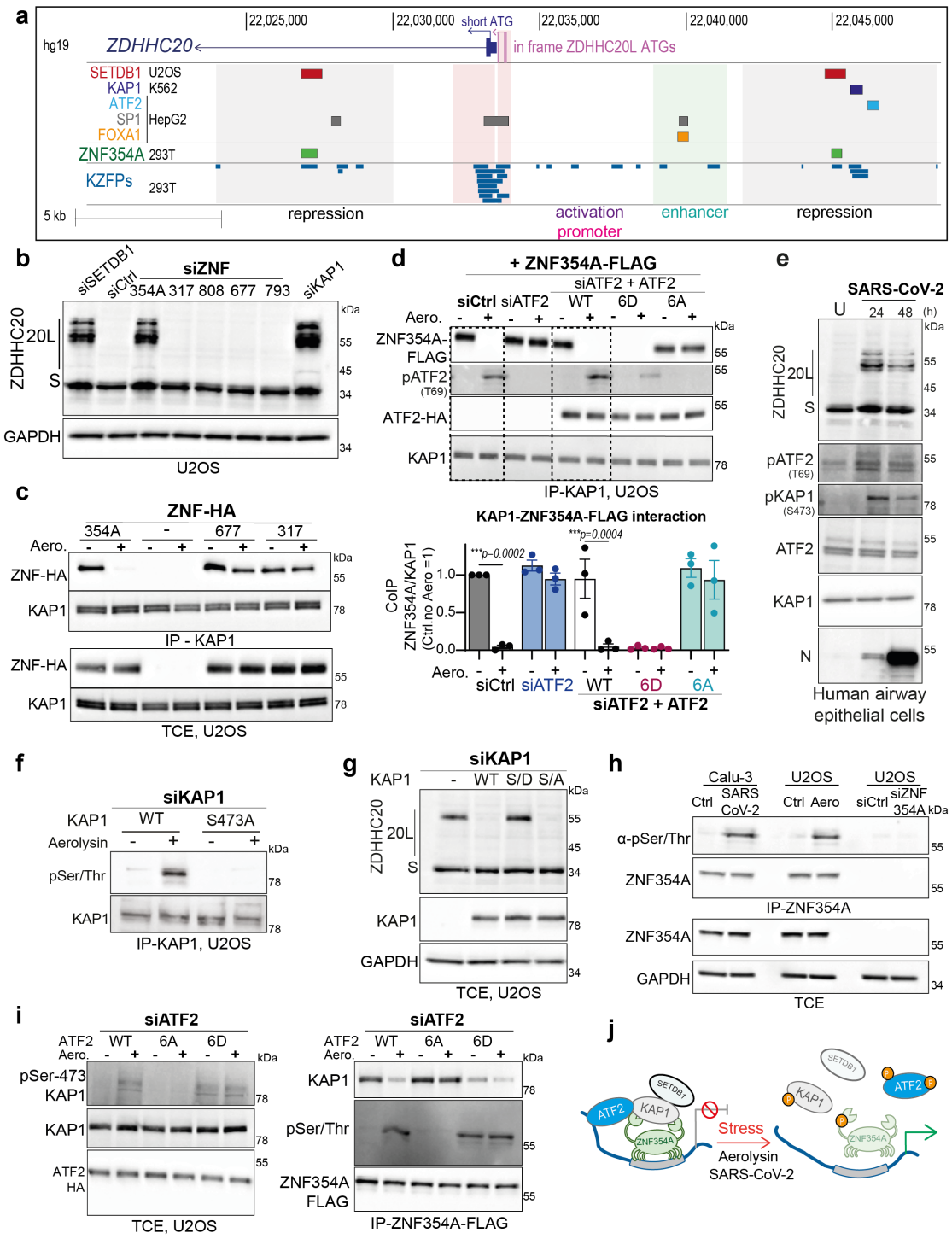

300
301
302
303
304
305
306
307
308
309
310
311

Figure 2. ZNF354A controls the expression of stress-induced ZDHHC20L.

a, Overview of ZDHHC20 locus (intron, exon, 5′ UTR; hg19). Tracks: transcription start codons (ATGs), transcript annotations (GENCODE), ChIP-seq peaks (ENCODE: SETDB1/KAP1, ATF2, SP1, FOXA1), ZNF354A and KZFP peaks from HEK293T cells (squish view,) from KRABopedia[58] , https://tronoapps.epfl.ch/web/krabopedia/); **b,** Western blot (WB) of ZDHHC20 isoforms (Short-S, 20L) and GAPDH (loading control) in U2OS cells depleted of SETDB1, KAP1, or indicated KZFPs. **c,** Immunoprecipitation (IP) of endogenous KAP1 in U2OS cells overexpressing HA-tagged KZFPs, untreated or treated with proaerolysin toxin (10 ng/ml, 1 h at 37 °C, washed, incubated further 8 h). Blots: co-IP fractions and total cell extracts (TCE). **d,** IP-KAP1 as in (c) from siCtrl or siATF2 U2OS cells expressing ZNF354A-FLAG complemented with indicated ATF2 constructs (WT, 6D, 6A; 24 h). Results mean ± SEM; dots represent independent experiments (n = 3); P values vs. untreated, two-way ANOVA, Tukey's correction. **e,** WB as (b) in human primary lung epithelial cells infected with SARS-CoV-2 (MOI 0.1). **f,** IP-KAP1 in siKAP1 U2OS cells expressing KAP1-WT or S473A mutant, treated with aerolysin as in (c). Blots show KAP1 and phospho-Ser/Thr proteins in IP fractions. **g,** WB of TCEs as (b) in siKAP1 U2OS cells expressing KAP1 WT, S473A (S/A), or S473D (S/D). **h,** IP-ZNF354A from Calu-3 cells infected with SARS-CoV-2 (24 h), aerolysin-treated U2OS cells (as in c), or siCtrl/siZNF354A-depleted U2OS cells. Blots show ZNF354A and phospho-Ser/Thr proteins (IP fractions) and ZNF354A and GAPDH (TCE). **i,** IP-ZNF354A -HA from U2OS cells expressing indicated ZNF354A-FLAG and ATF2 constructs, aerolysin-treated as (c). Blots: IP fractions (KAP1, ATF2, phospho-Ser/Thr); TCE (total/pS473-KAP1, ATF2-HA). **j,** Model of ATF2-KAP1-ZNF354A repressive complex before and after stress.

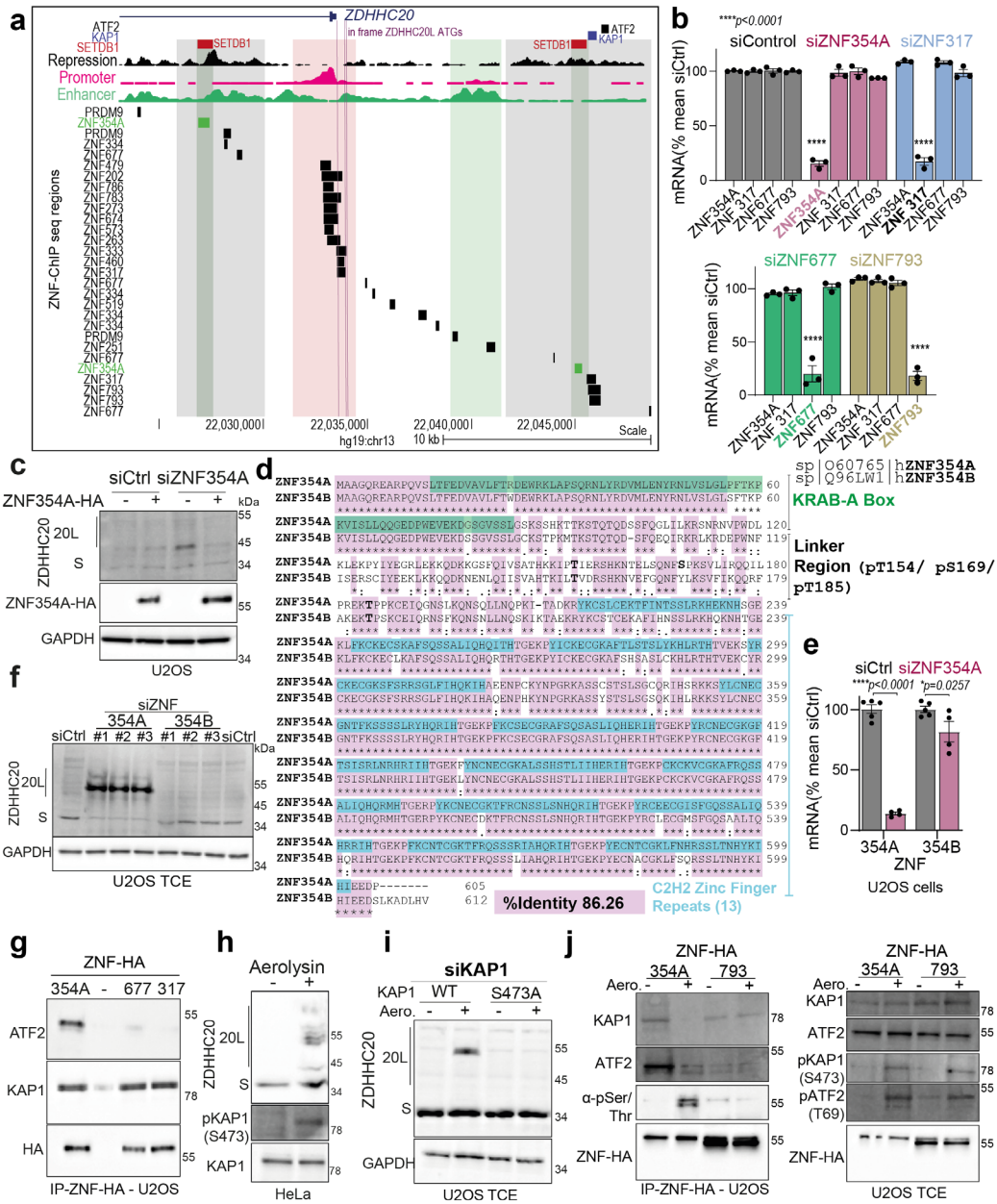

Supplementary Figure 2. ZNF354A controls the expression of stress-induced ZDHHC20L.

a, ZDHHC20 locus (hg19), indicating transcription start codons, transcripts (GENCODE), histone modifications, and ChIP-seq peaks SETDB1/KAP1/ATF2 (ENCODE); ZNF354A/KZFP, from HEK293T (KRABopedia[58]). See also fig 2a. **b,** mRNA levels of indicated KZFPs in U2OS cells after correspondent siRNA depletion (72 h). Mean ± SEM, each dot is an independent experiment n = 3; *p* values vs siCtrl, two-way ANOVA, Dunnett's correction.**c**, Western blot (WB) of ZDHHC20 isoforms and GAPDH (loading control) in siZNF354A U2OS cells complemented with ZNF354A-HA. **d**, Protein sequence alignment of the indicated ZNF354A and ZNF354B Uniprot sequences with highlighted KRAB-A-Box (green), linker region with phosphorylated residues, 13 uniprot-annotated C2H2 Zinc-finger repeats and identity-residues (pink). **e**, mRNA levels as in b for ZNF354A and ZNF354B. Mean ± SEM, each dot is an independent biological replicate n = 5 siCtrl and n=4 siZNF354A; *p* values by two-way ANOVA, Tukey's correction. **f**, WB as in c, in U2OS cells siZNF354A or siZNF354B depleted with three independent oligos. **g,** WB from IP-ZNF-HA fractions from U2OS cells expressing the indicated KZFP proteins. Blots show ATF2, KAP1 and ZNF-HA in IP-HA fractions. **h**, WB as in c, including total/phospho-KAP1 in HeLa cells ± proaerolysin toxin (10 ng/ml, 1 h at 37 °C, plus 8 h). **i**, WB as in c in siKAP1 U2OS cells expressing WT or S473A KAP1 mutant. **j**, IP-ZNF-HA from U2OS cells expressing indicated constructs, treated as in d. Blots show KAP1, ATF2, phospho-Ser/Thr (IP fractions); phospho-ATF2/KAP1 and total ZNF-HA (total cell lysates).

354 **p38 and JNK trigger phosphorylation of the repressive complex components**

355 To further explore the regulatory mechanisms of the ATF2-KAP1-ZNF354A complex, we first
356 identified the ZNF354A phosphorylation sites. Three residues, located in the linker region
357 between the KAP1-binding KRAB domain and the DNA-binding domains, were found by
358 phospho-proteomics in breast cancer (Ser-169 and Thr-185)[67], and a subgroup of large T-cell
359 lymphoma (T154)[68] (https://www.phosphosite.org). This linker region is the most diverse
360 between ZNF354A and ZNF354B. We generated the phospho-mutants of the three ZNF354A
361 sites and expressed them in ZNF354A-silenced U2OS cells. A phospho-Ser/Thr signal was
362 observed upon aerolysin treatment of WT ZNF354A-, but not S169A ZNF354A-expressing
363 cells (Fig. 3a). The signal was reduced, but not absent, when expressing the T154A or T185A
364 mutants (Fig. 3a), indicating a leading phosphorylation event at Ser169, as confirmed using
365 phospho-tag gels (Fig. 3b). Ser-169 is absent in ZNF354B (Supplementary Fig. 2d).

366 We next searched for the kinases involved in ZDHHC20L expression. We tested a panel of
367 inhibitors targeting MAPKs (*e.g.* JNK, p38, and ERK) and ATM since these are known to
368 modify KAP1 and ATF2 following different stresses, including infection[69,70]. Inhibition of
369 either p38 or JNK abolished the aerolysin-induced expression of ZDHHC20L and KAP1
370 phosphorylation, and reduced phosphorylation of ATF2. ATF2 phosphorylation was also
371 sensitive to ERK inhibition (Fig. 3c). p38 and JNK inhibitors similarly affected KAP1 and
372 ZNF354A phosphorylation and ZDHHC20L expression in cells expressing the ATF2 6D
373 mutant, in the absence of stressor (Fig. 3de). Thus, phosphorylation of ATF2, KAP1 (on Ser-
374 473) and ZNF354 (on Ser-169) occurs in a p38- and JNK-dependent manner and is required
375 for the expression of ZDHHC20L.

376

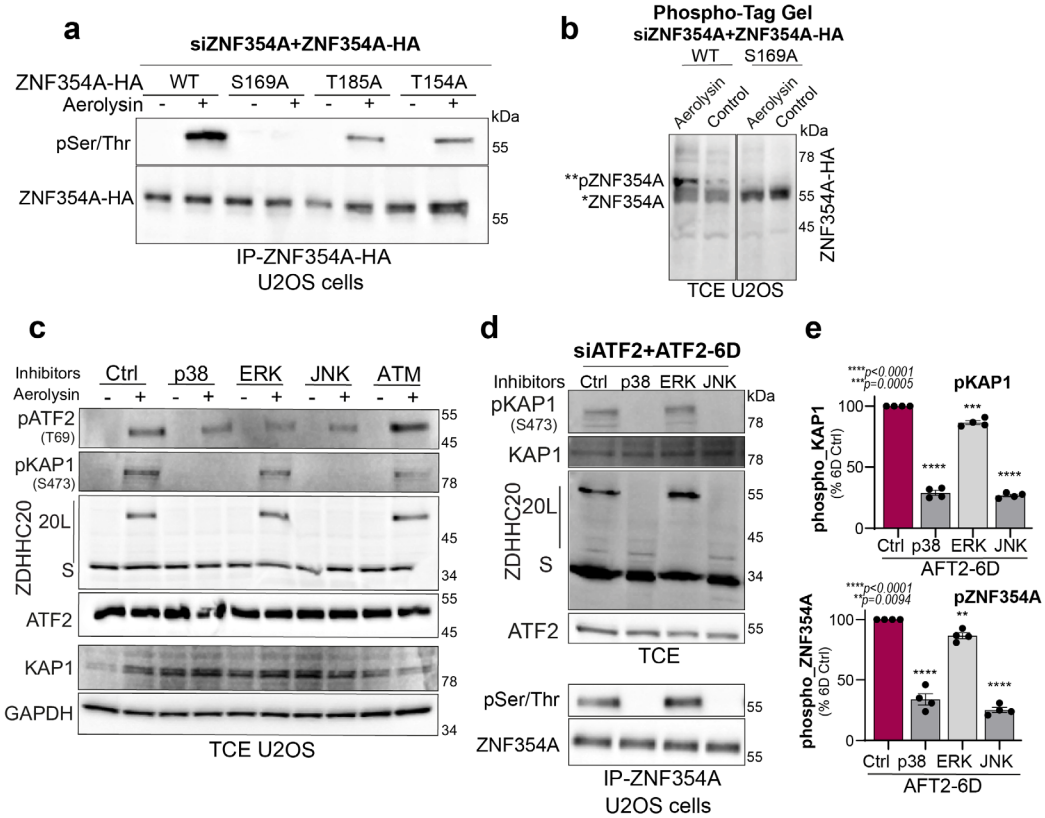

Figure 3. p38 and JNK phosphorylation of ZNF354A

a, Immunoprecipitation (IP) of ZNF354A-HA from U2OS cells (siZNF354A, 72 h) expressing WT or phospho-mutants of ZNF354A, untreated or treated with proaerolysin (10 ng/ml, 1 h at 37°C, washed, incubated additional 8 h). Blots show phospho-Ser/Thr proteins and ZNF354A in IP fractions.

b, Phospho-Tag Western blot of total cell extracts (TCE) from U2OS cells treated as in (a).

c, Western blot of ZDHHC20 (Short-S, 20L isoforms), phospho-KAP1 (S473), phospho-ATF2 (T69), total KAP1, ATF2, and GAPDH (loading control) in TCE from U2OS cells treated with proaerolysin as in (a), plus kinase inhibitors.

d, Western blot as in (c) from TCE and IP-ZNF354A of U2OS cells (siATF2, 72 h) expressing ATF2-6D phosphomimetic mutant (24 h), treated with kinase inhibitors.

e, Quantification of phospho-KAP1 and phospho-Ser/Thr-ZNF354A bands from blots in (d). Mean ± SEM; dots represent independent experiments (n=4). Statistical analysis by two-way ANOVA, Dunnett's test; P values compare treated conditions to untreated control (Ctrl).

393 **ZNF354A determines the genetic specificity of the cellular response to oxidative stress**
394
395 We next explored whether the de-repression by the ZNF354A-containing complex has a
396 broader effect than just controlling ZDHHC20L expression and could be coupled with the
397 activation of specific host stress response/repair pathways. To identify genes that reside in the
398 vicinity of the 1,665 ZNF354A peaks, we analyzed our ChIP-seq data from HEK293T cells
399 overexpressing HA-tagged ZNF354A[35,58] using GREAT (Genomic Regions Enrichment
400 Annotations) with a 300 kb window from the TSS as the cut-off for gene association [71]. GREAT
401 analysis mapped the ZNF354A peaks to the regulatory regions of 2,116 genes associated with
402 a variety of ontologies (Fig. 4a). Among the enriched pathways, selenium metabolism stood
403 out due to its connection to defense against ROS (Fig. 4a). Further manual curation of the gene
404 list led to the identification of additional selenium-related genes (Supplementary Fig. 3a).
405 The identified redox-related genes included: *MAT1A* (methionine adenosyltransferase 1A),
406 which synthesizes S-adenosylmethionine, a precursor for GSH biosynthesis[72]; *SLC7A11*,
407 encoding the main subunit of the cystine/glutamate antiporter system x_c^-, essential for GSH
408 production from extracellular cystine[73]; and *TXNRD1* (thioredoxin reductase-1 and its homolog
409 *TXNRD3*), which can reduce cystine after its uptake by the x_c^- system thereby contributing to
410 GSH synthesis[74]. We also found 8 selenoprotein-encoding genes (Supplementary Fig. 3a).
411 These proteins, of which the human proteome counts 25, contain a selenocysteine in their
412 primary sequence which they use to reduce H_2O_2 and organic hydroperoxides[12,75].
413 To test whether ZNF354A is indeed a regulator of antioxidant defense genes, we performed
414 RNA-seq upon ZNF354A knockdown in U2OS (Supplementary Fig. 4a), which led to the
415 identification of 1,223 significantly upregulated genes (fold change >2, p-adjusted 0.05) (Fig.
416 4b). Gene Set Enrichment Analysis (GSEA) indicated that these genes are involved in
417 protective responses against external insults, including bacteria, viruses and chemical stresses,
418 as well as antioxidant activity, lipid perturbations, and the NRF2 pathway (Fig. 4cd,
419 Supplementary Fig. 4b, Supplementary Table 3, and Supplementary dataset), pointing in the
420 same direction as the above ChIP-seq analysis of ZNF354A-overexpressing HEK293T cells
421 (Supplementary Fig. 3a).

422 Because the NRF2 pathway has a well-established regulatory role in antioxidant responses and
423 has been reported to be positively regulated by KAP1[76], we tested its potential involvement in
424 ZDHHC20L expression. While silencing ZNF354A leads to ZDHHC20L expression, this was
425 prevented by the additional silencing of NRF2 (Supplementary Fig. 4cd). Thus, together with
426 SP1 and FOXA1[37], NRF2 also positively regulates ZDHHC20L expression.
427 To validate the gene set of Supplementary Fig. 3a, we performed quantitative PCR (qPCR). In
428 ZNF354A-silenced cells, the mRNA levels of *MAT1A, SLC7A11, TXNRD1,* the redox regulator
429 *GLRX* (Glutaredoxin-1), *SEPHS2* (selenophosphate synthetase) and *FSP1* were all increased
430 (Supplementary Fig. 4e), consistent with elevated protein levels of MAT1A (Supplementary
431 Fig. 4a). Complementary qPCR analysis in cells overexpressing ZNF354A for 24 h revealed
432 downregulation of most of these target genes (Supplementary Fig. 4f), further supporting the
433 regulatory role of ZNF354A.

434 As predicted by the analysis of the ZNF354A DNA binding regions (Fig. 4a), this KZFP is
435 involved in the repression of genes encoding key antioxidant cellular defense effectors (Fig. 4,
436 Supplementary Fig. 3a, 4b, and Supplementary Table 3). Many of its target genes are indeed
437 involved in GSH biosynthesis, iron metabolism, the mevalonate pathway, and the NADPH-
438 FSP1-CoQ10 oxidoreductase system, which protects cells from lipid radical-induced
439 damage[21,22] (Fig. 4e). These various independent analyses point towards ZNF354A as a key
440 regulator of the genetic control of cellular antioxidant defenses, both selenium/thiol-dependent
441 and -independent, and thereby the cellular sensitivity to ferroptosis[7,12,77].
442 To assess the evolutionary conservation of the pathway, we extended our analysis to the mouse
443 ortholog of ZNF354A, ZFP354A. Using a liftover strategy [42,78], we mapped human ZNF354A
444 binding sites to the mouse genome assembly, identifying approximately 300 loci successfully
445 converted. Remarkably, ZFP354A also binds near genes involved in antioxidant defense
446 (Supplementary Fig. 3a). Consistently, silencing ZFP354A in mouse cells resulted in the
447 expression of mouse ZDHHC20L (Supplementary Fig. 3b), mirroring our findings in human

448 cells and supporting a conserved function of ZNF354A/ ZFP354A in regulating oxidative stress
449 responses.
450 ZNF354A binds predominantly to transposable elements (TEs), with some additional binding
451 observed in introns, as documented in Krabopedia [58] (Supplementary Fig. 3c). Among enriched
452 TE families, ZNF354A displays a strong preference for LINE-1 (Long Interspersed Nuclear
453 Elements)[15,19]. In the curated, redox-associated gene signature upregulated upon ZNF354A
454 depletion, the nearest ZNF354A peaks were also largely associated with LINE-1 elements
455 (Supplementary table 3). Future research will investigate how the emergence of ZNF354A and
456 its cognate TE targets contributed to shaping the regulatory network governing the LORD
457 pathway in placental mammals. This includes examining the role of ZNF354B, which, despite
458 its strong similarity to ZNF354A, exhibits a distinct binding profile with significantly fewer
459 peaks, suggesting functional divergence (Supplementary Fig. 3e).
460

a

Gene	Gene Name	TSS Distance to ZNF354A peak(s)	Seleno- protein	Redox/Sel function	LiftOver (mouse)
GLRX	Glutaredoxin-1	-24514	no	*S*-(de)glutathionylation	-33670
GPX6	Glutathione peroxidase 6	47542	yes	reduction of hydrogen peroxide.	30098
MAT1A	Methionine Adenosyltransferase 1A	-28062, -16487	no	methionine cycle (synthesis GHS)	n.d.
SELB/EEFSEC	Eukaryotic Elongation Factor, Selenocysteine-TRNA Specific	194202	yes	Sec.tRNA elongation factor	152742
SELS	Selenoprotein S	-12179	yes	reductase	-13661
SEPHS2	Selenophosphate Synthetase 2	15386	yes	synthesis of selenophosphate	13010
SEPP1 (SELP)	Selenoprotein P, Plasma, 1	-121809, -52889	yes	Se transporter protein	n.d.
SEPSECS	Sep (O-Phosphoserine) TRNA:Sec (Selenocysteine) TRNA Synthase	-71731	yes	Selenocysteine synthase	-69778
SLC7A11 (XCT)	Solute Carrier Family 7 (Anionic Amino Acid Transporter Light Chain, Xc- System), Member 11	-114554	no	glutamate-cystine antiporter	n.d.
TXNIP	Thioredoxin-interacting protein (TXNIP)	-1296	no	binds and regulates thioredoxin	-1239
TXNRD1	Thioredoxin Reductase 1	72592	yes	thioredoxinreductase	26264
TXNRD3	Thioredoxin Reductase 3	-35307,65219	yes	thioredoxinreductase	n.d.

Retrieved by GREAT / Manual Curated

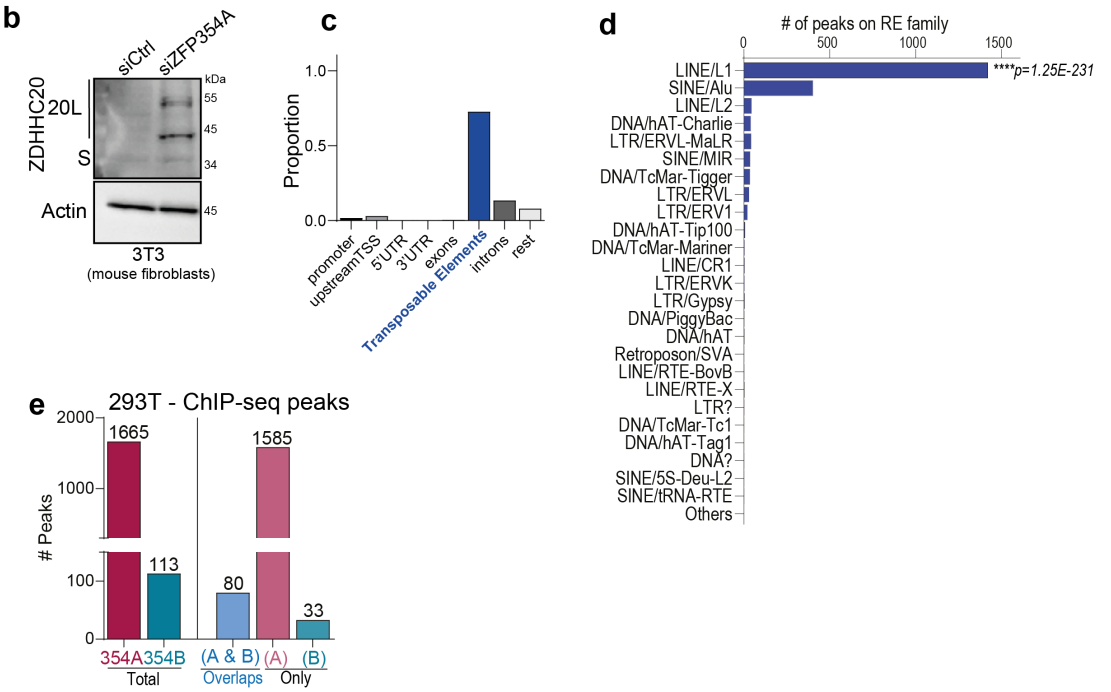

Supplementary Figure 3. ZNF354A binds to preferentially to transposable elements and controls selenium-related genes.

a. Selected genes associated with selenium pathways, antioxidant, and anti-ferroptotic activities identified near ZNF354A ChIP-seq peaks (within 300 kb from TSS) in HEK293T cells. Gene symbols, gene names, and distances to peaks are indicated. **b.** Western blots of 3T3 mouse fibroblasts transfected with siCtrl or siZNF354A (mouse ZFP354A). Blots show ZDHHC20 isoforms (Short-S 43 kDa and 20L 50 and 53 kDa) and loading controls (actin). **c.** Barplot depicting the distribution of peaks over genomic features with exclusive selection, meaning each peak is assigned to only one feature. **d.** Barplot showing the overlap of ChIP-seq peaks with TE families. P-values were computed using a binomial test. **e.** Comparison of ChIP-seq peaks for ZNF354A and ZNF354B, showing specific peaks and direct overlaps (≥1 bp). See methods or https://tronoapps.epfl.ch/web/krabopedia/ for full datasets.

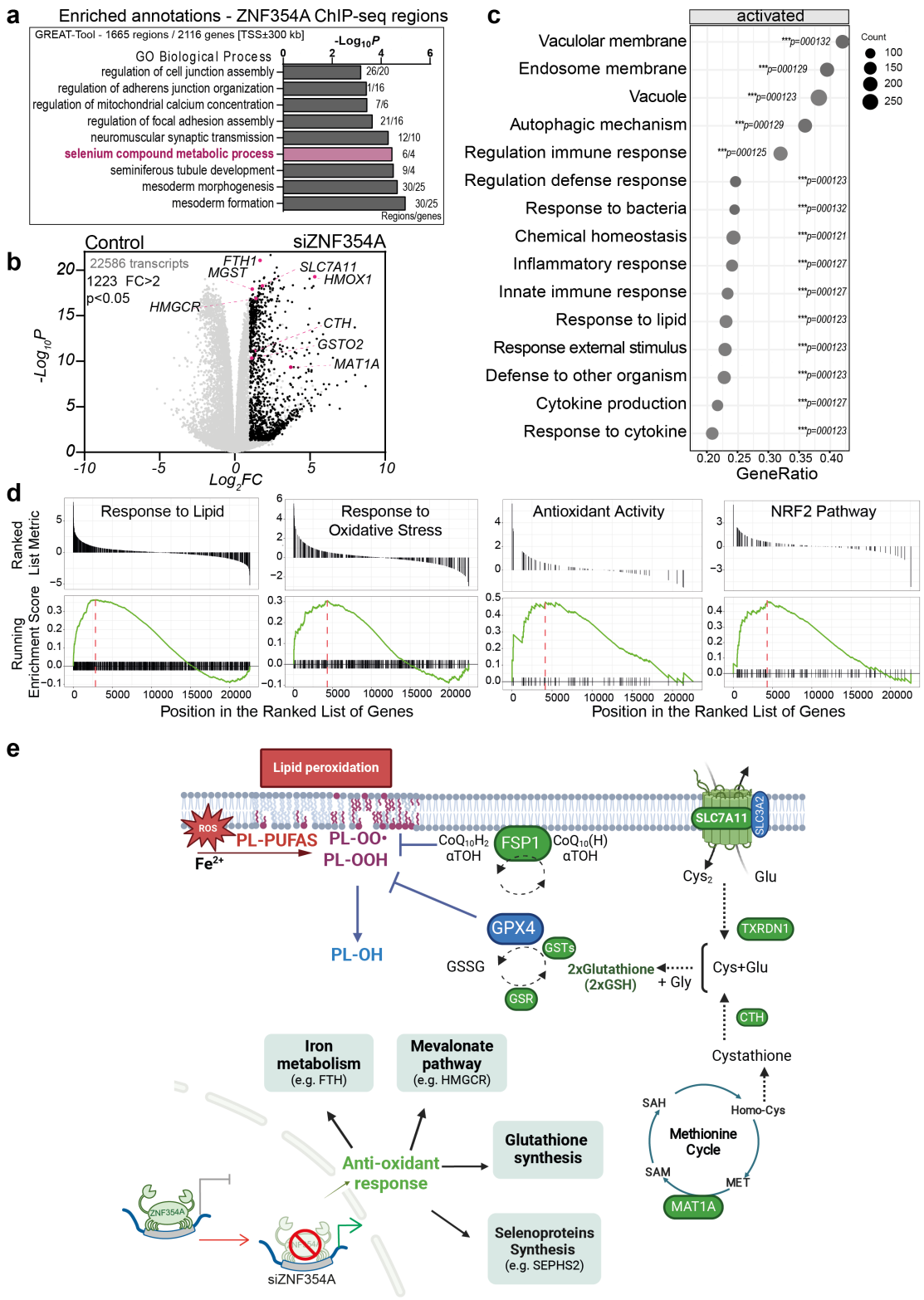
a
Enriched annotations - ZNF354A ChIP-seq regions
GREAT-Tool - 1665 regions / 2116 genes [TSS±300 kb]
GO Biological Process
-Log10P
regulation of cell junction assembly 26/20
regulation of adherens junction organization 1/16
regulation of mitochondrial calcium concentration 7/6
regulation of focal adhesion assembly 21/16
neuromuscular synaptic transmission 12/10
selenium compound metabolic process 6/4
seminiferous tubule development 9/4
mesoderm morphogenesis 30/25
mesoderm formation 30/25
Regions/genes
b
Control
siZNF354A
22586 transcripts
1223 FC>2
p<0.05
FTH1
MGST
SLC7A11
HMOX1
HMGCR
CTH
GSTO2
MAT1A
-Log10P
Log2FC
c
activated
Vaculolar membrane
Endosome membrane
Vacuole
Autophagic mechanism
Regulation immune response
Regulation defense response
Response to bacteria
Chemical homeostasis
Inflammatory response
Innate immune response
Response to lipid
Response external stimulus
Defense to other organism
Cytokine production
Response to cytokine
Count
GeneRatio
d
Response to Lipid
Response to Oxidative Stress
Antioxidant Activity
NRF2 Pathway
Ranked List Metric
Running Enrichment Score
Position in the Ranked List of Genes
e
Lipid peroxidation
ROS
PL-PUFAS
PL-OO•
PL-OOH
Fe2+
CoQ10H2 αTOH
FSP1
CoQ10(H) αTOH
SLC7A11
SLC3A2
Cys2
Glu
PL-OH
GPX4
GSTs
GSSG
GSR
2xGlutathione (2xGSH)
+ Gly
Cys+Glu
TXRDN1
CTH
Cystathione
Iron metabolism (e.g. FTH)
Mevalonate pathway (e.g. HMGCR)
Anti-oxidant response
Glutathione synthesis
Selenoproteins Synthesis (e.g. SEPHS2)
SAH
Homo-Cys
Methionine Cycle
SAM
MET
MAT1A
ZNF354A
siZNF354A

Figure 4. ZNF354A is a master regulator of antioxidant responses.

a, Ontologies (GREAT analysis) from ZNF354A ChIP-seq peaks in HEK293T cells. Histogram shows enriched terms ranked by P value. **b,** Volcano plot of RNA-seq analysis from U2OS cells (siCtrl vs. siZNF354A, 72 h), displaying expression changes of 22586 transcripts. Log2 fold change (FC) vs. −log10 P value plotted. Highlighted genes involved in GSH synthesis (MAT1A, SLC7A11, GSTO2, MGST, CTH), iron metabolism (HMOX1, FTH), and mevalonate pathway (HMGCR). Black dots: significantly upregulated genes (FC > 2, P < 0.05). **c,** Gene Set Enrichment Analysis (GSEA) dot plot highlighting significantly enriched GO-terms in siZNF354A cells. Gene count, gene ratio, and specific values indicated. **d**, GSEA plots for Biological Process (BP) and Cellular Component (CC) GO categories. **e,** Model overview of ZNF354A-regulated selenium-/thiol-dependent and independent pathways in phospholipid peroxide detoxification. ZNF354A targets highlighted in green. Main proteins/pathways upregulated by ZNF354A depletion are indicated (see Supplementary Table 3). In thiol-dependent pathways GPX4 converts phospholipid hydroperoxides (PL-OOH) to alcohols (PL-OH), dependent on glutathione (GSH) synthesis via cystine uptake and reduction. The methionine cycle contributes with precursors. In parallel the NAD(P)H/FSP1/ubiquinone system reduces peroxyl radicals in phospholipids (PLOO•). SLC7A11 (xCT), cystine/glutamate antiporter; TXNRD1, thioredoxin reductase-1; CTH, γ-cystathionase; MAT1A, methionine adenosyltransferase; GSTs, GSH-S-transferases; GSR, GSH-disulfide reductase; GPX4, glutathione peroxidase-4; GSSG, oxidized glutathione; FSP1, ferroptosis suppressor protein; CoQ10H2, ubiquinol; CoQ10(H), ubiquinone; SEPHS2, selenophosphate synthetase-2; FTH, ferritin heavy chain-1; HMGCR, 3-hydroxy-3-methylglutaryl-CoA reductase. Created with BioRender.com.

See methods or https://tronoapps.epfl.ch/web/krabopedia/ for full datasets

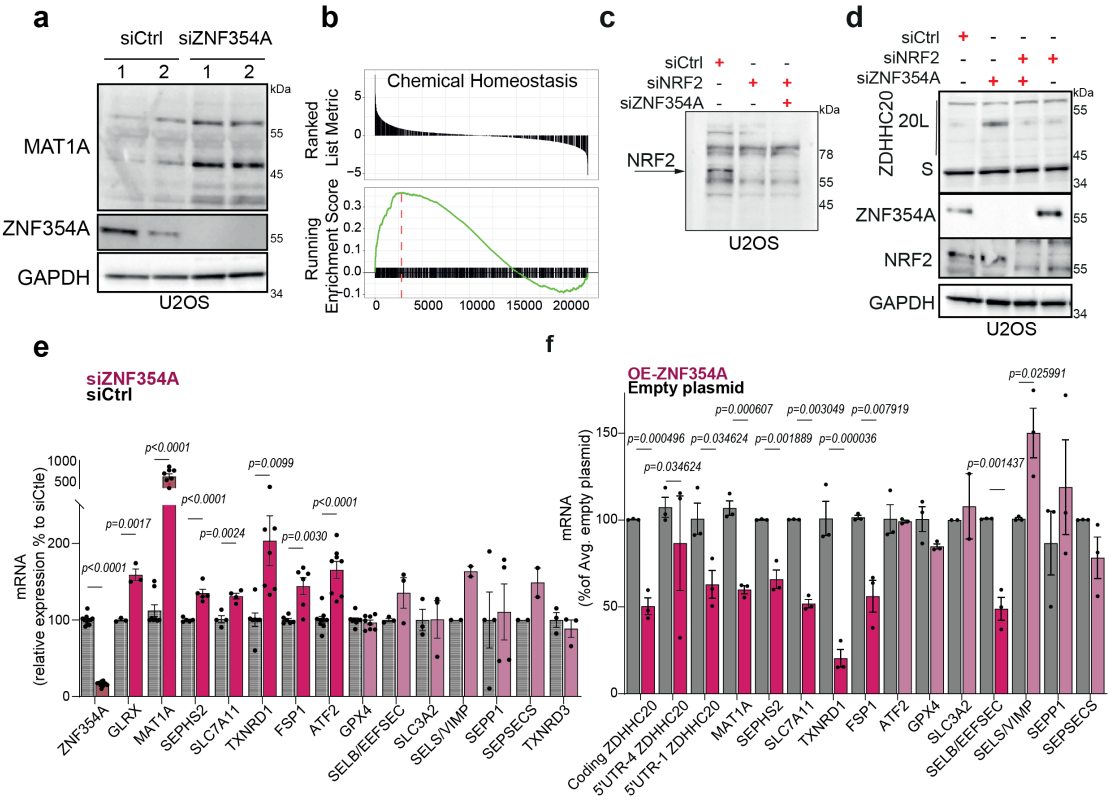

Supplementary Figure 4: ZNF354A is a regulator of antioxidant responses.
a, Western blot of MAT1A, ZNF354A and GAPDH (loading control) in TCE from U2OS cells treated 72h with 2 different RNAi control or against ZNF354A. **b,** GSEA plots of Chemical Homeostasis-Gene Ontology categories (Supplementary Table 2) from U2OS cells transfected with siCtrl or siZNF354A (72 h). **c,** mRNA quantification of indicated transcripts in U2OS cells transfected with siCtrl or siZNF354A (72 h). Mean ± SEM; each dot represents an independent experiment. Statistical analysis by two-way ANOVA, Sidak's test; *p* values compare to siControl. **d,** mRNA quantification of indicated transcripts in U2OS cells transfected 24 hours with Ctrl or ZNF354A expressing plasmids. Mean ± SEM; each dot represents an independent experiment. Statistical analysis by two-way ANOVA, Sidak's test; *p* values compare to empty plasmid. **e-f,** Western blots showing NRF2 (**f**), ZDHHC20 (Short-S, 20L isoforms), ZNF354A, and GAPDH (loading control) (**f**) in U2OS cells depleted of NRF2, ZNF354A, or both (siNRF2, siZNF354A, siNRF2/ZNF354A; 72 h).

541 **ZDHHC20L expression is induced by lipid peroxidation**

542 Since ZNF354A regulates genes involved in cellular responses to oxidation, we explored
543 whether oxidative damage could be the common primary trigger of the ZDHHC20L expression
544 observed following SARS-CoV-2 infection, pore-forming toxin treatment, colitis, and aging
545 (Fig. 1). When oxidative stress was induced by treating U2OS cells for 4-8 h with H_2O_2 at 50
546 μM, a significantly lower concentration than used to induce DNA damage [14], ZDHHC20L was
547 expressed in a dose-dependent manner (Fig. 5a).

548 We next tested whether ZDHHC20L expression could be specifically triggered by inducing the
549 accumulation of membrane lipid peroxides. These form when oxygen radicals interact with
550 PUFA-containing phospholipids[5,13,79]. Under physiological conditions, their accumulation is
551 avoided by the action of GPX4, the primary enzyme that detoxifies lipid peroxides, by reducing
552 them to lipid alcohols[23]. Treating cells with the covalent GPX4 inhibitor RSL3 (RAS-selective-
553 lethal-3)[25] induced ZDHHC20L expression in a dose-dependent manner (Fig. 5b). H_2O_2 and
554 RSL3 treatment also triggered phosphorylation of ATF2 (Fig. 5b), KAP-1, and ZNF354A
555 (Supplementary Fig. 5a). Silencing of GPX4 similarly led to ZDHHC20L expression (Fig. 5c).
556 Finally, since GPX4 requires GSH for its reduction, a third way of impairing its activity is to
557 block cystine uptake via SLC7A11 (system Xc^-). Erastin, a system Xc^- inhibitor [80], also induced
558 ZDHHC20L expression in a dose-dependent manner (Supplementary Fig. 5b).

559 Upon induction of lipid peroxidation, detoxification can also be performed chemically using
560 lipophilic peroxyl radical-trapping molecules such as Ferrostatin-1 (Fer-1)[81]. Ferrostatin-1
561 inhibited the H_2O_2-induced expression of ZDHHC20L in a dose-dependent manner (Fig. 5d).
562 Importantly, ferrostatin also inhibited aerolysin-induced ATF2 and KAP1 phosphorylation,
563 ZDHHC20L expression (Fig. 5e), and diminished aerolysin-induced cell death (Supplementary
564 Fig. 5c). Altogether, these observations demonstrate that lipid peroxide accumulation induces
565 ZDHHC20L expression, whereas inhibition of lipid peroxidation by Ferrostatin-1 prevents this
566 induction.

567 We next verified whether H_2O_2 could recapitulate the events triggered by aerolysin exposure
568 or SARS-CoV-2 infection. H_2O_2 treatment led to the phosphorylation of ATF2, KAP1 (on Ser-

569 473), and ZNF354A (on Ser-169), in a ferrostatin-dependent manner (Supplementary Fig. 5a).
570 H_2O_2-induced ZDHHC20L expression was prevented by the expression of the phospho-
571 deficient KAP1 S473A and ZNF354A S169A mutants (Supplementary Fig. 5d-f). The H_2O_2-
572 induced ATF2, KAP1 and ZNF354A phosphorylation and ZDHHC20L expression were p38-
573 and JNK-dependent (Fig. 6ab). Inhibition of ERK reduced ATF2 phosphorylation moderately,
574 diminished ZNF354A phosphorylation, but did not affect KAP1 phosphorylation or
575 ZDHHC20L expression (Fig. 6ab). ATM inhibition mildly reduced phosphorylation of all three
576 components and the expression of ZDHHC20L (Fig. 6ab). Finally, H_2O_2 treatment triggered
577 the detachment of KAP1 from ZNF354A, while phosphorylated ATF2 interacted with KAP1
578 (Fig. 6c).
579 Altogether, these observations demonstrate that H_2O_2 recapitulates the observations made with
580 aerolysin, and can trigger the expression of ZDHHC20L through the p38/JNK-dependent
581 phosphorylation of ATF2, KAP1 (Ser-473) and ZNF354A (Ser-169), and the disassembly of
582 the repressive complex.
583

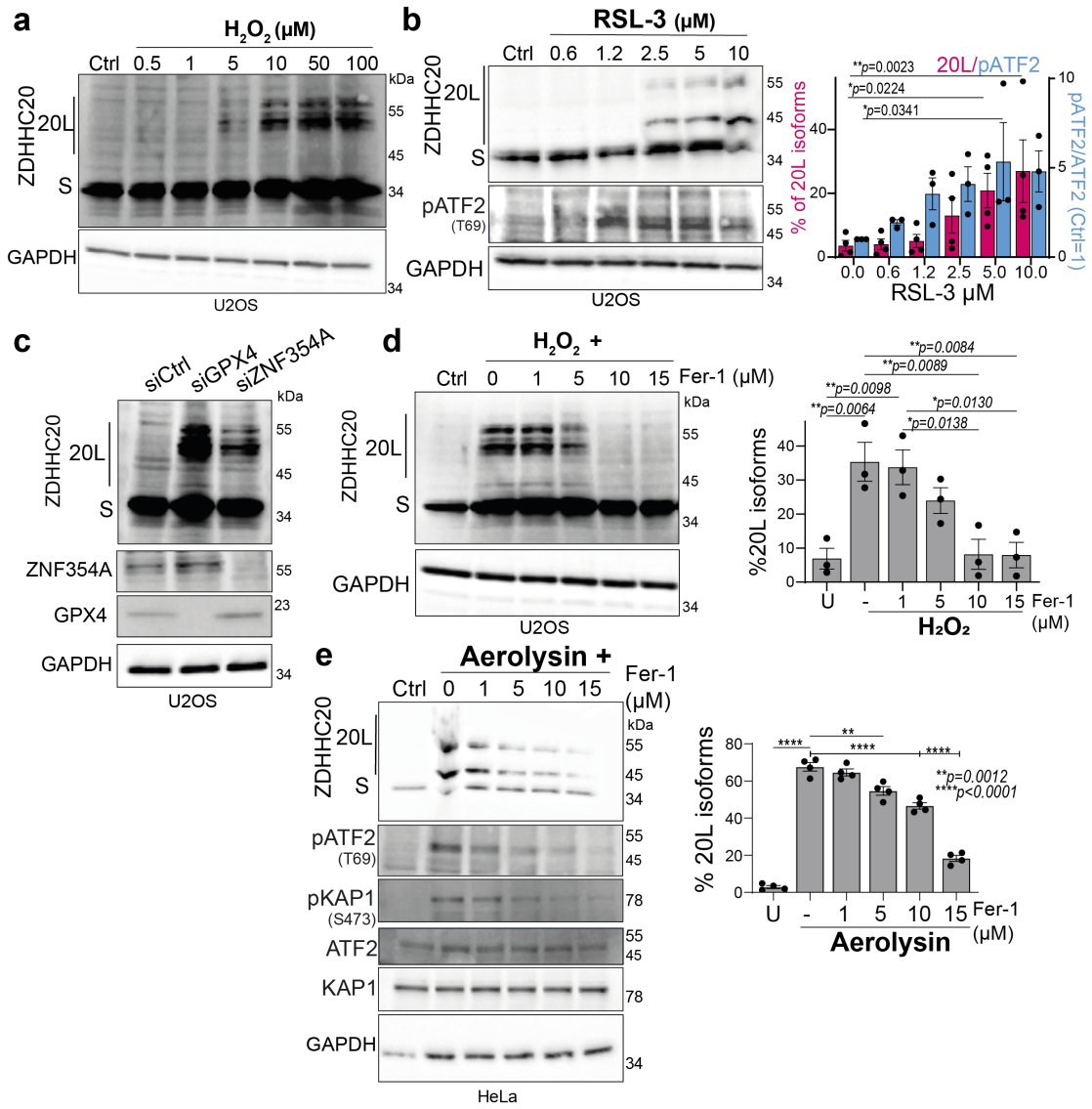

Figure 5. ZDHHC20L and ZNF354A respond to redox homeostasis and lipid peroxidation.

a–e, Western blot (WB) analysis of ZDHHC20 (Short and 20L isoforms) and GAPDH (loading control) in U2OS cells treated as follows: increasing concentrations of H_2O_2 (8 h) (a), increasing concentrations of RSL3 (b), siControl, siGPX4 or siZNF354A (72 h) (c), H_2O_2 (50 μM) with increasing concentrations of ferrostatin-1 (Fer-1) (d), and HeLa cells treated with proaerolysin (10 ng/ml, 1 h, washed, incubated additional 8 h) (e). Graphs in (b,d,e) show percentages of 20L isoform and (b) ATF2 levels. Mean ± SEM; each dot represents an independent experiment. Statistical analysis by two-way ANOVA, Tukey's test; *p* values as indicated.

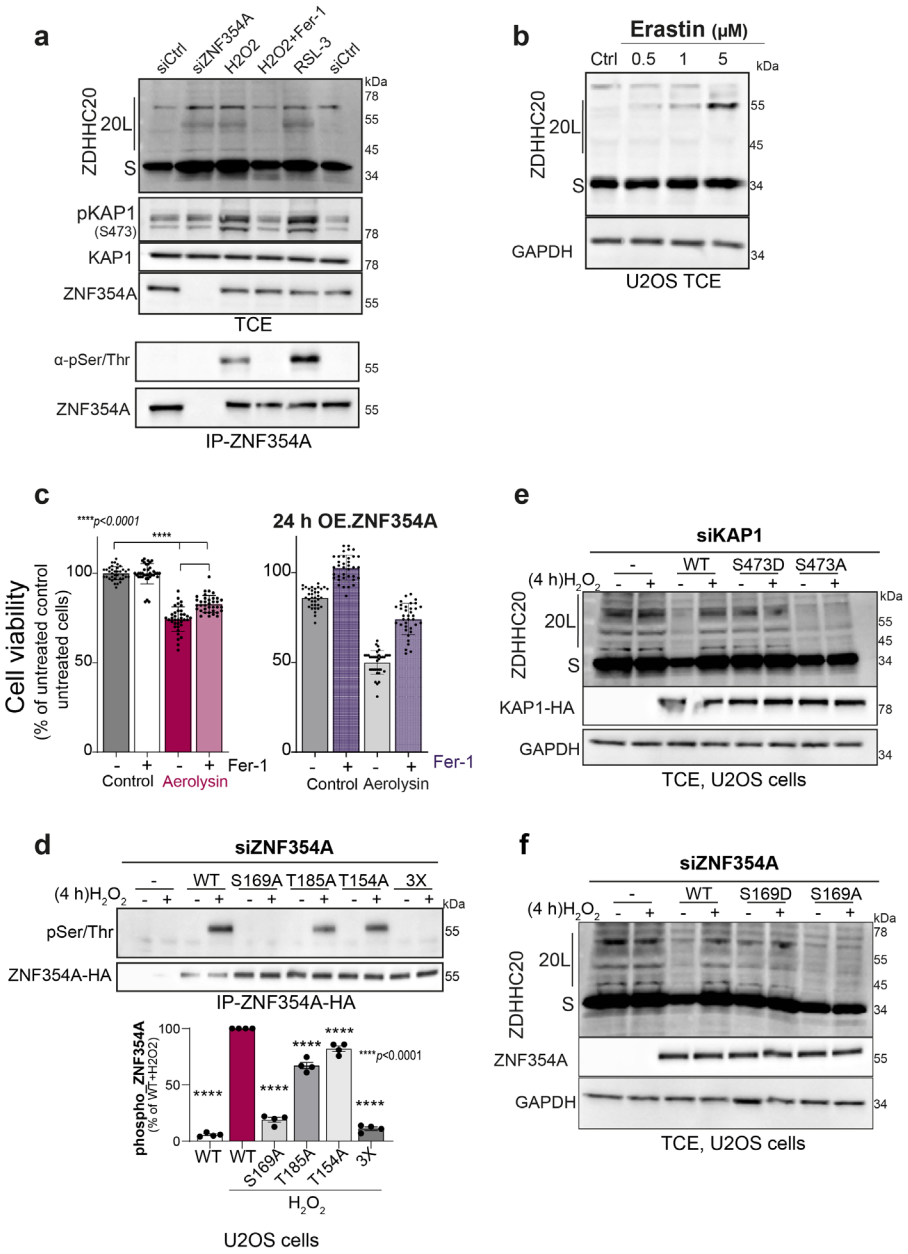

Supplementary Figure 5. ZDHHC20L and ZNF354A respond to redox homeostasis and lipid peroxidation.

a, Western blot (WB) of total cell extracts (TCE) and ZNF354A immunoprecipitates (IP) from U2OS cells (siCtrl or siZNF354A, 72 h) treated with H_2O_2 (50 μM, 7 h ± ferrostatin-1, Fer-1, 15 μM) or RSL3 (3 μM, 7 h). Blots show ZDHHC20 (20L and Short isoforms), phospho-KAP1, total KAP1, GAPDH (loading control), phospho-Ser/Thr proteins, and ZNF354A. **b,** WB (as in a) in TCE from U2OS cells treated with increasing concentrations of Erastin (16 h). **c,** Viability (ATP detection) of U2OS cells (Control or overexpressing ZNF354A, 24 h) ± Ferrostatin (15 μM) or/and proaerolysin (10 ng/ml, 1 h, washed, incubated additional 8 h last hours). Mean ± SD; representative assay (of three), n=36. ; *p* values compare to control plasmid, by two-way ANOVA, Sidak's test. **d**, IP-ZNF354A-HA in U2OS cells (siZNF354A, 72 h) overexpressing WT or phospho-mutant ZNF354A (3X mutant with all phospho-residues mutated to Ala), untreated or treated with H_2O_2 (50 μM, 4 h). Quantification of phospho-Ser/Thr/ZNF354A bands. Mean ± SEM; each dot represents an independent experiment (n=3). Statistical analysis by two-way ANOVA, Dunnett's test; *p* values compare H_2O_2-treated WT. **e,** WB (as in a) in U2OS cells (siKAP1, 72 h) expressing WT KAP1 or indicated phospho-mutants, untreated or treated with H_2O_2 (as in d). **f**, WB (as in d) in siZNF354A, 72h cells expressing WT or indicated phospho-mutant ZNF354A, treated as in (d).

614 **Stress-induced release of ZNF354A from regulatory loci**

615 Thus far, our data indicate that the repressive complex contains ATF2-SETDB1-KAP1-
616 ZNF354A and that upon lipid peroxidation-induced phosphorylation, KAP1 detaches from
617 ZNF354A. We next tested whether, under these conditions, ZNF354A is released from the
618 DNA. We performed genome-wide profiling of ZNF354A binding upon its overexpression in
619 K562 cells, treated or not with H_2O_2 for 4 hours (Supplementary Fig. 6ab). As a preamble, we
620 examined the genomic recruitment of this ZNF354A in untreated cells, and found it to be
621 consistent with that previously recorded in 293T cells, with 20% of K562 peaks (306/1558)
622 already identified in this other cell line (Supplementary Fig. 6c), representing a significant
623 overlap compared to randomized regions (permutation test: 100 permutations, empirical *P*-
624 value = 0) (Fig. 6d). Additionally, the ZNF354A-HA signal intensity over peaks was highly
625 consistent between the ChIP-seq experiments in the two cell lines (Fig. 6d). H_2O_2 treatment
626 induced a severe drop in the number of ZNF354A-HA peaks (521 vs. 1558 peaks), and a
627 significantly lower overlap with the peaks previously identified in HEK293T (6% vs. 20%,
628 Fisher's exact test, *P*-value = 2.465e-16) (Fig. 6d). Moreover, ZNF354A occupancy was
629 significantly reduced at the majority of identified peaks (Fig. 6e, Supplementary Fig. 6c). That
630 ZNF354A detaches from the DNA sites upon H_2O_2 treatment was further confirmed by ChIP-
631 RT-qPCR for specific peaks associated with selected redox target genes, including *MAT1A*,
632 *SELS*, *TXNRD1* and *ZDHHC20* (Fig. 6f). Together, these findings demonstrate that H_2O_2
633 treatment leads to the chromatin eviction of ZNF354A, to allow expression of previously
634 repressed genes, notably those involved in antioxidant response.

635

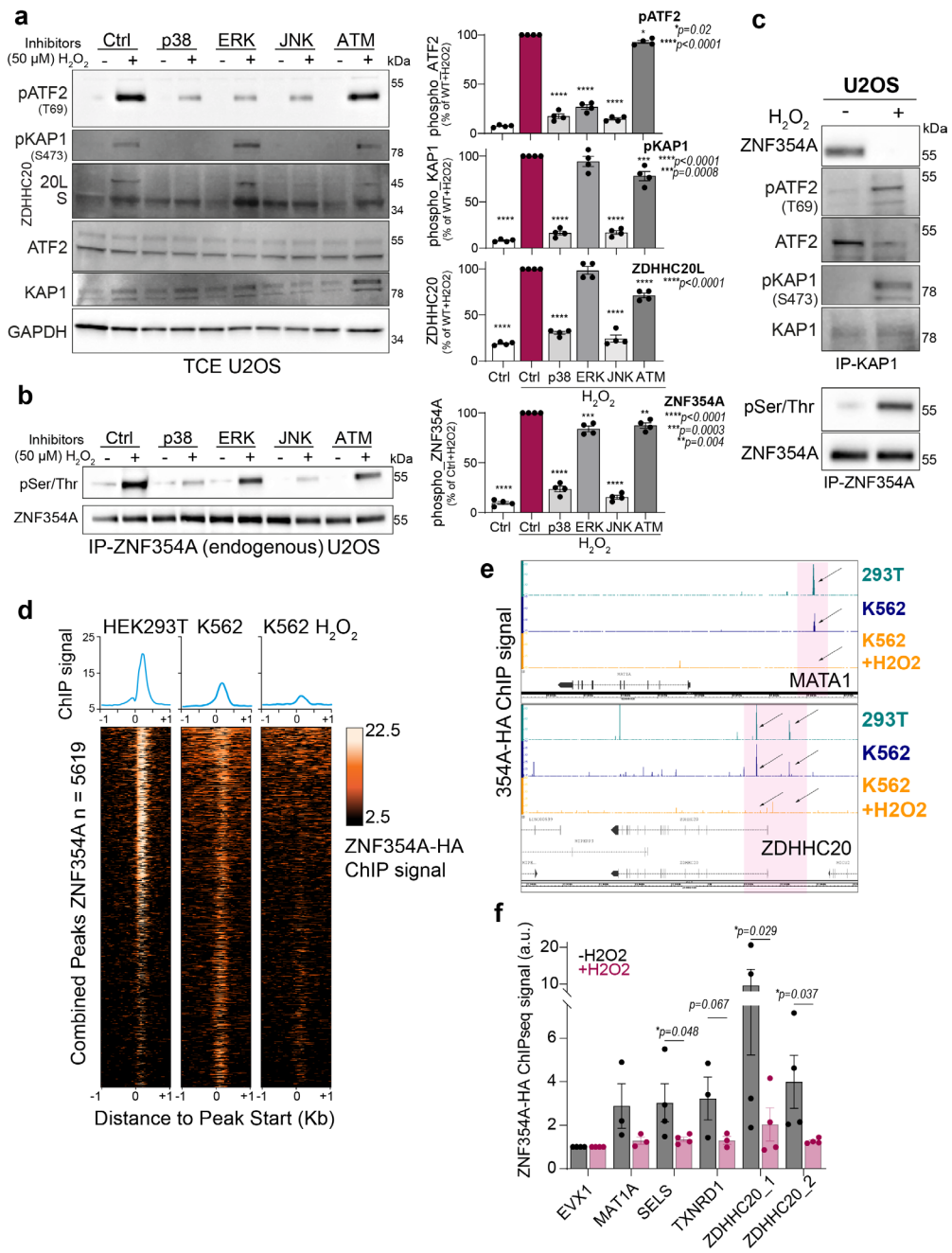

Figure 6. H_2O_2-dependent regulation of the ATF2-KAP1-ZNF354A epigenetic complex. **a,b,** Western blots of U2OS cells treated with H_2O_2 (50 μM, 4 h) in presence of indicated kinase inhibitors. Blots show ZDHHC20 (Short-S, 20L isoforms), phospho-KAP1 (S473), phospho-ATF2 (T69), total KAP1 and ATF2, GAPDH (loading control) (a), and phospho-Ser/Thr proteins with total ZNF354A (b). Quantification of phospho-ATF2, phospho-KAP1, ZDHHC20L (a), and phospho-Ser/Thr/ZNF354A (b) bands. Mean ± SEM; each dot represents an independent experiment (n=4). Statistical analysis by two-way ANOVA, Dunnett's test; *p* values compare treated conditions to untreated control (Ctrl). **c,** Western blots as in (a), in KAP1 or ZNF354A immunoprecipitates from H_2O_2-treated cells as in (a). **d,** Heat maps of ChIP-seq profiles centered on ZNF354A-HA peaks (±1 kb) showing enrichment in HEK293T and K562 cells under untreated and H_2O_2-treated conditions (50 μM, 4 h). **e,** IGV browser screenshots illustrating selected ZNF354A ChIP-seq peaks (arrows) within *MAT1A*, and *ZDHHC20* loci from cells treated as described in (d). **f.** ChIP–qPCR quantification of ZNF354A-HA peaks at indicated gene regions (two peaks for *ZDHHC20*; *EVX1* used as control). Results mean ± SEM; dots represent independent experiments (n = 3). *p* values vs untreated (−H_2O_2), two-way ANOVA, Tukey's correction.

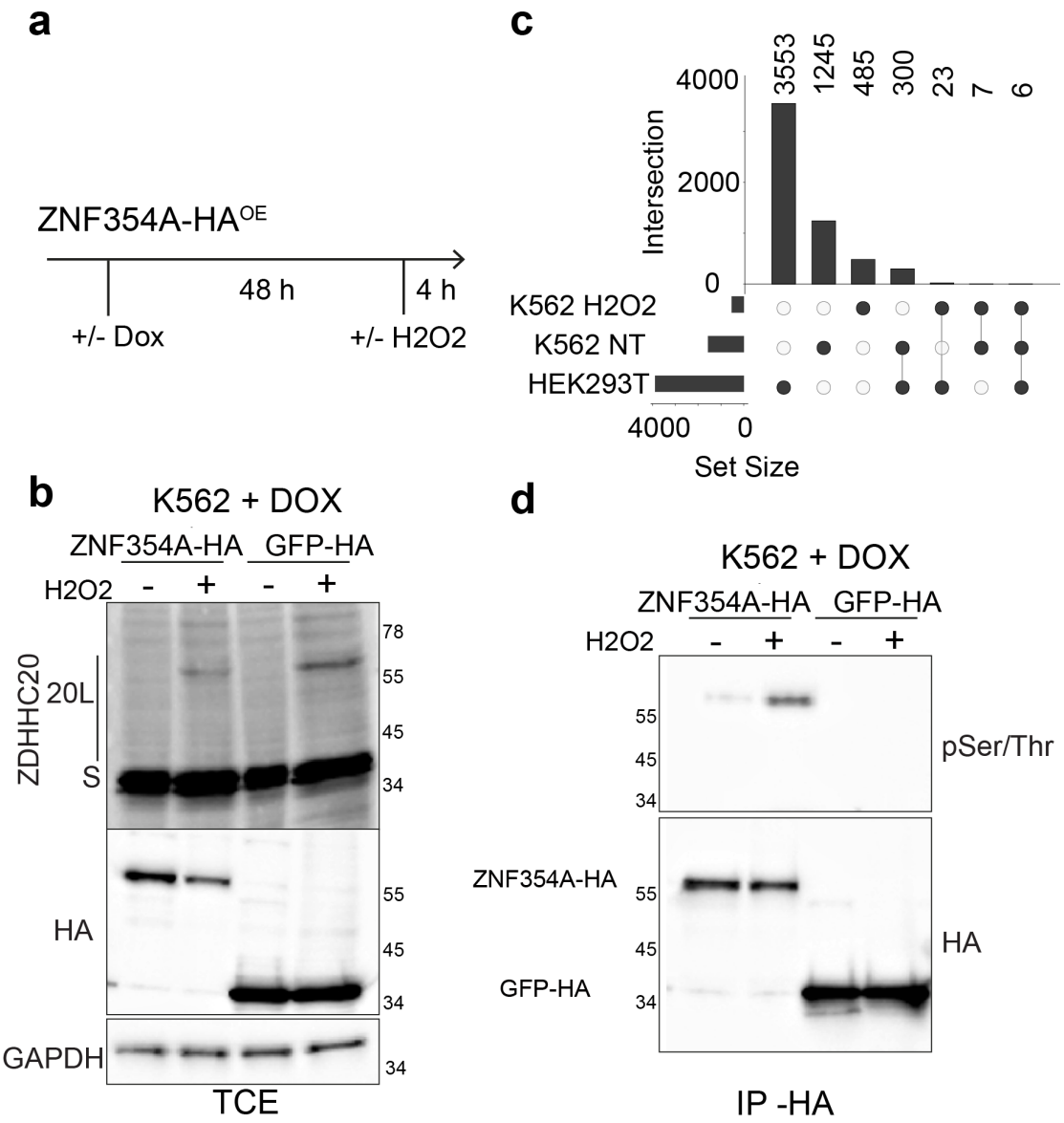

Supplementary Figure 6. H_2O_2-dependent regulation of the ATF2-KAP1-ZNF354A epigenetic complex.

a, Schematic of ChIP-seq experimental setup using K562 cells stably expressing control GFP-HA or ZNF354A-HA. ZNF354A expression was induced with doxycycline (1 µg/ml, 48 h) and verified by western blot (WB). Cells were untreated or treated with H_2O_2 (50 µM, 4 h). **b**, WB analysis of total cell extracts (TCE) showing ZDHHC20 (Short and 20L isoforms), HA-tagged protein expression, and GAPDH (loading control). HA immunoprecipitates (IP-HA) from K562 cells (a) were analyzed for HA-tagged proteins and phospho-Ser/Thr proteins. **c,** UpSet plot showing overlaps of ZNF354A ChIP-seq peaks identified in HEK293T cells (HEK293T), untreated K562 cells (K562_NT), and H_2O_2-treated K562 cells (K562_H_2O_2; 50 µM, 4 h). Horizontal bars indicate total peaks per condition; vertical bars represent intersections of shared peaks between conditions.

666 **ZNF354A acts as a regulator of ferroptosis sensitivity**

667 To test the functional relevance of ZNF354A in controlling an antioxidant gene program, we
668 tested whether silencing ZNF354A expression would protect cells from lipid peroxidation-
669 induced death. We first monitored lipid peroxidation, using two different fluorescent probes –
670 C11-BODIPY and LiperFluo, the latter specifically detecting oxidized phospholipids[82,83].
671 Silencing ZNF354A expression led to a decrease in lipid peroxide levels (Fig. 7ab). ZNF354A-
672 depleted cells also showed a moderate reduction in lipid peroxide accumulation following
673 GPX4 inhibition with RSL3 compared to controls (Fig. 7ab). This suggests that in the absence
674 of ZNF354A, cells have an increased ability to prevent the formation or detoxify lipid
675 peroxides. Consistently, staining with the membrane-impermeant dye propidium iodide (PI)
676 indicated that plasma membrane integrity was more preserved in ZNF354A-depleted cells than
677 in control cells (Fig. 7c). Finally, cell viability was monitored by measuring ATP levels,
678 following RSL3 or H_2O_2 treatment. Depletion of ZNF354A by siRNA led to a marked increase
679 in viability in response to both RSL3 and H_2O_2 (Fig. 7d), as well as the cystine import inhibitors
680 Erastin (Supplementary Fig. 7a).

681 These observations show that silencing ZNF354A expression reduces the cellular sensitivity to
682 ferroptosis. We next tested whether ZNF354A overexpression would sensitize them. We
683 designed inactive ZNF354A mutants by mutating the ZFP-KRAB-A box of ZNF354A, a well-
684 conserved interaction domain of KZFP with KAP1 (Supplementary Fig. 7b) [60], composed in
685 particular of D18, E27, N45 and E46 [60,84,85]. We generated a quadruple ZNF354A mutant
686 construct with arginine substitutions of D18 and E27, or arginine and alanine substitutions of
687 N45 and E46 (Supplementary Fig. 7b). While the mutant was expressed at WT levels, as
688 predicted it failed to interact with KAP1 (Supplementary Fig. 7c). Overexpression of
689 $ZNF354A^{WT}$, but not $ZNF354A^{Mut}$, led to an increase in oxidized phospholipids (Fig. 7e,
690 Supplementary Fig. 7d), associated with significant cell death starting at 48 hours (Fig. 7f). Cell
691 viability could be rescued by ferrostatin-1, to levels that depended on the frequency of Fer-1
692 treatment (Fig. 7ef, Supplementary Fig. 7e-g). When ZNF354A was overexpressed to levels
693 that led to 85% cell death after 4 days, daily administration of Fer-1 reduced death to 22±16%

694 (Supplementary Fig. 7g). Comparable protection was observed by treating cells with N-
695 acetylcysteine amide (NAC), a cell-permeable cysteine derivative that restores GSH
696 production, which reduced cell death to 12±5% (Supplementary Fig. 7g). The treatment with
697 both Fer-1 and NAC reduced cell death to 7±1% (Supplementary Fig. 7g). Thus, cell death
698 induced by ZNF354A overexpression is predominantly triggered by lipophilic ROS (≈75%
699 contribution), with a minor contribution (<20%) by cytosolic or other ROS. Altogether, these
700 observations show that ZNF354A silencing prevents excessive lipid peroxide accumulation and
701 protects from cell death, while overexpression does the opposite.
702 As mentioned earlier, lipid peroxide detoxification relies mostly on GPX4 and FSP1, the latter
703 operating in a GSH-independent manner via the NAD(P)H/FSP1/CoQ10 axis. We tested
704 whether cell death induced by ZNF354A overexpression could be rescued by co-
705 overexpression with either GPX4 or FSP1. FSP1 restored the viability of ZNF354A-
706 overexpressing cells, consistent with the effect of Fer-1, while GPX4 did not (Fig. 7g). As this
707 might reflect insufficient levels of GSH, we supplemented cells with NAC, which was
708 sufficient to rescue ZNF354A-induced cell death, indicating that cellular GPX4 levels were not
709 limiting (Fig. 7g). We then measured GSH levels to test whether they are influenced by
710 ZNF354A. Silencing ZNF354A increased cellular GSH levels, as did to a greater extent
711 silencing of GPX4 expression (Fig. 7h). Conversely, overexpression of ZNF354A led to a
712 decrease in GSH (Fig. 7h). Thus, ZNF354A appears to act as a rheostat of cellular GSH levels.
713 The induction of ferroptosis is of major therapeutic interest to kill cancer cells[25]. To probe the
714 relevance of the ZNF354A pathway in predicting and controlling the sensitivity of tumor cell
715 lines to ferroptosis, we first monitored the phosphorylation of ZNF354A. Only the cells
716 expressing ZDHHC20L, i.e., HEPG2, MCF7, and HCT116 (Fig. 1a, 7i), showed
717 phosphorylated ZNF354A, despite similar ZNF354A expression levels in all cells (Fig. 7i). We
718 next submitted all cell lines to H_2O_2 or RSL3 treatment and monitored cell viability. Consistent
719 with our hypothesis, HEPG2, MCF7, and HCT116 cells were more resistant to RSL3 and H_2O_2,
720 compared to all other cancer lines (Fig. 7j).

721 Altogether, these findings indicate that ZNF354A regulates cellular GSH levels and lipid
722 detoxification capacity, thereby modulating cellular sensitivity to lipid peroxidation-induced
723 cell death pathways, in particular ferroptosis. In the context of cancer, the presence of phospho-
724 ZNF354A or ZDHHC20L therefore appears predictive of tumor cell sensitivity to ferroptosis-
725 inducing drugs.
726

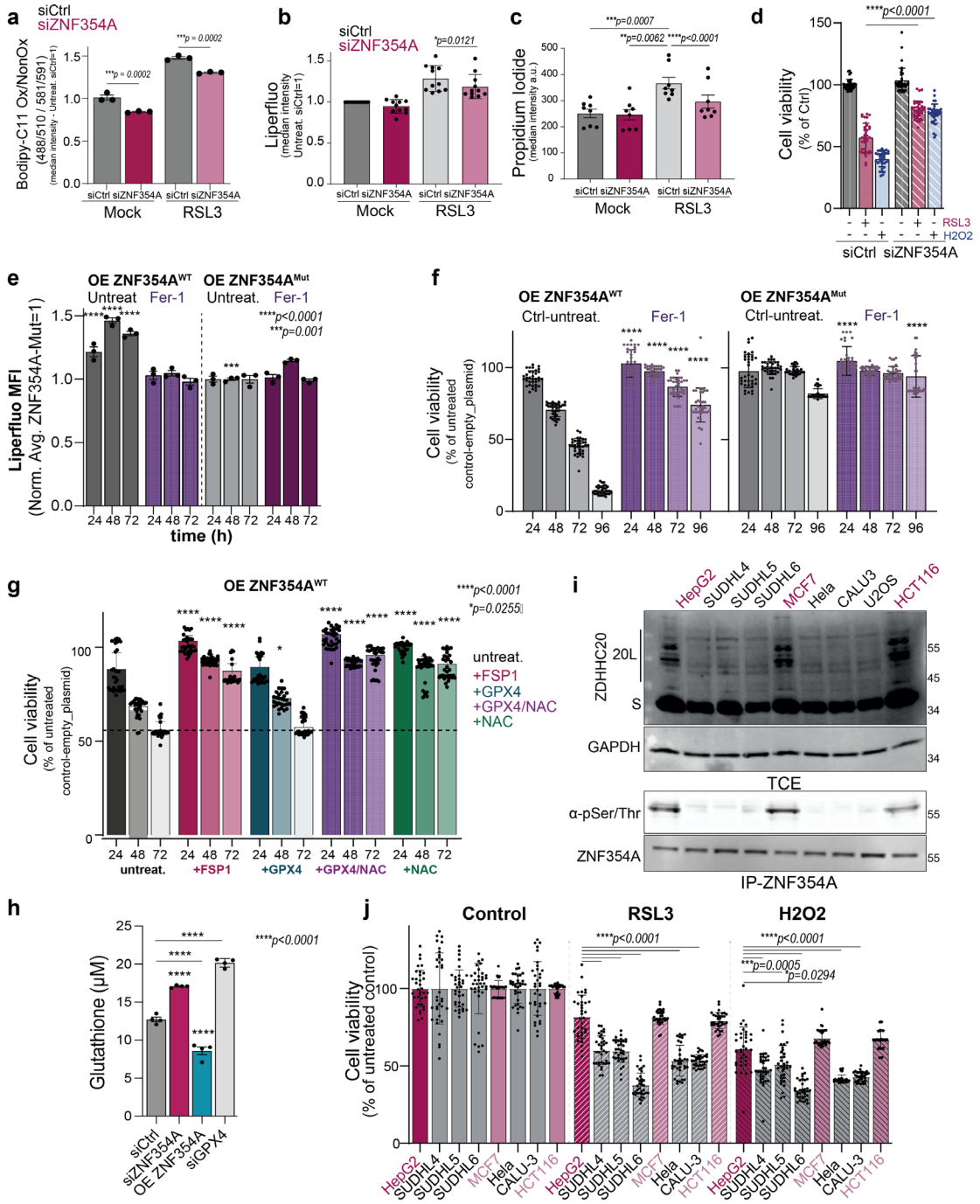
a
siCtrl
siZNF354A
Bodipy-C11 Ox/NonOx (488/510 / 581/591) (median intensity - Untreat. siCtrl=1)
***p = 0.0002
***p = 0.0002
siCtrl siZNF354A siCtrl siZNF354A
Mock
RSL3
b
siCtrl
siZNF354A
Liperfluo (median intensity Untreat. siCtrl=1)
*p=0.0121
siCtrl siZNF354A siCtrl siZNF354A
Mock
RSL3
c
Propidium Iodide (median intensity a.u.)
***p=0.0007
**p=0.0062 ****p<0.0001
siCtrl siZNF354A siCtrl siZNF354A
Mock
RSL3
d
Cell viability (% of Ctrl)
****p<0.0001
RSL3
H2O2
siCtrl siZNF354A
e
OE ZNF354A^WT
OE ZNF354A^Mut
Untreat Fer-1
Untreat. Fer-1
Liperfluo MFI (Norm. Avg. ZNF354A-Mut=1)
****p<0.0001
***p=0.001
time (h)
f
OE ZNF354A^WT
OE ZNF354A^Mut
Ctrl-untreat.
Fer-1
Cell viability (% of untreated control-empty_plasmid)
g
OE ZNF354A^WT
****p<0.0001
*p=0.0255
Cell viability (% of untreated control-empty_plasmid)
untreat.
+FSP1
+GPX4
+GPX4/NAC
+NAC
i
HepG2 SUDHL4 SUDHL5 SUDHL6 MCF7 Hela CALU3 U2OS HCT116
ZDHHC20
20L
S
GAPDH
TCE
α-pSer/Thr
ZNF354A
IP-ZNF354A
h
Glutathione (µM)
****p<0.0001
siCtrl
siZNF354A
OE ZNF354A
siGPX4
j
Control
RSL3
H2O2
Cell viability (% of untreated control)
****p<0.0001
****p<0.0001
***p=0.0005
*p=0.0294
HepG2 SUDHL4 SUDHL5 SUDHL6 MCF7 Hela CALU-3 HCT116

741 **Figure 7. ZNF354A controls lipid peroxide detoxification and sensitivity to ferroptosis.**
742 **a–c**, Lipid peroxides measured by flow cytometry (Bodipy-C11, Liperfluo) and membrane permeability
743 (propidium iodide) in U2OS cells transfected with siControl or siZNF354A (72 h) ± RSL3 (3 μM, 24 h).
744 Mean ± SEM; dots indicate independent experiments. ; *p* values compare to siControl, by two-way
745 ANOVA, Tukey's test. **d**, Viability (ATP detection) of U2OS cells (siControl or siZNF354A, 72 h) ±
746 RSL3 (3 μM) or H_2O_2 (50 μM, 16 h). Mean ± SD; representative assay (of three), n=36. ; *p* values
747 compare to siControl, by two-way ANOVA, Sidak's test. **e,f,** Lipid peroxidation (**e**) and viability (**f**) of
748 U2OS cells expressing wild-type (WT) or KRAB-binding mutant ZNF354A ± ferrostatin-1 (Fer-1, 15
749 μM, added at 0 and 48 h post-transfection). Mean ± SEM and dots represent independent experiments
750 (e). Mean ± SD normalized to untreated controls (empty plasmid) of representative assay (of three) n=33
751 (f). *p* values compare untreated controls vs Fer-1, by two-way ANOVA, Sidak's test. **g**, Viability (as in
752 f) of HeLa cells expressing ZNF354A, supplemented with FSP1, GPX4, GPX4 + N-Acetyl-Cysteine
753 (NAC, 1 mM), or NAC alone. Mean ± SD; representative assay (of three), n=33. ; *p* values compare
754 untreated controls at each time point, by two-way ANOVA, Sidak's test. **h**, The cellular level of GSH
755 was measured in control cells and upon silencing of ZNF354A or GPX4 and upon over expression of
756 ZNF354A. Mean ± SEM. **i**, Western blot of total cell extracts (TCE) and ZNF354A immunoprecipitates
757 (IP) from indicated cancer cells, showing Short-S (42 kDa), 20L isoforms (~49, 62, 69 kDa), GAPDH
758 (loading control), total ZNF354A, and phospho-Ser/Thr proteins. **j**, Viability (as in d) of cancer cells
759 (from h) ± RSL3 (3 μM) or H_2O_2 (50 μM, 16 h). Viability normalized to untreated controls (100%).
760 Mean ± SD; representative assay (n=35). *p* values compare each condition to HepG2 reference, by two-
761 way ANOVA, Dunnett's test.
762
763

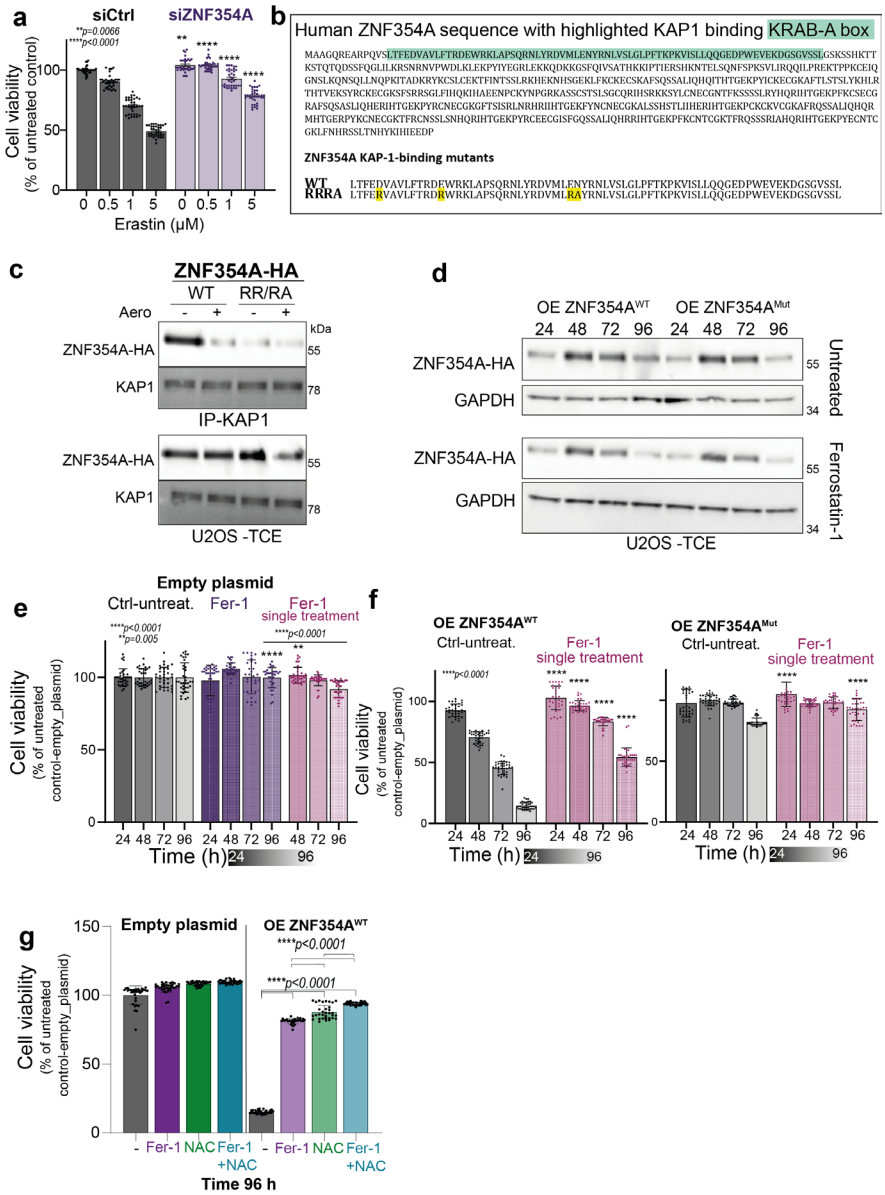

Supplementary Figure 7. ZNF354A controls lipid peroxide detoxification and sensitivity to ferroptosis.

a, Viability (ATP detection) of U2OS cells transfected with siControl or siZNF354A (72 h), treated with increasing concentrations of Erastin (16 h). Mean ± SD; representative assay (of three), n=36. Statistical analysis by two-way ANOVA, Sidak's test; P values compare siControl vs siZNF354A. **b**, ZNF354A protein sequence with KAP1-binding KRAB-A box (green) and KAP1-binding mutantations. **c**, Immunoprecipitation (IP) of endogenous KAP1 from U2OS cells overexpressing wild-type (WT) HA-tagged ZNF354A or KAP1-binding mutant (RR/RA), untreated or treated with proaerolysin (10 ng/ml, 1 h, 37 °C), followed by washing and additional incubation (8 h, 37 °C). Western blots show co-immunoprecipitated proteins (CoIP) and total cell extracts (TCE). **d–f**, U2OS cells overexpressing WT or KRAB-binding mutant ZNF354A, treated ± ferrostatin-1 (Fer-1, 15 μM) at time 0 and 48 h post-transfection. d, Western blot analysis of TCEs showing ZNF354A-HA and GAPDH. **e,f**, Cell viability (ATP detection) in U2OS cells transfected with empty plasmid (e) or ZNF354A WT/KRAB-binding mutant (**f**), treated ± Fer-1 (single treatment, 15 μM at time 0). Results normalized to untreated empty plasmid controls (set as 100%). Mean ± SD; representative assay (of three), n=35. Statistical analysis by two-way ANOVA, Sidak's test; p values compare untreated controls vs Fer-1 at each time point. **g**, Cell viability (ATP detection) in U2OS cells transfected with empty plasmid (e) or ZNF354A WT, treated ± Fer-1 (everyday treatment, 15 μM), or NAC (1mM everyday) or both treatments together. Results normalized to untreated empty plasmid controls (set as 100%). Mean ± SD; representative assay (of three), n=36. Statistical analysis by two-way ANOVA, Sidak's test; p values compare untreated vs treated.

785 **ZDHHC20L is an effector of the ZNF354A-mediated pathway**

786 In this study, we have so far used the expression of ZDHHC20L as a proxy to decipher the
787 ZNF354A-mediated pathway. We initially identified ZDHHC20L in SARS-CoV-2-infected
788 cells and could show that ZDHHC20L greatly outperforms the canonical enzyme in modifying
789 the envelope glycoprotein Spike[37,38]. We postulated that the virus had hijacked a stress response
790 pathway—presumably activated to fight infection—for its own benefit. Here, we hypothesized
791 that ZDHHC20L may act as a bona fide effector of the ZNF354A-mediated pathway, with a
792 role in redox homeostasis. To explore this possibility, we sought to identify potential redox-
793 regulatory substrates of ZDHHC20L. Given the central role of GPX4 in detoxifying lipid
794 peroxides and protecting against ferroptosis, we hypothesized that ZDHHC20L might regulate
795 GPX4 through this modification. During the course of our study, two reports were published
796 indicating that S-acylation of GPX4 is critical for its function in controlling cellular sensitivity
797 to ferroptosis [86,87]. The first study showed that GPX4 undergoes acylation by ZDHHC20 on
798 Cys-66[86], while the second proposed acylation by ZDHHC8 on Cys-75[87]. Our screen of the 23
799 human ZDHHC enzymes, first tested in mixes of siRNA[38], showed that only Mix 3 led to a
800 marked decrease in GPX4 ^{3}H-palmitate incorporation (Fig. 8ab). The enzymes targeted by Mix
801 3, namely ZDHHC9, 14, 18, and 20, were subsequently tested individually. Only ZDHHC20
802 modified GPX4 in our cellular system (Fig. 8cd). We further confirmed S-acylation using a
803 click chemistry-based approach, so-called Click Acyl-PEG assay [88], which involves labeling
804 cells with a clickable palmitate analogue, and subsequently labeling the added acyl chains *in*
805 *vitro* with azide-PEG to induce a band shift detected by SDS-PAGE and Western blotting. A
806 clear GPX4 band shift towards two upper bands could be observed in control HEK293T cells,
807 which was absent in the corresponding ZDHHC20 KO line (Fig. 8e). The double band shift is
808 indicative of acylation on more than one cysteine, suggesting that both reported cysteines at
809 positions 66 and 75 could be simultaneously subject to S-acylation[86,87].

810 We next tested the ability of the long isoform ZDHHC20L to modify GPX4 and found that it
811 was more efficient than the canonical enzyme in promoting GPX4 acylation (Fig. 8fg). Given
812 the stress-induced expression of ZDHHC20L and its proposed role in redox homeostasis, we

813 next asked whether oxidative stress conditions could modulate GPX4 acylation. Remarkably,
814 H_2O_2 treatment had a major effect on GPX4 acylation, as evidenced by a marked increase in
815 ^{3}H-palmitate incorporation into GPX4 (Fig. 8h).
816 Because GPX4 activity depends on GSH, and its knockdown increases GSH levels (Fig. 7h),
817 we asked whether ZDHHC20 influences cellular GSH levels. Similar to GPX4 and ZNF354A,
818 ZDHHC20 knockdown elevated intracellular GSH (Fig. 8i). This redox imbalance was fully
819 corrected by re-expression of ZDHHC20L, whereas the canonical isoform had a more modest
820 effect (Fig. 8i). Importantly, ZDHHC20L conferred a marked survival advantage: loss of
821 ZDHHC20 impaired cell viability, consistent with recent findings[86], which was rescued by
822 ZDHHC20L and only partially by the canonical form (Fig. 8j). Finally, ZDHHC20L-expressing
823 cells were significantly more resistant to H_2O_2-induced oxidative stress when compared to cells
824 expressing the canonical isoform or lacking ZDHHC20 (Fig. 8j).
825 Altogether, these findings demonstrate that ZDHHC20 contributes to cellular redox
826 homeostasis, and that ZDHHC20L outperforms the canonical isoform. This identifies
827 ZDHHC20L as a functional effector of the LORD pathway that protects cells against oxidative
828 stress.
829
830
831
832
833

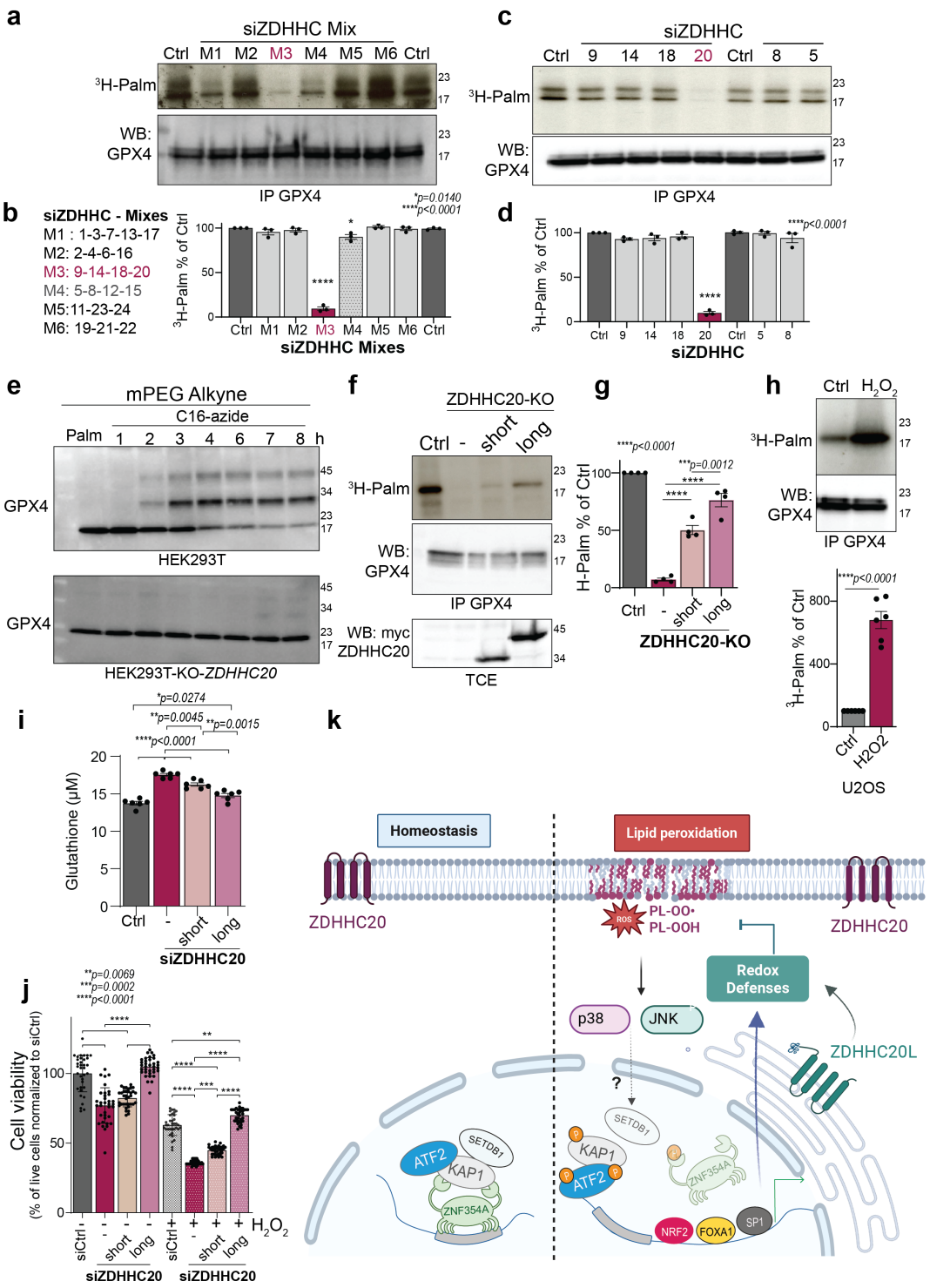
a
siZDHHC Mix
Ctrl M1 M2 M3 M4 M5 M6 Ctrl
3H-Palm
WB: GPX4
IP GPX4
b
siZDHHC - Mixes
M1 : 1-3-7-13-17
M2: 2-4-6-16
M3: 9-14-18-20
M4: 5-8-12-15
M5:11-23-24
M6: 19-21-22
3H-Palm % of Ctrl
siZDHHC Mixes
c
siZDHHC
Ctrl 9 14 18 20 Ctrl 8 5
d
siZDHHC
e
mPEG Alkyne
C16-azide
Palm 1 2 3 4 6 7 8 h
GPX4
HEK293T
HEK293T-KO-ZDHHC20
f
ZDHHC20-KO
Ctrl - short long
WB: myc ZDHHC20
TCE
g
H-Palm % of Ctrl
ZDHHC20-KO
h
Ctrl H2O2
U2OS
i
Glutathione (µM)
siZDHHC20
j
Cell viability
(% of live cells normalized to siCtrl)
siZDHHC20
k
Homeostasis
Lipid peroxidation
ZDHHC20
PL-OO•
PL-OOH
Redox Defenses
p38
JNK
ZDHHC20L
ATF2
SETDB1
KAP1
ZNF354A
NRF2
FOXA1
SP1

840 **Figure 8: ZDHHC20L is an effector of the LORD pathway.**

841 **a–d.** Incorporation of ^{3}H-palmitic acid (^{3}H-palm) in GPX4 from U2OS cells silenced for 72 h with
842 pooled (a) or individual (c) ZDHHC siRNAs. Cells were metabolically labeled for 3 h at 37 °C with ^{3}H-
843 palm; GPX4 was immunoprecipitated (IP-GPX4), resolved by SDS–PAGE, and analyzed by Western
844 blot (WB) and autoradiography (^{3}H-palm). The levels of ^{3}H-palm incorporation in control RNAi (Ctrl)
845 were set to 100% and results are mean ± SEM, and each dot represents an independent experiment (n=3).
846 *p* values compare siCtrl, two-way ANOVA, Dunnett's test. **e.** HEK WT or ZDHHC20-KO cells were
847 incubated with 100 µM C16:0-azide for the indicated times or with palmitic acid for 8 h. Incorporated
848 C16:0-azide was detected by click chemistry with alkyne-mPEG 5K (200 µM), followed by SDS–PAGE
849 and WB for GPX4. Results are representative of three independent experiments. **f–h**. same as in a, for **f,**
850 HEK WT (Ctrl) or ZDHHC20-KO cells, recomplemented with empty vector or short/long ZDHHC20 or
851 **h,** U2OS cells left untreated or treated for 4 h with 50 µM H_2O_2. For f, Myc-ZDHHC20 expression was
852 confirmed by WB. The levels of ^{3}H-palm incorporation were set to 100% in Control-WT cells for g, or
853 untreated control cells, in h. Results are mean ± SEM, and each dot represents an independent experiment
854 (g, n=4 and h, n=6). *p* values comparing to Ctrl or as indicated by, g, two-way ANOVA, Tukey's test,
855 and h, Student's t-test. **i.** Cellular glutathione measured in U2OS cells, siCtrl or siZDHHC20 (72 h) alone
856 or recomplemented with short/long ZDHHC20 (24 h). Data are mean ± SEM from one of three
857 independent experiments (n=6). *p* values by, two-way ANOVA, Tukey's test **j.** Viability assessed using
858 Promega Glo ATB detection in U2OS cells as in i, treated as in h. Data are mean ± SEM from one of
859 three independent experiments (n=36 replicates). *p* values by, two-way ANOVA, Tukey's test **k.**
860 Proposed Model: Under homeostasis, ATF2–SETDB1–KAP1–ZNF354A repress antioxidant genes.
861 Lipid peroxide accumulation activates p38/JNK signaling, leading to ZNF354A dissociation and
862 induction of antioxidant responses.
863

864

865

866 **Discussion**

867 This study uncovers an epigenetically controlled stress-response pathway that protects cells
868 from the harmful accumulation of membrane lipid peroxides. We term this pathway LORD
869 (Lipid Oxygen Radical Defense) (Fig. 8k). In addition to regulating the expression of
870 antioxidant genes, LORD also regulates the activity—but not the transcription—of GPX4,
871 enhancing the cell's ability to detoxify lipid peroxides, preserve membrane integrity, and
872 modulate susceptibility to ferroptosis.

873 Under basal conditions, the transcriptional regulator ZNF354A, a central LORD component,
874 represses numerous antioxidant defense genes, acting as a controller of lipid quality and
875 membrane damage repair. ZNF354A is ubiquitously expressed, as shown by GTEx Portal data
876 (https://www.gtexportal.org/home/), with its lowest expression in the liver—a tissue naturally
877 exposed to oxidative stress, potentially reflecting a reduced need to repress antioxidant
878 programs. In contrast, expression is high in the kidney, consistent with early reports in rats,
879 where it was identified as Kid-1 (kidney, ischemia, and developmentally regulated gene 1)[89–
880 91]. Interestingly, in the rat kidney, ZNF354A expression drops to undetectable levels upon
881 reperfusion after ischemia, suggesting LORD pathway activation during reoxygenation. Our
882 genomic liftover analysis indicates that the mouse ortholog ZFP354A may also bind near
883 antioxidant response genes, making it important to examine whether these regulatory networks
884 are conserved across species and shaped by the distribution of transposable elements, in
885 particular LINE-1.

886 Mechanistically, ZNF354A is part of a repressive complex that includes the global epigenetic
887 regulator KAP1and the H3K9 methyltransferase SETDB1, as for many KZFPs. A crucial non-
888 canonical component of this complex is the transcriptional activator ATF2, which plays a
889 central role in relieving repression in response to stress. Upon lipid peroxide accumulation,
890 ATF2, KAP1 and ZNF354A undergo p38- and JNK-dependent phosphorylation. This triple
891 phosphorylation requirement is intriguing and suggests that LORD is a finely tuned, tightly
892 regulated stress-response pathway—warranting further investigation.

893 Phosphorylation causes ZNF354A to dissociate from the complex and to be released from
894 chromatin, enabling the expression of antioxidant genes. These genes protect from ferroptosis
895 and possibly other forms of cell death. Notably, not all antioxidant genes fall under LORD
896 transcriptional control. *GPX4* does not. Instead, its activity is modulated by S-acylation through
897 ZDHHC20L and by ZNF354A-dependent control of GSH availability, both downstream of
898 LORD. Thus, although GPX4 gene expression lies outside the LORD network, its enzymatic
899 function is shaped by it. Future studies should, in particular, determine whether selenoprotein
900 synthesis of GPX4 is also under LORD control.
901 Our findings reinforce the emerging view that KZFPs orchestrate gene regulatory networks
902 across diverse biological processes[35,36,59,92–96]. They also highlight the function of additional
903 factors, such as ATF2, that can dynamically modulate KAP1–KZFP repression complexes in a
904 pathway-specific manner. How ATF2 is selectively recruited to specific KZFP–KAP1
905 complexes remains an open and important question.
906 The expression of ZNF354A-repressed genes involves transcriptional activators. For
907 ZDHHC20L, we identified FOXA1, SP1, and NRF2, the latter being a well-established redox
908 regulator. These findings suggest that LORD operates within a broader transcriptional
909 framework. Future work will define the full set of transcription factors involved in the LORD
910 response, detail the dynamics of activation, and test whether repression serves to delay
911 transcriptional responses—allowing coordinated defense to return to homeostasis[2,14].
912 The discovery of the LORD pathway addresses a long-standing gap in lipid oxidative stress
913 biology and raises exciting new questions, foremost among them how excessive lipid
914 peroxidation is sensed and how this triggers MAP kinase activation. Our findings also highlight
915 testable therapeutic opportunities, such as increasing ferroptosis sensitivity to eliminate cancer
916 cells or activate the LORD pathway to reduce neurodegeneration and inflammation.

Acknowledgments

We warmly thank Dr. Martina Begnis, Dr. Julien Duc, Dr. Priscilla Turelli and Prof. Giovanni D'Angelo for helpful discussions throughout the study and comments on the manuscript. This work is supported by a generous foundation represented by CARIGEST SA, and Swiss National Science Foundation grant 310030_192608 to F.G. v.d.G. and grants from the European Research Council (KRABnKAP, No. 268721; Transpos-X, No. 694658), the Swiss National Science Foundation (310030_152879 and 310030B_173337), and the Aclon Foundation to D.T.

Author contributions

Conceptualization, F.S.M., L.A., R.F., D.T., and F.G.v.d.G.; investigation, F.S.M., L.A., R.F., B.K., C.R., L.B., F.M., D.M., E.P., and O.R.; funding acquisition, F.G.v.d.G.; writing – original draft, F.S.M., L.A., R.F., D.T., and F.G.v.d.G.; writing – review & editing, F.S.M., L.A., R.F., L.B., F.M., D.M., O.R., D.T., and F.G.v.d.G.; resources, B.K. and C.R.

Declaration of Interest

The authors declare that a patent application (EP25160082.1) related to the medical use of the findings reported in this study has been submitted.

Declaration of generative AI and AI-assisted technologies in the writing process

During the preparation of this work, the author(s) used ChatGPT in order to improve the language.

939 **References**

940 1. Lennicke, C. & Cochemé, H. M. Redox metabolism: ROS as specific molecular
941 regulators of cell signaling and function. *Molecular Cell* **81**, 3691–3707 (2021).
942 2. Sies, H. & Jones, D. P. Reactive oxygen species (ROS) as pleiotropic physiological
943 signalling agents. *Nat Rev Mol Cell Biol* **21**, 363–383 (2020).
944 3. Sies, H., Mailloux, R. J. & Jakob, U. Fundamentals of redox regulation in biology. *Nat*
945 *Rev Mol Cell Biol* **25**, 701–719 (2024).
946 4. Dixon, S. J. *et al.* Ferroptosis: An Iron-Dependent Form of Nonapoptotic Cell Death. *Cell*
947 **149**, 1060–1072 (2012).
948 5. Qiu, B. *et al.* Phospholipids with two polyunsaturated fatty acyl tails promote ferroptosis.
949 *Cell* **187**, 1177-1190.e18 (2024).
950 6. Yang, W. S. *et al.* Peroxidation of polyunsaturated fatty acids by lipoxygenases drives
951 ferroptosis. *Proceedings of the National Academy of Sciences* **113**, E4966–E4975 (2016).
952 7. Dixon, S. J. & Olzmann, J. A. The cell biology of ferroptosis. *Nat Rev Mol Cell Biol* **25**,
953 424–442 (2024).
954 8. Maher, P., Currais, A. & Schubert, D. Using the Oxytosis/Ferroptosis Pathway to
955 Understand and Treat Age-Associated Neurodegenerative Diseases. *Cell Chem Biol* **27**,
956 1456–1471 (2020).
957 9. Stockwell, B. R. *et al.* Ferroptosis: A Regulated Cell Death Nexus Linking Metabolism,
958 Redox Biology, and Disease. *Cell* **171**, 273–285 (2017).
959 10. Jiang, X., Stockwell, B. R. & Conrad, M. Ferroptosis: mechanisms, biology and role in
960 disease. *Nat Rev Mol Cell Biol* **22**, 266–282 (2021).
961 11. Stockwell, B. R. Ferroptosis turns 10: Emerging mechanisms, physiological functions,
962 and therapeutic applications. *Cell* **185**, 2401–2421 (2022).
963 12. Conrad, M. & Proneth, B. Selenium: Tracing Another Essential Element of Ferroptotic
964 Cell Death. *Cell Chemical Biology* **27**, 409–419 (2020).
965 13. Ingold, I. *et al.* Selenium Utilization by GPX4 Is Required to Prevent Hydroperoxide-
966 Induced Ferroptosis. *Cell* **172**, 409-422.e21 (2018).
967 14. Jose, E. *et al.* Temporal coordination of the transcription factor response to H2O2 stress.
968 *Nat Commun* **15**, 3440 (2024).
969 15. Anandhan, A., Dodson, M., Schmidlin, C. J., Liu, P. & Zhang, D. D. Breakdown of an
970 Ironclad Defense System: The Critical Role of NRF2 in Mediating Ferroptosis. *Cell*
971 *Chem Biol* **27**, 436–447 (2020).
972 16. Itoh, K. *et al.* An Nrf2/small Maf heterodimer mediates the induction of phase II
973 detoxifying enzyme genes through antioxidant response elements. *Biochem Biophys Res*
974 *Commun* **236**, 313–322 (1997).

975 17. Kerins, M. J. & Ooi, A. The Roles of NRF2 in Modulating Cellular Iron Homeostasis.
976 *Antioxid Redox Signal* **29**, 1756–1773 (2018).
977 18. Raghunath, A. *et al.* Antioxidant response elements: Discovery, classes, regulation and
978 potential applications. *Redox Biol* **17**, 297–314 (2018).
979 19. Baird, L. & Yamamoto, M. The Molecular Mechanisms Regulating the KEAP1-NRF2
980 Pathway. *Mol Cell Biol* **40**, e00099-20 (2020).
981 20. Koppula, P. *et al.* A targetable CoQ-FSP1 axis drives ferroptosis- and radiation-
982 resistance in KEAP1 inactive lung cancers. *Nat Commun* **13**, 2206 (2022).
983 21. Bersuker, K. *et al.* The CoQ oxidoreductase FSP1 acts parallel to GPX4 to inhibit
984 ferroptosis. *Nature* **575**, 688–692 (2019).
985 22. Doll, S. *et al.* FSP1 is a glutathione-independent ferroptosis suppressor. *Nature* **575**, 693–
986 698 (2019).
987 23. Habib, E., Linher-Melville, K., Lin, H.-X. & Singh, G. Expression of xCT and activity of
988 system xc(-) are regulated by NRF2 in human breast cancer cells in response to oxidative
989 stress. *Redox Biol* **5**, 33–42 (2015).
990 24. Sasaki, H. *et al.* Electrophile response element-mediated induction of the
991 cystine/glutamate exchange transporter gene expression. *J Biol Chem* **277**, 44765–44771
992 (2002).
993 25. Yang, W. S. *et al.* Regulation of ferroptotic cancer cell death by GPX4. *Cell* **156**, 317–
994 331 (2014).
995 26. Forcina, G. C. *et al.* Ferroptosis regulation by the NGLY1/NFE2L1 pathway. *Proc Natl*
996 *Acad Sci U S A* **119**, e2118646119 (2022).
997 27. Chen, D. *et al.* ATF4 promotes angiogenesis and neuronal cell death and confers
998 ferroptosis in a xCT-dependent manner. *Oncogene* **36**, 5593–5608 (2017).
999 28. Yang, W.-H., Ding, C.-K. C., Sun, T. A., Hsu, D. S. & Chi, J.-T. The Hippo Pathway
1000 Effector TAZ Regulates Ferroptosis in Renal Cell Carcinoma. *Cell Rep* **28**, 2501-2508.e4
1001 (2019).
1002 29. A, T. *et al.* p53 Suppresses Metabolic Stress-Induced Ferroptosis in Cancer Cells. *Cell*
1003 *reports* **22**, (2018).
1004 30. Yao, F. *et al.* A targetable LIFR−NF-κB−LCN2 axis controls liver tumorigenesis and
1005 vulnerability to ferroptosis. *Nat Commun* **12**, 7333 (2021).
1006 31. Gao, R. *et al.* YAP/TAZ and ATF4 drive resistance to Sorafenib in hepatocellular
1007 carcinoma by preventing ferroptosis. *EMBO Molecular Medicine* **13**, e14351 (2021).
1008 32. Wang, Y. *et al.* Epigenetic regulation of ferroptosis by H2B monoubiquitination and p53.
1009 *EMBO reports* **20**, e47563 (2019).

1010 33. Palma, F. R. *et al.* Histone H3.1 is a chromatin-embedded redox sensor triggered by
1011 tumor cells developing adaptive phenotypic plasticity and multidrug resistance. *Cell*
1012 *Reports* **43**, (2024).
1013 34. Gantner, B. N. *et al.* Histone oxidation as a new mechanism of metabolic control over
1014 gene expression. *Trends in Genetics* **40**, 739–746 (2024).
1015 35. Imbeault, M., Helleboid, P.-Y. & Trono, D. KRAB zinc-finger proteins contribute to the
1016 evolution of gene regulatory networks. *Nature* **543**, 550–554 (2017).
1017 36. Rosspopoff, O. & Trono, D. Take a walk on the KRAB side. *Trends in Genetics* **39**, 844–
1018 857 (2023).
1019 37. S. Mesquita, F. *et al.* SARS-CoV-2 hijacks a cell damage response, which induces
1020 transcription of a more efficient Spike S-acyltransferase. *Nat Commun* **14**, 7302 (2023).
1021 38. Mesquita, F. S. *et al.* S-acylation controls SARS-CoV-2 membrane lipid organization and
1022 enhances infectivity. *Developmental Cell* **56**, 2790-2807.e8 (2021).
1023 39. López-Otín, C., Blasco, M. A., Partridge, L., Serrano, M. & Kroemer, G. Hallmarks of
1024 aging: An expanding universe. *Cell* **186**, 243–278 (2023).
1025 40. ENCODE Project Consortium. An integrated encyclopedia of DNA elements in the
1026 human genome. *Nature* **489**, 57–74 (2012).
1027 41. Luo, Y. *et al.* New developments on the Encyclopedia of DNA Elements (ENCODE)
1028 data portal. *Nucleic Acids Res* **48**, D882–D889 (2020).
1029 42. Haeussler, M. *et al.* The UCSC Genome Browser database: 2019 update. *Nucleic Acids*
1030 *Research* **47**, D853–D858 (2019).
1031 43. van Dam, H. *et al.* ATF-2 is preferentially activated by stress-activated protein kinases to
1032 mediate c-jun induction in response to genotoxic agents. *EMBO J* **14**, 1798–1811 (1995).
1033 44. Bhoumik, A. *et al.* ATM-Dependent Phosphorylation of ATF2 Is Required for the DNA
1034 Damage Response. *Molecular Cell* **18**, 577–587 (2005).
1035 45. Gupta, S., Campbell, D., Dérijard, B. & Davis, R. J. Transcription Factor ATF2
1036 Regulation by the JNK Signal Transduction Pathway. *Science* **267**, 389–393 (1995).
1037 46. Kirsch, K. *et al.* Co-regulation of the transcription controlling ATF2 phosphoswitch by
1038 JNK and p38. *Nat Commun* **11**, 5769 (2020).
1039 47. Yamasaki, T., Takahashi, A., Pan, J., Yamaguchi, N. & Yokoyama, K. K.
1040 Phosphorylation of Activation Transcription Factor-2 at Serine 121 by Protein Kinase C
1041 Controls c-Jun-mediated Activation of Transcription. *J Biol Chem* **284**, 8567–8581
1042 (2009).
1043 48. Sakurai, A., Maekawa, T., Sudo, T., Ishii, S. & Kishimoto, A. Phosphorylation of cAMP
1044 response element-binding protein, CRE-BP1, by cAMP-dependent protein kinase and
1045 protein kinase C. *Biochemical and Biophysical Research Communications* **181**, 629–635
1046 (1991).

1047 49. Lau, E. & Ronai, Z. A. ATF2 – at the crossroad of nuclear and cytosolic functions.
1048 *Journal of Cell Science* **125**, 2815–2824 (2012).
1049 50. Watson, G., Ronai, Z. & Lau, E. ATF2, a paradigm of the multifaceted regulation of
1050 transcription factors in biology and disease. *Pharmacol Res* **119**, 347–357 (2017).
1051 51. Lopez-Bergami, P., Lau, E. & Ronai, Z. Emerging roles of ATF2 and the dynamic AP1
1052 network in cancer. *Nat Rev Cancer* **10**, 65–76 (2010).
1053 52. Bischofberger, M., Iacovache, I. & van der Goot, F. G. Pathogenic pore-forming
1054 proteins: function and host response. *Cell Host Microbe* **12**, 266–275 (2012).
1055 53. Brito, C., Cabanes, D., Sarmento Mesquita, F. & Sousa, S. Mechanisms protecting host
1056 cells against bacterial pore-forming toxins. *Cell. Mol. Life Sci.* **76**, 1319–1339 (2019).
1057 54. Schultz, D. C., Ayyanathan, K., Negorev, D., Maul, G. G. & Rauscher, F. J. SETDB1: a
1058 novel KAP-1-associated histone H3, lysine 9-specific methyltransferase that contributes
1059 to HP1-mediated silencing of euchromatic genes by KRAB zinc-finger proteins. *Genes*
1060 *Dev* **16**, 919–932 (2002).
1061 55. Iyengar, S. & Farnham, P. J. KAP1 Protein: An Enigmatic Master Regulator of the
1062 Genome. *J Biol Chem* **286**, 26267–26276 (2011).
1063 56. Iglesias, N. & Moazed, D. Silencing repetitive DNA. *eLife* **6**, e29503 (2017).
1064 57. O'Geen, H. *et al.* Genome-Wide Analysis of KAP1 Binding Suggests Autoregulation of
1065 KRAB-ZNFs. *PLOS Genetics* **3**, e89 (2007).
1066 58. de Tribolet-Hardy, J. *et al.* Genetic features and genomic targets of human KRAB-zinc
1067 finger proteins. *Genome Res* **33**, 1409–1423 (2023).
1068 59. Helleboid, P.-Y. *et al.* The interactome of KRAB zinc finger proteins reveals the
1069 evolutionary history of their functional diversification. *The EMBO Journal* **38**, (2019).
1070 60. Stoll, G. A., Pandiloski, N., Douse, C. H. & Modis, Y. Structure and functional mapping
1071 of the KRAB-KAP1 repressor complex. *EMBO J* **41**, e111179 (2022).
1072 61. Li, X. *et al.* Role for KAP1 serine 824 phosphorylation and sumoylation/desumoylation
1073 switch in regulating KAP1-mediated transcriptional repression. *J Biol Chem* **282**, 36177–
1074 36189 (2007).
1075 62. Bolderson, E. *et al.* Kruppel-associated Box (KRAB)-associated co-repressor (KAP-1)
1076 Ser-473 phosphorylation regulates heterochromatin protein 1β (HP1-β) mobilization and
1077 DNA repair in heterochromatin. *J Biol Chem* **287**, 28122–28131 (2012).
1078 63. Hu, C. *et al.* Roles of Kruppel-associated Box (KRAB)-associated Co-repressor KAP1
1079 Ser-473 Phosphorylation in DNA Damage Response. *J Biol Chem* **287**, 18937–18952
1080 (2012).
1081 64. Jang, S. M. *et al.* KAP1 facilitates reinstatement of heterochromatin after DNA
1082 replication. *Nucleic Acids Research* **46**, 8788–8802 (2018).

1083 65. White, D. E. *et al.* The ATM substrate KAP1 controls DNA repair in heterochromatin:
1084 Regulation by HP1 proteins and Serine 473/824 phosphorylation. *Mol Cancer Res* **10**,
1085 401–414 (2012).
1086 66. Cheng, C.-T. *et al.* Metabolic Stress-Induced Phosphorylation of KAP1 Ser473 Blocks
1087 Mitochondrial Fusion in Breast Cancer Cells. *Cancer Research* **76**, 5006–5018 (2016).
1088 67. Mertins, P. *et al.* Proteogenomics connects somatic mutations to signalling in breast
1089 cancer. *Nature* **534**, 55–62 (2016).
1090 68. Wu, F. *et al.* Studies of Phosphoproteomic Changes Induced by Nucleophosmin-
1091 Anaplastic Lymphoma Kinase (ALK) Highlight Deregulation of Tumor Necrosis Factor
1092 (TNF)/Fas/TNF-related Apoptosis-induced Ligand Signaling Pathway in ALK-positive
1093 Anaplastic Large Cell Lymphoma. *Mol Cell Proteomics* **9**, 1616–1632 (2010).
1094 69. Krischuns, T. *et al.* Phosphorylation of TRIM28 Enhances the Expression of IFN-β and
1095 Proinflammatory Cytokines During HPAIV Infection of Human Lung Epithelial Cells.
1096 *Front Immunol* **9**, 2229 (2018).
1097 70. Ludwig, S. *et al.* Influenza Virus-induced AP-1-dependent Gene Expression Requires
1098 Activation of the JNK Signaling Pathway *. *Journal of Biological Chemistry* **276**,
1099 10990–10998 (2001).
1100 71. McLean, C. Y. *et al.* GREAT improves functional interpretation of cis-regulatory
1101 regions. *Nat Biotechnol* **28**, 495–501 (2010).
1102 72. Lozano-Sepulveda, S. A. *et al.* S-adenosyl-L-methionine modifies antioxidant-enzymes,
1103 glutathione-biosynthesis and methionine adenosyltransferases-1/2 in hepatitis C virus-
1104 expressing cells. *World J Gastroenterol* **22**, 3746–3757 (2016).
1105 73. Koppula, P., Zhuang, L. & Gan, B. Cystine transporter SLC7A11/xCT in cancer:
1106 ferroptosis, nutrient dependency, and cancer therapy. *Protein Cell* **12**, 599–620 (2021).
1107 74. Mandal, P. K. *et al.* System xc− and Thioredoxin Reductase 1 Cooperatively Rescue
1108 Glutathione Deficiency. *J Biol Chem* **285**, 22244–22253 (2010).
1109 75. Labunskyy, V. M., Hatfield, D. L. & Gladyshev, V. N. Selenoproteins: Molecular
1110 Pathways and Physiological Roles. *Physiol Rev* **94**, 739–777 (2014).
1111 76. Maruyama, A. *et al.* The novel Nrf2-interacting factor KAP1 regulates susceptibility to
1112 oxidative stress by promoting the Nrf2-mediated cytoprotective response. *Biochem J* **436**,
1113 387–397 (2011).
1114 77. Conrad, M., Lorenz, S. M. & Proneth, B. Targeting Ferroptosis: New Hope for As-Yet-
1115 Incurable Diseases. *Trends Mol Med* **27**, 113–122 (2021).
1116 78. Hinrichs, A. S. *et al.* The UCSC Genome Browser Database: update 2006. *Nucleic Acids*
1117 *Res* **34**, D590-598 (2006).
1118 79. Gaschler, M. M. & Stockwell, B. R. Lipid peroxidation in cell death. *Biochemical and*
1119 *biophysical research communications* **482**, 419 (2017).

1120 80. Dixon, S. J. *et al.* Pharmacological inhibition of cystine–glutamate exchange induces
1121 endoplasmic reticulum stress and ferroptosis. *eLife* **3**, e02523 (2014).
1122 81. Zilka, O. *et al.* On the Mechanism of Cytoprotection by Ferrostatin-1 and Liproxstatin-1
1123 and the Role of Lipid Peroxidation in Ferroptotic Cell Death. *ACS Cent. Sci.* **3**, 232–243
1124 (2017).
1125 82. Yamanaka, K. *et al.* A novel fluorescent probe with high sensitivity and selective
1126 detection of lipid hydroperoxides in cells. *RSC Adv.* **2**, 7894–7900 (2012).
1127 83. Li, B. & Pratt, D. A. Methods for determining the efficacy of radical-trapping
1128 antioxidants. *Free Radical Biology and Medicine* **82**, 187–202 (2015).
1129 84. Tycko, J. *et al.* High-Throughput Discovery and Characterization of Human
1130 Transcriptional Effectors. *Cell* **183**, 2020-2035.e16 (2020).
1131 85. Wang, W. *et al.* Novel activity of KRAB domain that functions to reinforce nuclear
1132 localization of KRAB-containing zinc finger proteins by interacting with KAP1. *Cell.*
1133 *Mol. Life Sci.* **70**, 3947–3958 (2013).
1134 86. Huang, B. *et al.* Palmitoylation-dependent regulation of GPX4 suppresses ferroptosis.
1135 *Nat Commun* **16**, 867 (2025).
1136 87. Zhou, L. *et al.* Palmitoylation of GPX4 via the targetable ZDHHC8 determines
1137 ferroptosis sensitivity and antitumor immunity. *Nat Cancer* **6**, 768–785 (2025).
1138 88. Salaun, C., Greaves, J., Tomkinson, N. C. O. & Chamberlain, L. H. The linker domain of
1139 the SNARE protein SNAP25 acts as a flexible molecular spacer that ensures efficient S-
1140 acylation. *J Biol Chem* **295**, 7501–7515 (2020).
1141 89. Witzgall, R., O'Leary, E., Gessner, R., Ouellette, A. J. & Bonventre, J. V. Kid-1, a
1142 putative renal transcription factor: regulation during ontogeny and in response to
1143 ischemia and toxic injury. *Mol Cell Biol* **13**, 1933–1942 (1993).
1144 90. Witzgall, R., Volk, R., Yeung, R. S. & Bonventre, J. V. Genomic structure and
1145 chromosomal location of the rat gene encoding the zinc finger transcription factor Kid-1.
1146 *Genomics* **20**, 203–209 (1994).
1147 91. Shakib, K., Norman, J. T., Fine, L. G., Brown, L. R. & Godovac-Zimmermann, J.
1148 Proteomics profiling of nuclear proteins for kidney fibroblasts suggests hypoxia, meiosis,
1149 and cancer may meet in the nucleus. *PROTEOMICS* **5**, 2819–2838 (2005).
1150 92. Begnis, M. *et al.* Clusters of lineage-specific genes are anchored by ZNF274 in
1151 repressive perinucleolar compartments. *Science Advances* **10**, eado1662 (2024).
1152 93. Martins, F. *et al.* A Cluster of Evolutionarily Recent KRAB Zinc Finger Proteins Protects
1153 Cancer Cells from Replicative Stress–Induced Inflammation. *Cancer Research* **84**, 808–
1154 826 (2024).

1155 94. Pontis, J. *et al.* Hominoid-Specific Transposable Elements and KZFPs Facilitate Human
1156 Embryonic Genome Activation and Control Transcription in Naive Human ESCs. *Cell*
1157 *Stem Cell* **24**, 724-735.e5 (2019).
1158 95. Forey, R. *et al.* Cancer cells subvert the primate-specific KRAB zinc finger protein
1159 ZNF93 to control APOBEC3B. 2025.03.05.641617 Preprint at
1160 https://doi.org/10.1101/2025.03.05.641617 (2025).
1161 96. Pulver, C. *et al.* Evolutionarily recent transcription factors partake in human cell cycle
1162 regulation. *Cell Genomics* 100923 (2025) doi:10.1016/j.xgen.2025.100923.
1163 97. Lakkaraju, A. K. *et al.* Palmitoylated calnexin is a key component of the ribosome-
1164 translocon complex. *Embo J* **31**, 1823–1835 (2012).
1165 98. Quinlan, A. R. & Hall, I. M. BEDTools: a flexible suite of utilities for comparing
1166 genomic features. *Bioinformatics* **26**, 841–842 (2010).
1167

1168 # Methods

1169 **Resource and Data availability**

1170 All resources and materials will be made available upon reasonable request to Gisou van der
1171 Goot (gisou.vandergoot@epfl.ch). All data supporting the findings of this study are available
1172 within the paper, Supplementary Information, Source data and DOI: 10.17632/54dztcj7km.1.
1173 All data regarding the human *ZDHHC20* locus was obtained from the Genome browser on
1174 Human (GRCh37/hg19) (version hg19); Transcript data obtained from GENCODE Genes
1175 track (V4 0lift37) https://genome.ucsc.edu/cgi-bin/hgTrackUi?g=knownGene; Transcription
1176 factor binding sites and Chromatin State segmentation obtained from ENCODE
1177 https://genome.ucsc.edu/cgi-bin/hgTrackUi?db=hg18&g=wgEncodeBroadHmm and
1178 https://genome.ucsc.edu/cgi-
1179 bin/hgTrackUi?hgsid=2468617405_fC2FHA661Zobf2VQ1vQVBSTt1M4b&c=chr5&g=wgE
1180 ncodeReg. Available KZFP ChIP-seq data was obtained from
1181 https://tronoapps.epfl.ch/web/krabopedia/

1182

1183 **Cell lines**

1184 U2OS (ATCC: HTB_96), MDA-MB-231 (ATCC: HTB_26), K-562 (ATCC: CCL_243),
1185 SUDHL4 (ATCC: CRL_2957), SUDHL5 (ATCC: CRL_2958), SUDHL6 (ATCC:
1186 CRL_2959), MCF7 (ATCC: HTB_22), SW480 (ATCC: CCL_228), LS1034 (ATCC:
1187 CRL_2158), HCT116 (ATCC: CRL_3502), HAP-1 (Horizon Discovery: HZGGHC9001),
1188 HAP-1 KO_KAP1 (Horizon Discovery: HZGHC000293c003), HEK293T (ATCC: CRL-
1189 3216), HEPG2 (ATCC: HB_8065), Calu-3 (ATCC: HTB_55), 3T3 (ATCC: CRL_1658),
1190 VERO-E6 (ATCC: CRL_1586) cells were grown in Dulbecco's Modified Eagle Medium
1191 supplemented with 10% FBS, penicillin, and streptomycin. HELA (ATCC: CCL_2) cells were
1192 grown in MEM Media supplemented with 10% fetal calf serum, 1% penicillin–streptomycin,
1193 1% NEAA and 1% glutamine (all media from ThermoFisher Scientific). ZDHHC20 KO

1194 HEK293T cells were generated using CRISPR technology [38]. HEK293T cell lines stably
1195 expressing ZNF354A or GFP were generated as previously described[35].
1196
1197 **Antibodies and Reagents**
1198 The antibodies and reagents were acquired from: ATF2 (Abcam: ab_131484; RRID:
1199 AB_11156678, rabbit: 1:2000x), ATF2 (Abcam: E243 ab32160, RRID: AB_2243137, rabbit:
1200 1:2000x), phosphor-ATF2 (T69) (Abcam : 131106; RRID: AB_11157608;rabbit:1:1000x),
1201 GAPDH (Thermofisher : 398600; RRID: AB_2533438; mouse: 1:4000x), ZDHHC20 (Sigma:
1202 SAB4501054; RRID: AB_10744838; rabbit: 1:2000x), HA-HRP (Roche: 112013819001;
1203 RRID: AB_390917; rat: 1:5000x), KAP1 (Abcam: ab_109289; RRID: AB_10863057, rabbit:
1204 1:1000x), phosphor-KAP1 S473 was generated in D. TRONO laboratory using the following
1205 peptide krsrSgegevsgl (rabbit: 1:500x), Nucleocapside N SARS-CoV-2 (Genetex:
1206 GTX135357; RRID: AB_2868464; rabbit 1:4000x), FLAG (Sigma: F3165; RRID:
1207 AB_259529; mouse: 1:2000x), phosphor-Threonine-Serine (BD: 612548; RRID: AB_399843;
1208 rabbit: 1:1000x), GPX4 for WB (Cell Signalling: 52455; RRID: AB_2924984, rabbit:
1209 1:1000x), GPX4 for IP (MA5-49216, RRID: AB_3074874, mouse 1:2000x), SETDB1 (Novus
1210 Biologicals: NBP1_51677; RRID: AB_11002952, mouse: 1:2000x), NRF2 (Abnova:
1211 H00004780; RRID:566020, mouse: 1:2000x), V5-HRP (Sigma: V2260; RRID: AB_261857,
1212 mouse : 1:2000x), Actin (Millipore: MAB1501; RRID: AB_2223041, mouse: 1:4000x),
1213 MAT1A (Abcam: 129176; RRID: AB_11145300, rabbit: 1:2000x), ZNF354A (Santa Cruz:
1214 81140; RRID: AB_1131557, mouse: 1:1000x), MAT1A (Abcam: ab1129176, RRID:
1215 AB_11145300, rabbit: 1:1000x), Myc (Millipore : 9E10 ,05-419, RRID: AB_309725, mouse:
1216 1:3000x), and HRP-conjugated secondary antibodies (GE-Healthcare).
1217
1218 RSL-3 (Sigma: S8155), Hydrogen Peroxide 30% (Fisher: H/1750/15), Rotenone (Cayman
1219 Chemical: CAY-13995), Ferrostatin-1 (Sigma: SML0583), Bodipy 581/591 C11 (Sigma:
1220 D3861), Liperfluo (Fisher: L248), Propidium Iodide (Thermofisher: P3566), Cell Viability
1221 assay (Promega: G9711), JQ1 (Sigma: SML-1524), Mithramycin (LKT: M3476), Erastin

1222 (Millipore: 329600) , all resuspended in DMSO and N-acetylcysteine (NAC) (Selleckchem:
1223 S1623) resuspended in water, with pH adjusted to 7.4).
1224
1225 **siRNA**
1226 For human ZNF354A, 3 different siRNA in 3'-UTR were tested and validated, from Qiagen:
1227 ZNF354A (TACATCCTTGAGAGAGATGTA), from Santa Cruz (sc-91974), ZNF354A
1228 **(**GTCACGTGATCATCAGAAA), and from Origene , ZNF354A
1229 (GAGGTTTATCCATGGAATTAAATACCT).
1230 siRNAs against all human ZDHHC genes were the same as previously published [97].
1231 The other following human siRNA with the corresponding target sequences were
1232 purchased from Qiagen : ZNF354B (ATCAGTCTTCATTAAGCAACA;
1233 CACATTGAAGAGGACTCCTTA; TACATGCTTGAGTGATTTA), ZNF317
1234 (CATGACGGAAATCACACTAAA), ZNF 308 (CAGTTCATTGGCAACCTCATA),
1235 ZNF677 (GAGATTGGTTACAGTACAAGA), ZNF793
1236 (ACCCTGGCATGTAAACGTTTA), SETDB1 (TCGGGTGGTCGCCAAATACAA), KAP1
1237 (AGCGTCCTGGCACTAACTCAA), ATF2 (CCGAGGTAGTCCACATACAGAA),
1238 NRF2/NFE2L2 (CCCATTGATCTTTCTGATCTA), GPX4
1239 (CGGCTGCGTGGTGAAGCGCTA). The following human siRNA were purchased from
1240 Santa Cruz: SP1 (sc-44221), FOXA1 (sc-37930). Mouse siRNA were purchased from Qiagen
1241 for mouse ZFP354A (TACCACTTTAATAACATTCAA). As a control siRNA, a sequence
1242 targeting the viral glycoprotein VSV-G (5'-ATTGAACAAACGAAACAAGGA-3') was
1243 used. Transfections of 50 nM of siRNA were carried out using *TRANS*IT-X2 (MIRUS), and
1244 the cells were analyzed at least 72 h after transfection.
1245
1246 **Western Blotting**
1247 Cells were washed three times in 1x PBS at 4°C and lysed in Buffer (1x PBS, 0.5% NP40 and
1248 protease inhibitor cocktail; Roche) for 30 min on ice. Lysates were then spin down at 10 000 g,

1249 and the protein content of supernatant were determined, the samples were boiled in Laemmli
1250 buffer for 5 min before separation via SDS-PAGE and western blotting against the different
1251 anti-bodies used in this study. For the analysis of phosphorylated proteins, SuperSep™ Phos-
1252 tag™ gels (cat. no. 199-18011) were used. Western blots were developed using the ECL
1253 protocol and imaged on a Fusion Solo from Vilber Lourmat. Densitometric analysis was
1254 performed using the software Bio-1D from the manufacturer.
1255
1256 **Plasmids**
1257 Plasmids expressing HA-tagged ZNF354A-HA, ZNF317-HA, ZNF677-HA, ZNF793-HA,
1258 KAP1-HA were obtained from the D. Trono lab [35]. Plasmids expressing FLAG-ATF2
1259 (RC2118983) were from Origene, myc-SETDB1 (RC2266620) and plasmids expressing SP1-
1260 FLAG (25543) and FOXA1-V5 (153109) from Addgene. Mutations to change KAP1-HA to
1261 KAP1-FLAG, ZNF354A-HA to ZNF354A-FLAG, FLAG-ATF2 to HA-ATF2, HA-ATF2 6A
1262 (T52A-T69A-T71A-T73A-S490A-S498A), HA-ATF2 6D (T52D-T69D-T71D-T73D-S490D-
1263 S498D), ZNF354A-HA (S169A), ZNF354A-HA (S169D), ZNF354A-HA (T189A), ZNF354A
1264 (T154A), ZNF354A-HA RR (D18R-E27R), ZNF354A RA (E45R-N46A), ZNF354A RR-RA
1265 (D18R-E27R- E45R-N46A), KAP1-HA (S473A), KAP1-HA (S473D) and MYC-SETDB1
1266 inactive form (H1224A-C1226A-C1279A-C1280A-C1281A) were generated following
1267 Quickchange mutagenesis kit (Agilent) instructions. We generated a pIRES-based expression
1268 construct encoding the wild-type cytoplasmic isoform 2 of human GPX4, tagged with Myc and
1269 Flag epitopes. This construct includes a UGA codon at position 46, corresponding to the
1270 incorporation site of selenocysteine (Sec, U46), as well as the selenocysteine insertion sequence
1271 (SECIS) element in the 3′ untranslated region (3′UTR). The SECIS element is a conserved
1272 RNA stem-loop structure required for the recoding of the UGA stop codon as selenocysteine
1273 during translation, enabling the proper synthesis of selenoproteins.
1274
1275 **Q-RT-PCR**

1276 For the real-time PCR, RNA was extracted from a six-well dish using the RNeasy kit (Qiagen).
1277 In all, 0.5-1 mg of the total RNA extracted was used for the reverse transcription using random
1278 hexamers and superscript II (Invitrogen). A 1:40 dilution of the cDNA was used to perform the
1279 real-time PCR using using Applied Biosystems SYBR Green Master Mix on 7900 HT Fast
1280 QPCR System (Applied Biosystems) with SDS 2.4 Software. All data (always in triplicate)
1281 were normalized to Ct values from three housekeeping (HK) genes ALAS-1, Guss and TBP.
1282 Results were expressed as 2^(-ΔΔCt)*100%.
1283

1284 **Oligonucleotides for Quantitative RT-PCR**

1285 All QPCR primers, used in this study are described in detail in table below (Supplementary
1286 Table 1).

Primers	**Forward**	**Reverse**
ALAS-1	CTCACCACACACCCCAGATG	AGTTCCAGCCCCACTTGCT
ATF2	AGTCTGATTGGCTTAACTCGTATT	CACAGGTCCTTGTATTGCCTG
FSP1	ACAGAATATCCTGAGAAAGAGGTCA	ATCTCCTTCACTTCCTGC
GLRX	AACAGAGTGGGGAACTGCTG	AACATTTCCTATGAGATCTGTGGTT
GPX4	GCATCCTGGGAAATGCCATC	GGAGAGACGGTGTCCAAACT
GUSS	CCACCAGGGACCATCCAAT	AGTCAAAATATGTGTTCTGGACAAAGTAA
MAT1A	GGGACACCCGGATAAGATC	CACCACACAGCAGCACCATG
SELB	CCTTGTGATCGGCCAGATTG	TGTTCTCTAGGGTCTTCTGCATT
SELS	CTTTGCGGGGAGGAGGTTA	AGGGTTCATCTTGCTAATGTCAA
SEPHS2	CCTGTCACTGGTGCAGACCAC	CCCATGGCGTAGAGGTCACTC
SEPP1	CTGTGGCTTTGTGGAGCTG	ACATTGCTGGGGTTGTCCTAT
SEPSECS	GCTGTCATGAACCGCGAG	GGACACTTGCCCTTCTCCA
SLC7A11	TGCATATGCTGGCTGGTTTT	GGCCACATTTGTCAGCACAT
SLC3A2	AGCTACGGGGATGAGATTGG	TCTTCACTCTGGCCCTTCAC
TBP	GCCCGAAACGCCGAATATA	CGTGGCTCTCTTATCCTCATGA
TXNRD3	TTCATGTGCGAAGGAAGCT	GGTGACGGGACAACAAAGTC
TXRND1	AAAGGCAAGAACGGCGATG	CAGGGTGATGATCTTTAGCTGAC
ZDHHC20 1	GTGGCCTTATTTGGAAGTGGG	CCCTACTCTAGTATGGCCTC
ZDHHC20 2	GCCACTGCCACTGCAGGTC	CACAGCCATGTGCCCTCTG
ZDHHC20 3	GGCACAAAATCAGGGAGAACAG	AAGAAGACGTCACCCTTTGCT
ZDHHC20 4	AGTCTCCCTCCCCTATTGAGT	AAAACACGCCCTTGATGGAT
ZDHHC20 5	CCTCGGACTTTTGCTCCCACAAG	CGTCCCACCGTTCTGGGGAG
ZDHHC20 C1	CGCCTTGTGGGGATGGATCC	CCGCTTGTTGGACAGTGAATCTCAG

ZDHHC20 C2	GTCGTCTGGTCCTACTACGC	AGCCACAAGGTAAACAACGG
ZNF354A	CGAGGCCCCAGGTGTC	TAAATGGGAGCCCCAGTGAG
ZNF354B	CCCCAGGTGTCACTGACATTC	GAGAGTCCCAGTGAGACCAGG
NRF2	AACTACTCCCAGGTTGCCC	TACAAACGGGAATGTCTGCG
SETDB1	GGCACATGGTGGAAGTCCCGAG	GCTGAACATGGGCTCCAGCCG
KAP1_TRIM28	AAGGACACTGTGCGCTCTAC	ACGTTGCAATAGACAGTACGTTCAC

Supplementary Table 1 - Primers against human genes used in this study.

Aerolysin purification and cell intoxication

Proaerolysin toxin was produced and purified by our laboratory in Aeromonas salmonicida as previously described (ref). Cells were treated one hour in complete medium with 10 ng/ml of proaerolysin at 37 °C. Cells were washed twice in complete medium and further incubated at 37 °C for indicated times.

GREAT – analysis

ChIP-seq data for ZNF354A-HA binding sites were obtained from KRABopedia [58] and submitted to the Genomic Regions Enrichment of Annotations Tool (GREAT - http://great.stanford.edu/public/html/) [71]. The parameters for gene regulatory domains for each gene were defined as domain that extends in both directions of the TSS until the nearest TSS up to a maximum extension of 300 kb.

Human MucilAir assays

MucilAir-human upper respiratory tissues (Epithelix, Geneve, Switzerland) were maintained according to the manufacturer's protocol. For infection, tissues were washed apically with 200 µl of DPBS, calcium, magnesium (#14040091—Gibco) for 20 min at 37 °C and the basal medium replaced with fresh mucilair medium. Tissues were infected at the MOI of 0.1 PFU (assuming the manufacturer's estimations of 500000 cells per tissue). Tissues were inoculated with 200 µl of SARS-CoV-2 (passage 3) for 3 h (apically) at 33 °C. The apical inoculum was

1310 removed and infected tissues were maintained until harvest. For harvest tissues were lysed
1311 using 300 µl lysis buffer for 30 min and processed for western blot.
1312
1313 **Viral Stock production and titration with plaque-based assays**
1314 All viral stocks were produced and isolated from supernatants of Vero E6 cells, cultured in T75
1315 culture flasks to a confluency of 80-90%, and infected with an original passage 2 (P2) SARS-
1316 CoV-2 virus, for 48 or 72 h, at MOI≈0.05, in 10 ml DMEM supplemented with 2.5% FCS.
1317 Original stocks were obtained from the following strain: hCoV-
1318 19/Switzerland/GE9586/2020|EPI_ISL_414022|2020-02-27. Passage 3 supernatants were
1319 harvested, clear of cell debris by centrifugation (500 *g* 10 min) and filtration (0.45 µm),
1320 aliquoted and stored at -80 C. Viral titers were quantified by determining the number of
1321 individual plaque forming units after 48 h of infection in confluent Vero E6 cells as described
1322 in [37].
1323
1324 **SARS-CoV-2 infections**
1325 All infections for experimental analysis were done using passage 3 SARS-CoV-2 stocks. Vero
1326 E6 cells or CALU-3 cells seeded to a confluency of 90 to 100%, were, washed twice in warm
1327 serum-free medium and inoculated with the indicated MOI of SARS-CoV-2, diluted in serum
1328 free medium. 1 hour after inoculation cells were washed with complete medium and infection
1329 allowed to proceed for the indicated time points in DMEM supplemented with 2.5% FCS,
1330 penicillin and streptomycin.
1331
1332 **Drug and toxin treatments**
1333 All drug treatments were done for the indicated times in complete culture and/or infection
1334 medium. Equivalent volume of Dimethyl sulfoxide (DMSO), used as a solvent, was added for
1335 control samples. Specifically, culture media was replaced, cells were washed once in warm
1336 culture media and drugs resuspended as indicated were used as: RSL3 (in DMSO - 3 µM,

1337 increasing concentrations 0.6 to 10 μM), Ferrostatin-1 (DMSO - 1 – 15 μM), H_2O_2 (0.5 – 100
1338 μM), Rotenone (1 – 10 μM).
1339
1340 **Data mining analysis**
1341 UCSC genome browser at ZDHHC20 locus was obtained from (Human version hg19). Specific
1342 UCSC genome browser tracks were selected for display in Fig. 1 and 2. Transcript annotation
1343 corresponds to GENCODE Genes track (version V4 0lift37); Histone Modifications by ChIP-
1344 seq from ENCODE/Stanford/Yale/USC/Harvard display ChIP-seq signals for H3K4me1,
1345 H3K4me3, H3K27Ac marks for HepG2 and H3K9me3 for U2OS. Transcription Factor CHIP-
1346 seq Peaks track shows transcription factor SETDB1, and KAP1binding sites for U2OS and
1347 K562 cells based on ChIP-seq experiments from ENCODE. KZFP CHIP-seq data show binding
1348 sites for different KZFP proteins obtained from KRABopedia
1349 (https://tronoapps.epfl.ch/web/krabopedia/) (https://doi.org/10.1101/2023.02.27.530095)
1350
1351 **Chromatin Immunoprecipitation (ChIP) followed by qPCR or sequencing (ChIP-seq).**
1352 K562 cells (30 million) were cross-linked at room temperature for 10 minutes by adding
1353 formaldehyde to a final concentration of 1%, followed by quenching with glycine Tris 200mM.
1354 Cells were washed twice with PBS, pelleted, and stored at -80°C. Pellets were sequentially
1355 lysed in LB1 (50 mM HEPES-KOH pH 7.4, 140 mM NaCl, 1 mM EDTA, 0.5 mM EGTA,
1356 10% glycerol, 0.5% NP-40, 0.25% Triton X-100, protease inhibitors), LB2 (10 mM Tris-HCl
1357 pH 8.0, 200 mM NaCl, 1 mM EDTA, 0.5 mM EGTA, protease inhibitors), and SDS shearing
1358 buffer (10 mM Tris-HCl pH 8.0, 1 mM EDTA, SDS 0.15%, protease inhibitors). Chromatin
1359 was sonicated (Covaris: 5% duty, 200 cycles, 140 PIP, 20 min 25min) to obtain DNA fragments
1360 of 100-300bp. ChIP was performed anti-HA magnetic beads (Pierce: 88837). Chromatin was
1361 adjusted for immunoprecipitation using 1% Triton X-100 and 150mM NaCl then transferred
1362 on beads, followed by overnight incubation at 4°C. Immunoprecipitated complexes were
1363 washed sequentially with Low Salt Wash Buffer (10 mM Tris-HCl pH 8.0, 1 mM EDTA, 150
1364 mM NaCl, 1% Triton X-100, 0.15% SDS, protease inhibitors), High Salt Wash Buffer (10 mM

1365 Tris-HCl pH 8.0, 1 mM EDTA, 500 mM NaCl, Triton X-100, 0.15% SDS, protease inhibitors),
1366 LiCl Buffer (10 mM Tris-HCl pH 8.0, 1 mM EDTA, 0.5 mM EGTA, 250 mM LiCl, 1% NP-
1367 40, 1% NaDOC, protease inhibitors), and TE buffer. DNA was eluted and purified using
1368 QIAGEN columns. Experiments were performed in biological duplicates, Samples were send
1369 for sequencing and ChIP-QPCR experiments were independently repeated 3 or 4 times for each
1370 depicted primer. ChIP and input DNA were analyzed by qPCR using specific primers and
1371 sequencing. Enrichment was calculated as a percentage of input or relative to a control region
1372 using the ΔΔCt method. Primers used for QPCR are listed below:

Gene/Position	**Primer Sequence (5' → 3')**
ZDHHC20_pos1_fw	AAAGAAGGTCAAAGAAGGAGAAA
ZDHHC20_pos1_rv	GGCTTAAGTCTATCATTTGCTCT
ZDHHC20_pos2_fw	CCATTCAGCCACTCTATGTCTT
ZDHHC20_pos2_rv	AATGGCAGGAATAAATCCTTACTTATC
MAT1A_fw	GCTAGGAAGAAACTGCATCAAAC
MAT1A_rv	CTCCTCAATACAGCACACTGAT
TXNRD1_fw	AGTGTAACTGTGGAATCTGTATGT
TXNRD1_rv	GCCTACCTGGTGCATTCTT
SELS_fw	GATTGAAGAACGGGTGGGA
SELS_rv	AATTACTGGTGTGTTCCAGTTTG

1373

1374 **Library preparation and sequencing.**

1375 DNA concentrations were determined using a Qubit fluorometer (Thermo Fisher Scientific)
1376 following the manufacturer's protocol. Chromatin immunoprecipitated DNA was processed
1377 using the NEBNext Ultra II DNA Library Prep Kit (New England Biolabs, Version 7.0_9/22)
1378 according to the manufacturer's instructions (internal experiment code GFX016). Input DNA
1379 amounts varied between 1.5 ng and 5 ng, as specified in the corresponding sample table. Given
1380 the absence of initial DNA profile data, a positive control was included during library
1381 preparation. Library concentrations were measured using Qubit High Sensitivity (HS) DNA
1382 quantification, and fragment size distributions were assessed using a TapeStation TS4200
1383 (Agilent Technologies). All libraries exhibited expected fragment profiles and sufficient yield
1384 for sequencing. Prepared libraries were sequenced on the Element Biosciences Aviti platform
1385 in a paired-end 150 bp (PE150) run (run ID: AVT0149). Sample-specific identifiers and

1386 sequencing metadata are detailed in the supplementary data. Adapter sequences were trimmed
1387 using Cutadapt vX.X with TruSeq adapter sequences:
1388 Read 1:AGATCGGAAGAGCACACGTCTGAACTCCAGTCA;
1389 Read2: AGATCGGAAGAGCGTCGTGTAGGGAAAGAGTGT
1390

1391 **ChIPseq analysis**

1392 To identify and merge significant peaks across multiple conditions, we utilized BEDTools[98]
1393 (v2.30.0). Initially, overlapping peaks from multiple BED files were merged using the bedtools
1394 multiinter function. To ensure a more comprehensive peak detection, an alternative strategy
1395 was applied, merging all available BED files in the directory. Following peak merging, signal
1396 intensity filtering was performed using deepTools (v3.5.1). The computeMatrix function
1397 extracted signal values from bigWig (BW) files over predefined peak regions (Filt_GFP.bed).
1398 A threshold of 15 was applied to exclude peaks with excessively high signal intensities. To
1399 visualize the signal distribution, a heatmap was generated using plotHeatmap, employing the
1400 Oranges_r colormap. Based on the filtered set (sorted_regionsFilt12.bed), another round of
1401 peak merging was conducted to ensure that only the most relevant peaks were retained. This
1402 final merged peak list contained only peaks present in HEK293T and those retained in K562.
1403 To further refine peak selection and exclude aberrant values, we applied an additional filtering
1404 step with a stricter intensity threshold (--maxThreshold 150). A final heatmap was generated to
1405 visualize the refined peak set. A final heatmap was generated to visualize the refined peak set.
1406 Ultimately, the final set of high-confidence peaks used for downstream analysis was stored in
1407 sorted_regions_3.bed, representing the most relevant and biologically meaningful peak regions
1408 across conditions.
1409

1410 **RNAseq**

1411 RNA quality was controlled on the TapeStation 4200 (Agilent), which confirmed their
1412 integrity. Libraries for mRNA-seq were prepared with the Stranded mRNA Ligation method
1413 (Illumina), according to manufacturer's instructions, starting from 800ng RNA. Libraries, all

1414 bearing unique dual indexes, were subsequently loaded at 100 pM on a Novaseq 6000 flow cell
1415 (Illumina) and sequenced according to manufacturer instructions, yielding pairs of 60
1416 nucleotides reads at a depth of about 70 mio reads pairs per sample. Reads were trimmed of
1417 their adapters with bclconvert v00.000.000.3.9.3 (Illumina) and quality-controlled with fastQC
1418 v0.11.9. FastQ Screen v0.14.0 tool was used for screening FASTQ files reads against multiple
1419 reference genomes.
1420
1421 **RNAseq processing and analysis**
1422 Sequencing reads were mapped to the human hg19 genome using hisat2 [D. Kim, B. Langmead,
1423 and S. L. Salzberg, "HISAT: a fast spliced aligner with low memory requirements," *Nature*
1424 *Methods*, vol. 12, no. 4, pp. 357–360, Mar. 2015.] with parameters: hisat2 -k 5 --seed 42 --rna-
1425 strandness RF. Counts on genes were generated using featureCounts [Y. Liao, G. K. Smyth,
1426 and W. Shi, "featureCounts: an efficient general purpose program for assigning sequence reads
1427 to genomic features," *Bioinformatics*, vol. 30, no. 7, pp. 923–930, Apr. 2014.]. Only uniquely
1428 mapped reads were used for counting on genes. Normalization for sequencing depth was done
1429 using the TMM method as implemented in the limma package of Bioconductor [Gentleman et
1430 al., 2004]. Differential gene expression analysis was performed using voom (Law et al., 2014)
1431 as it has been implemented in the limma package of Bioconductor. A gene was considered to
1432 be differentially expressed when the fold change between groups was bigger than 2 and the p-
1433 value was smaller than 0.05. A moderated t-test (as implemented in the limma package of R)
1434 was used to test significance. P-values were corrected for multiple testing using the Benjamini-
1435 Hochberg's method[97]. Gene set enrichment analysis (GSEA) was performed using
1436 the ClusterProfiler package in R. The analysis utilized a ranked list of genes and gene set
1437 collections downloaded from MsigDB. The GSEA was conducted with the following
1438 parameters: the number of permutations was set to 10,000, minimum gene set size was 10,
1439 maximum gene set size was 800.
1440
1441 **Flow cytometry analysis of membrane permeability and lipid peroxidation**

1442 U2OS cells (1 × 10^6 per well, 6-well plate) were transfected with siRNA for 72 h. For
1443 Liperfluo staining (Dojindo), cells were treated with 5 μM RSL-3 for 24 h, washed twice with
1444 EBSS-10 μM HEPES, and incubated in 1 mL EBSS-HEPES with 5 μM Liperfluo for 30 min
1445 at 37 °C. Cells were washed, trypsinized, washed in 1% FBS EBSS-HEPES to remove trypsin,
1446 resuspended in 500 μL EBSS-HEPES, filtered, and stained with propidium iodide (1 μg/mL)
1447 prior to flow cytometry. For C11-BODIPY581/591 (Invitrogen) staining, siRNA-treated cells
1448 were washed twice in HBSS and incubated in 1 mL HBSS with 10 μM probe for 30 min at 37
1449 °C. Excess dye was removed and cells were treated with 5 μM RSL-3 for 4 h in complete
1450 medium. Cells were then processed as above but stained with DAPI (1 μg/mL). Flow cytometry
1451 was performed on an LSRII or LSR Fortessa (BD Biosciences). Oxidized Liperfluo and
1452 BODIPY were detected using 488 nm excitation and 530/30 nm emission; PI and reduced
1453 BODIPY were detected using 561 nm excitation and 610/20 nm emission. At least 10,000 live
1454 events (PI/DAPI-negative) were acquired per sample and data were analyzed using FlowJo.
1455

1456 **CLICK-PEG Assay**

1457 The protocol was adapted from [88]**.** Twenty-four hours after transfection, cells were washed with
1458 serum-free medium containing 1 mg/mL BSA and incubated for various times with either
1459 100 μM unlabeled palmitic acid (control) or 100 μM palmitic acid-azide. After labeling, cells
1460 were washed twice with cold PBS and lysed in 50 mM Tris-HCl (pH 8.0), 0.5% SDS. Lysates
1461 were subjected to a click reaction with 5 kDa mPEG-alkyne (JKA-3177, Sigma), $CuSO_4$,
1462 TBTA, and ascorbic acid for 1 hour at room temperature. The reaction was stopped by boiling
1463 the samples in 4× SDS–BME sample buffer (SB4×).
1464

1465 **Intracellular glutathione measurements**

1466 Intracellular reduced glutathione levels were measured using the QuantiChrom Glutathione
1467 Assay Kit (DIGT-250, BioAssay Systems), following the manufacturer's instructions. Briefly,
1468 1×10^6 cells were collected and processed for the colorimetric detection of reduced glutathione.
1469 The assay is based on the reaction of glutathione with 5,5′-dithiobis-(2-nitrobenzoic acid)

1470 (DTNB), which yields a yellow-colored product. Absorbance was measured at 412 nm, and
1471 values were directly proportional to the glutathione concentration in the sample.
1472
1473 **^{3}H-palmitic acid radiolabeling experiments**
1474 HeLa cells were transfected or not with different constructs, incubated for 2 h in Glasgow
1475 minimal essential medium (IM; buffered with 10 mM HEPES, pH 7.4) with 200 µCi/ml of ^{3}H
1476 palmitic acid (9,10-^{3}H[N]) (American Radiolabeled Chemicals, Inc.). The cells were washed,
1477 and incubated in DMEM complete medium for the indicated time of chase or directly lysed for
1478 immunoprecipitation with the indicated antibodies. After immunoprecipitation, washed beads
1479 were incubated for 5 min at 90°C in reducing sample buffer prior to 4−20% gradient SDS-
1480 PAGE. Gels were incubated 30 min in a fixative solution (25% isopropanol, 65% H2O, 10%
1481 acetic acid), followed by a 30 min incubation with the signal enhancer Amplify NAMP100 (GE
1482 Healthcare). The radiolabeled products were imaged using a Typhoon phosphoimager and
1483 quantified using a Typhoon Imager (ImageQuanTool, GE Healthcare). The images shown for
1484 ^{3}H-palmitate labeling were obtained using fluorography on film.
1485
1486 **DSS-induced mice colitis**
1487 Six wild-type C57BL/6j mice (8-week-old males) were used. Three (n = 3) mice were used as
1488 controls and three mice were given 3% dextran sulfate sodium in the drinking water for 7 days,
1489 then switched to regular drinking water for 3 days. Three Control 8-week male were given
1490 drinking water that did not contain DSS. During the 10-day experiment, mice were weighted
1491 and disease activity index (DAI) was performed daily based on stool consistency, presence of
1492 occult blood and body weight loss. On day 10, mice were euthanized with injection of
1493 pentobarbital and bled via cardiac puncture, and colon and intestines were collected. For animal
1494 experimentation, all procedures were performed according to protocols approved by the
1495 Veterinary Authorities of the Canton Vaud and according to the Swiss Law (license VD 3497,
1496 EPFL).
1497

1498 **Quantification and Statistical Analysis**

1499 All experiments were conducted independently a minimum of three times. Unless indicated
1500 otherwise, each data point corresponds to a separate experiment yielding consistent outcomes.
1501 Statistical evaluations were carried out using Prism software, with graphical representations
1502 and detailed statistical information available in the figure legends. For ANOVA, p-values were
1503 calculated using post hoc tests: Tukey's and Sidak's for multiple comparisons between groups,
1504 and Dunnett's for comparisons against a control condition. RNA-seq and ChIP-seq analyses
1505 were performed using distinct bioinformatics pipelines, as outlined in the Materials and
1506 Methods section, to ensure appropriate data handling and statistical evaluation specific to each
1507 dataset.

1508 # Supplementary information

1509
1510
1511

Ontology	setSize	pvalue
GOBP_CHEMICAL_HOMEOSTASIS	772	0.000120555
GOBP_REGULATION_OF_RESPONSE_TO_EXTERNAL_STIMULUS	713	0.000122549
GOCC_VACUOLE	711	0.000122594
GOBP_RESPONSE_TO_LIPID	669	0.000122956
GOBP_DEFENSE_RESPONSE_TO_OTHER_ORGANISM	704	0.000123062
GOBP_RESPONSE_TO_CYTOKINE	698	0.000123183
GOBP_REGULATION_OF_IMMUNE_RESPONSE	599	0.000125423
GOBP_INFLAMMATORY_RESPONSE	550	0.000127146
GOBP_INNATE_IMMUNE_RESPONSE	550	0.000127146
GOBP_CYTOKINE_PRODUCTION	550	0.000127146
GOBP_PROCESS_UTILIZING_AUTOPHAGIC_MECHANISM	510	0.0001287
GOCC_ENDOSOME_MEMBRANE	479	0.000129433
GOBP_REGULATION_OF_DEFENSE_RESPONSE	464	0.000129836
GOCC_VACUOLAR_MEMBRANE	417	0.000131752
GOBP_RESPONSE_TO_BACTERIUM	422	0.000131961

1512 **Supplementary Table 2. Gene Set Enrichment Analysis-GSEA dot plot of ZNF354A**
1513 **upregulated enriched GO-terms depicted in Fig 3C.**

1514

symbol	genename	FC	*Padj*	dis ZNF354A peaks	TE.Peak	TEsfam. Peak	TEsfam . age
AKR7L	aldo-keto reductase family 7 like (gene/pseudogene)	1.67637	4.10E-02	735	LINE/L1	L1MEc	132
KLF4	KLF transcription factor 4	3.09815	4.46E-09	5889	DNA/TcMar-Tc1	EutTc1-N2	
ATF7	activating transcription factor 7	1.39198	4.25E-10	10209	LINE/L1	L1M4	105
SELENOS	selenoprotein S	1.34950	1.39E-09	11887	LINE/L1	L1MEg	141
SEPHS2	selenophosphate synthetase 2	1.32264	1.34E-09	15362	LINE/L1	L1PA4	15
MAT1A	methionine adenosyltransferase 1A	13.26199	4.49E-10	16326	LINE/L1	L1MC3	103
RAB3IL1	RAB3A interacting protein like 1	5.55800	3.73E-15	17310	SINE/Alu	AluJr	56
GLRX	glutaredoxin	1.96197	2.62E-14	23895	LINE/L1	L1PA3	11
FTH1	ferritin heavy chain 1	3.21032	8.59E-22	29424	SINE/Alu	AluJr	56
MGST1	microsomal glutathione S-transferase 1	2.22804	1.22E-18	33768	LINE/L1	L1PA4	15
HMGCR	3-hydroxy-3-methylglutaryl-CoA reductase	1.86945	1.59E-15	35907	LINE/L1	L1M1	77
TFRC	transferrin receptor	2.15256	7.21E-17	42168	LINE/L1	L1M4	105
GCLM	glutamate-cysteine ligase modifier subunit	2.06617	4.35E-16	51255	LINE/L1	L1PA4	15
NDUFB8	NADH:ubiquinone oxidoreductase subunit B8	1.08169	3.02E-02	59467	LINE/L1	L1MD1	94
NDUFA5	NADH:ubiquinone oxidoreductase subunit A5	1.12969	2.73E-05	67937	LINE/L1	L1M5	145
NDUFAF7	NADH:ubiquinone oxidoreductase complex assembly factor 7	1.23995	4.09E-05	71450	LTR/ERVL	ERVL-E-int	180
TXNRD1	thioredoxin reductase 1	1.64304	6.17E-16	72320	SINE/Alu	AluSg4	26
HSD17B7	hydroxysteroid 17-beta dehydrogenase 7	1.51071	1.27E-07	73974	LINE/L1	L1ME1	124
CYP19A1	cytochrome P450 family 19 subfamily A member 1	18.88029	4.95E-07	82413	LINE/L1	L1HS	2
SLC3A2	solute carrier family 3 member 2	2.24350	5.43E-18	89414	SINE/Alu	AluY	16
AKR1B1P1	aldehyde reductase family 1 member B1 pseudogene 1	3.05182	6.32E-03	97235			
TXNRD2	thioredoxin reductase 2	1.10808	3.77E-03	106689	LINE/L1	L1MC5a	135
ATF7IP	activating transcription factor 7 interacting protein	1.08151	1.33E-02	107118	LINE/L2	L2	189
SLC7A11	solute carrier family 7 member 11	3.58697	5.49E-19	114361	LINE/L1	L1PA5	19
SRXN1	sulfiredoxin 1	2.04742	1.40E-10	132921	LINE/L1	L1ME1	124
CTH	cystathionine gamma-lyase	2.48726	7.59E-12	143346	LINE/L1	L1MD2	109
TSTD1	thiosulfate sulfurtransferase like domain containing 1	4.98308	2.10E-02	144226			
ATF4	activating transcription factor 4	1.32477	2.50E-09	152172	SINE/MIR	MIR	153
GLRX3	glutaredoxin 3	1.44949	7.10E-13	153087	LINE/L1	L1MD1	94
P4HA2	prolyl 4-hydroxylase subunit alpha 2	2.42890	2.22E-16	167708	LINE/L1	L1PA8	32
ATF3	activating transcription factor 3	37.76809	5.52E-19	167734	LINE/L1	L1MEf	136
AKR1B10	aldo-keto reductase family 1 member B10	2.65612	1.95E-09	213640	SINE/MIR	MIR3	173
AKR1C1	aldo-keto reductase family 1 member C1	9.20472	3.01E-11	223325	LINE/L1	L1MB7	92
DHCR7	7-dehydrocholesterol reductase	1.61435	2.87E-12	225373	LINE/L1	L1MD1	94
NDUFA9	NADH:ubiquinone oxidoreductase subunit A9	1.16230	1.17E-03	282927	SINE/Alu	AluSc	24
NDUFB11	NADH:ubiquinone oxidoreductase subunit B11	1.08236	7.13E-03	296985	LINE/L1	L1MB7	92
NDUFS2	NADH:ubiquinone oxidoreductase core subunit S2	1.05238	5.23E-02	302341	LINE/L1	L1PA5	19
FTL	ferritin light chain	2.46023	1.82E-19	304001	LINE/L1	L1M2	89
HSD17B12	hydroxysteroid 17-beta dehydrogenase 12	1.43413	2.18E-12	304606	LINE/L1	L1MEd	149
SELENOF	selenoprotein F	1.35544	3.64E-11	307944	LINE/L1	L1MA2	54
GSTO1	glutathione S-transferase omega 1	1.51388	4.37E-13	310313	LINE/L1	L1M4a2	119
FRRS1	ferric chelate reductase 1	2.95170	3.22E-08	319661	DNA/hAT-Charlie	Charlie22a	
ATF2	activating transcription factor 2	1.06191	3.39E-02	334627	LINE/L1	L1MEc	132
GSTO2	glutathione S-transferase omega 2	2.18080	4.76E-11	343830	LINE/L1	L1M4a2	119

AKR1C2	aldo-keto reductase family 1 member C2	6.20264	7.50E-10	348751	LINE/L1	L1MB7	92
NDUFV2	NADH:ubiquinone oxidoreductase core subunit V2	1.93345	3.52E-05	363516	LINE/L1	L1M4a1	133
AKR1C3	aldo-keto reductase family 1 member C3	3.86735	1.22E-18	366075	LINE/L1	L1MB7	92
BLVRB	biliverdin reductase B	1.97565	7.61E-14	373773	LINE/L1	L1PA5	19
HMGCS1	3-hydroxy-3-methylglutaryl-CoA synthase 1	2.73390	1.27E-17	379367	LINE/L1	L1PA4	15
GCH1	GTP cyclohydrolase 1	1.60685	2.41E-06	386709	LINE/L1	L1MEc	132
SOD2	superoxide dismutase 2	9.69222	7.70E-19	390822	LINE/L1	L1MEc	132
PRDX1	peroxiredoxin 1	1.21564	2.34E-09	398186	LINE/L1	L1MD1	94
TXN	thioredoxin	1.79078	4.45E-17	418789	LINE/L1	L1PA5	19
PRDX4	peroxiredoxin 4	1.30553	3.66E-10	423424	LINE/L1	L1HS	2
HSD17B14	hydroxysteroid 17-beta dehydrogenase 14	2.48244	4.98E-15	432625	LINE/L1	L1M2	89
TXNL4B	thioredoxin like 4B	1.29035	3.12E-06	488236	LINE/L1	L1PA4	15
FOXQ1	forkhead box Q1	13.03230	2.95E-11	497166			
SELENOK	selenoprotein K	1.07427	4.16E-02	506083	LINE/L1	L1HS	2
MGST3	microsomal glutathione S-transferase 3	1.34790	4.89E-10	533779	LINE/L1	L1MA6	80
FDXR	ferredoxin reductase	1.64100	1.14E-12	553258	SINE/Alu	AluY	16
P4HA1	prolyl 4-hydroxylase subunit alpha 1	1.45452	3.20E-11	557975	LINE/L1	L1M1	77
NDUFS3	NADH:ubiquinone oxidoreductase core subunit S3	1.06963	1.78E-02	568919	SINE/Alu	AluYg6	4
NSDHL	NAD(P) dependent steroid dehydrogenase-like	1.45957	2.31E-10	589094	LINE/L1	L1MEf	136
AKR1C7P	aldo-keto reductase family 1 member C7, pseudogene	4.48240	4.75E-03	618961	LINE/L1	L1MB7	92
NDUFB2	NADH:ubiquinone oxidoreductase subunit B2	1.09303	6.19E-03	622344	LINE/L1	L1M4	105
LTF	lactotransferrin	2.54085	2.72E-02	679508	LINE/L1	L1MEd	149
MELTF	melanotransferrin	1.69815	2.85E-07	692986	LINE/L1	L1MA6	80
NDUFA9P1	NADH:ubiquinone oxidoreductase subunit A9 pseudogene 1	7.90338	7.64E-03	708980			
LSS	lanosterol synthase	1.68330	5.04E-15	709144	LINE/L1	L1MD1	94
MSMO1	methylsterol monooxygenase 1	1.88010	3.65E-16	782003	LINE/L1	L1PA4	15
NDUFAF2	NADH:ubiquinone oxidoreductase complex assembly factor 2	1.20448	2.76E-05	816680	LINE/L1	L1ME2z	119
PRDX5	peroxiredoxin 5	1.21422	2.47E-08	842276	LINE/L1	L1M4a2	119
NDUFB4	NADH:ubiquinone oxidoreductase subunit B4	1.10886	4.20E-04	850356	LINE/L1	L1MA3	59
HSD11B1L	hydroxysteroid 11-beta dehydrogenase 1 like	1.76546	2.35E-09	890504	LINE/L1	L1M1	77
SC5D	sterol-C5-desaturase	1.49738	1.51E-12	891316	LINE/L1	L1MEc	132
NDUFAF4	NADH:ubiquinone oxidoreductase complex assembly factor 4	1.33062	1.84E-07	912348	LINE/L1	L1MEf	136
NDUFA4	NDUFA4 mitochondrial complex associated	1.08067	7.47E-03	979671	LINE/L1	L1M1	77
FTH1P2	ferritin heavy chain 1 pseudogene 2	3.43869	1.22E-16	1048840	LINE/L1	L1M4	105
NDUFS4	NADH:ubiquinone oxidoreductase subunit S4	1.14451	4.91E-04	1053523	LINE/L1	L1MDa	112
GPX3	glutathione peroxidase 3	1.52610	3.00E-10	1058124			
SELENOM	selenoprotein M	1.18063	3.74E-04	1099433	LINE/L1	L1M5	145
FTH1P10	ferritin heavy chain 1 pseudogene 10	3.05804	3.51E-13	1111474	LTR/ERV1	MER4-int	59
HSD17B10	hydroxysteroid 17-beta dehydrogenase 10	1.25522	3.49E-08	1135437	LINE/L1	L1ME1	124
FSP1/AIFM 2	Ferroptosis suppressor protein 1	1.72545	5.60E-14	1178833	LINE/L1	L1MEg	141
NDUFB9	NADH:ubiquinone oxidoreductase subunit B9	1.13064	2.85E-05	1232076	LINE/L1	L1MB3	82
NQO1	NAD(P)H quinone dehydrogenase 1	1.17734	3.96E-07	1242909	LINE/L1	L1MDa	112
NMRAL2P	NmrA like redox sensor 2, pseudogene	10.28214	3.79E-16	1305694	LINE/L1	L1MEf	136
NDUFA7	NADH:ubiquinone oxidoreductase subunit A7	2.12137	8.05E-05	1326649	LINE/L1	L1MEg	141
FDFT1	farnesyl-diphosphate farnesyltransferase 1	1.27331	1.73E-09	1356011	LINE/L1	L1ME4b	146
SLC8A2	solute carrier family 8 member A2	67.21656	1.22E-07	1425404	LINE/L1	L1PA10	40

PNLIPRP3	pancreatic lipase related protein 3	421.49194	5.61E-08	1444167			
TXNDC11	thioredoxin domain containing 11	1.15231	2.33E-05	1451931	LINE/L1	L1PA4	15
NDUFAF1	NADH:ubiquinone oxidoreductase complex assembly factor 1	1.07162	4.05E-02	1481054	LINE/L1	L1MEf	136
SELENOW	selenoprotein W	1.12829	1.38E-03	1490730	LINE/L1	L1M2	89
SQLE	squalene epoxidase	1.35487	2.41E-10	1691471	LINE/L1	L1MB3	82
NDUFS7	NADH:ubiquinone oxidoreductase core subunit S7	1.13717	1.91E-04	1744888	LINE/L1	L1MD	120
TXNDC5	thioredoxin domain containing 5	1.10580	2.04E-02	1943399	LINE/L1	L1PA2	7
NDUFA3	NADH:ubiquinone oxidoreductase subunit A3	1.11283	1.68E-03	2022941	SINE/Alu	AluSp	23
GPX4	glutathione peroxidase 4	1.17304	2.59E-06	2024478	LINE/L1	L1MD	120
HSD17B2	hydroxysteroid 17-beta dehydrogenase 2	1.84782	3.64E-06	2575820			
GCLC	glutamate-cysteine ligase catalytic subunit	2.69661	1.32E-16	2600255	LINE/L1	L1ME1	124
HSD11B1	hydroxysteroid 11-beta dehydrogenase 1	12.90050	2.94E-08	2683104			
HSD17B4	hydroxysteroid 17-beta dehydrogenase 4	1.10894	1.70E-04	2753786	LINE/L1	L1PA5	19
PPT1	palmitoyl-protein thioesterase 1	2.00294	4.07E-16	2875962	LINE/L1	L1MD2	109
HSD17B7P2	hydroxysteroid 17-beta dehydrogenase 7 pseudogene 2	1.36815	1.40E-02	3099994	LINE/L1	L1M4c	106
ATP6V0D2	ATPase H+ transporting V0 subunit d2	33.31862	1.93E-10	3771851			
GSR	glutathione-disulfide reductase	1.45407	4.01E-12	3798310	LINE/L1	L1MEc	132
A1BG-AS1	A1BG antisense RNA 1	1.27134	1.33E-04	6276022	SINE/Alu	AluSp	23
TXNL1	thioredoxin like 1	1.16451	9.03E-07	6423295	LINE/L1	L1PA5	19
FECH	ferrochelatase	1.14963	1.53E-05	7358468	LINE/L1	L1PA5	19

1515 **Supplementary Table 3. Selected Antioxidant genes up-regulated upon**
1516 **siZNF354A.** Fold enrichment, adjusted P values, distance to nearest ZNF354A peak,
1517 and corresponding overlapping TE (with Subfam and age) are indicated.

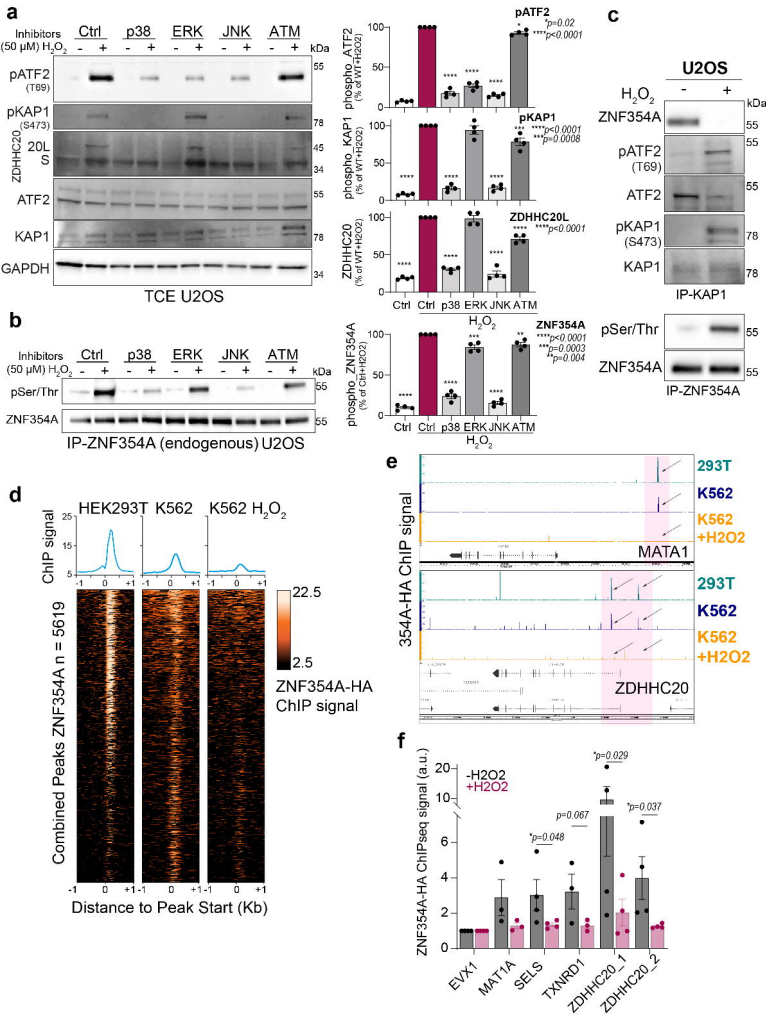
a
Inhibitors (50 μM) H2O2
Ctrl
p38
ERK
JNK
ATM
kDa
pATF2 (T69)
pKAP1 (S473)
ZDHHC20 S
20L
ATF2
KAP1
GAPDH
TCE U2OS
pATF2
*p=0.02
****p<0.0001
pKAP1
****p<0.0001
***p=0.0008
ZDHHC20L
***p<0.0001
phospho_ATF2 (% of WT+H2O2)
phospho_KAP1 (% of WT+H2O2)
ZDHHC20 (% of WT+H2O2)
H2O2
b
pSer/Thr
ZNF354A
IP-ZNF354A (endogenous) U2OS
ZNF354A
***p<0.0001
**p=0.0003
*p=0.004
phospho_ZNF354A (% of Ctrl+H2O2)
c
U2OS
ZNF354A
pATF2 (T69)
ATF2
pKAP1 (S473)
KAP1
IP-KAP1
pSer/Thr
ZNF354A
IP-ZNF354A
d
HEK293T
K562
K562 H2O2
ChIP signal
Combined Peaks ZNF354A n = 5619
22.5
2.5
ZNF354A-HA ChIP signal
Distance to Peak Start (Kb)
e
354A-HA ChIP signal
293T
K562
K562 +H2O2
MATA1
ZDHHC20
f
ZNF354A-HA ChIPseq signal (a.u.)
-H2O2
+H2O2
*p=0.029
p=0.067
*p=0.048
*p=0.037
EVX1
MAT1A
SELS
TXNRD1
ZDHHC20_1
ZDHHC20_2

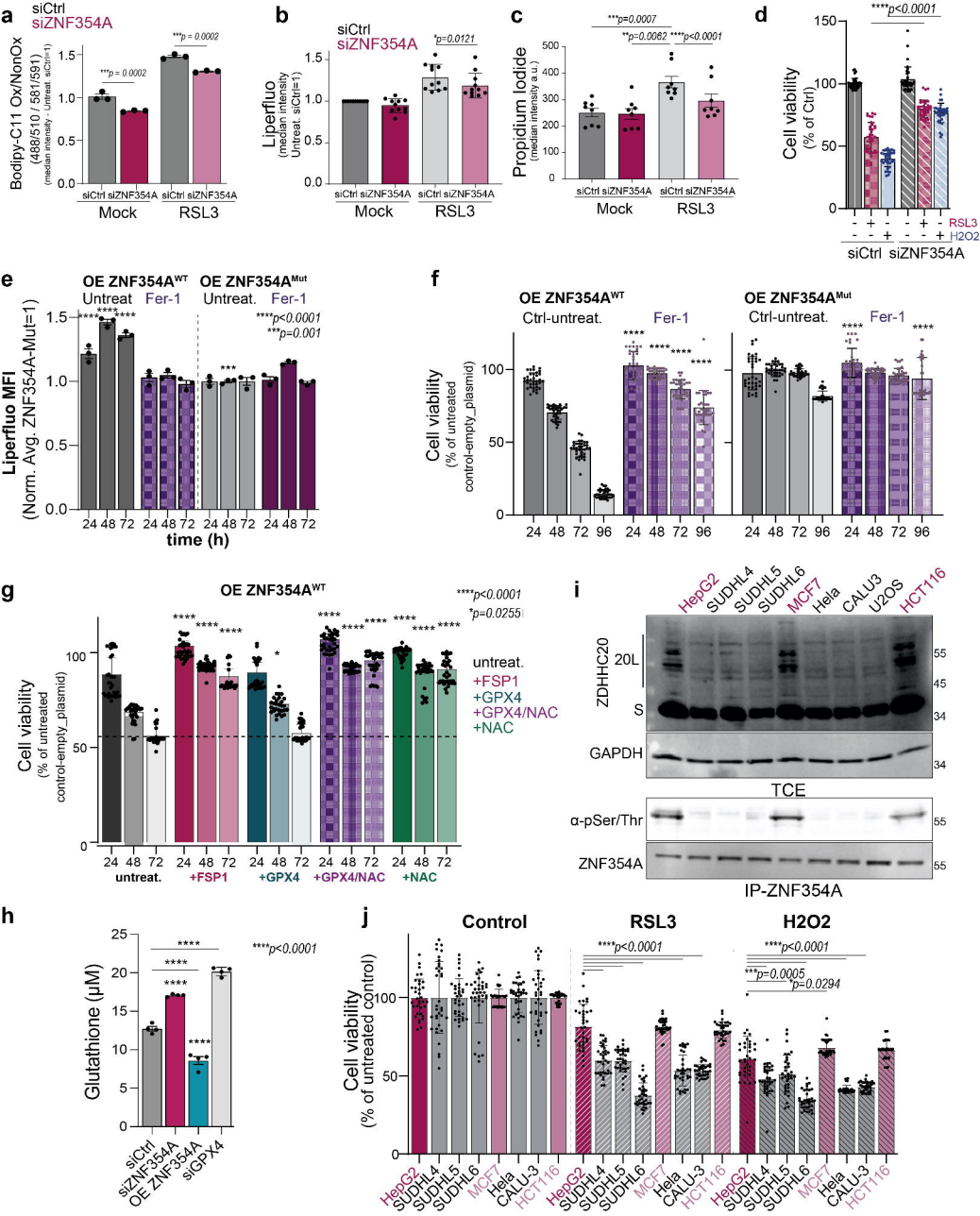
a
siCtrl
siZNF354A
Bodipy-C11 Ox/NonOx
(488/510 / 581/591)
(median intensity - Untreat. siCtrl=1)
***p = 0.0002
***p = 0.0002
siCtrl siZNF354A siCtrl siZNF354A
Mock
RSL3
b
siCtrl
siZNF354A
Liperfluo
(median intensity
Untreat. siCtrl=1)
*p=0.0121
siCtrl siZNF354A siCtrl siZNF354A
Mock
RSL3
c
Propidium Iodide
(median intensity a.u.)
***p=0.0007
**p=0.0062
****p<0.0001
siCtrl siZNF354A siCtrl siZNF354A
Mock
RSL3
d
Cell viability
(% of Ctrl)
****p<0.0001
RSL3
H2O2
siCtrl siZNF354A
e
OE ZNF354A^WT
OE ZNF354A^Mut
Untreat
Fer-1
Untreat.
Fer-1
****p<0.0001
***p=0.001
Liperfluo MFI
(Norm. Avg. ZNF354A-Mut=1)
time (h)
f
OE ZNF354A^WT
OE ZNF354A^Mut
Ctrl-untreat.
Fer-1
Ctrl-untreat.
Fer-1
Cell viability
(% of untreated
control-empty_plasmid)
g
OE ZNF354A^WT
****p<0.0001
*p=0.0255
Cell viability
(% of untreated
control-empty_plasmid)
untreat.
+FSP1
+GPX4
+GPX4/NAC
+NAC
untreat.
+FSP1
+GPX4
+GPX4/NAC
+NAC
i
HepG2
SUDHL4
SUDHL5
SUDHL6
MCF7
Hela
CALU3
U2OS
HCT116
ZDHHC20
20L
S
GAPDH
TCE
α-pSer/Thr
ZNF354A
IP-ZNF354A
h
Glutathione (μM)
****p<0.0001
siCtrl
siZNF354A
OE ZNF354A
siGPX4
j
Control
RSL3
H2O2
Cell viability
(% of untreated control)
****p<0.0001
****p<0.0001
***p=0.0005
*p=0.0294
HepG2
SUDHL4
SUDHL5
SUDHL6
MCF7
Hela
CALU3
HCT116

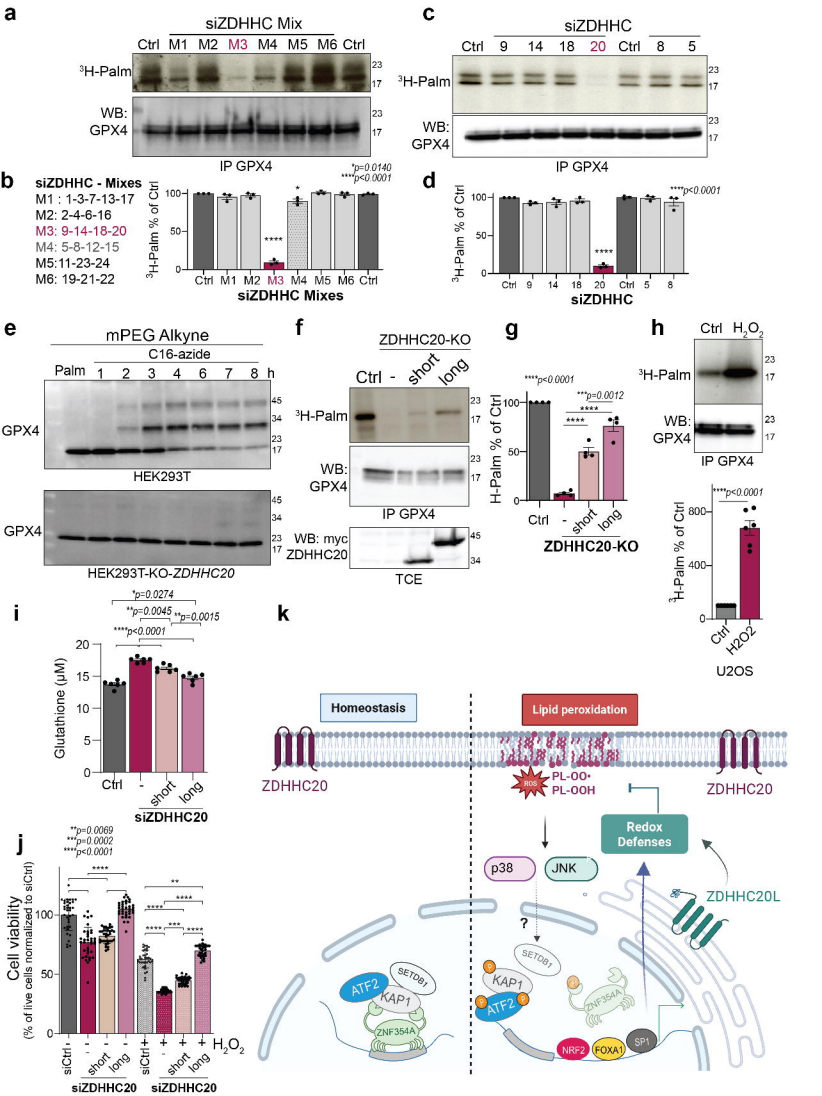
a
siZDHHC Mix
Ctrl M1 M2 M3 M4 M5 M6 Ctrl
3H-Palm
WB: GPX4
IP GPX4
b
siZDHHC - Mixes
M1 : 1-3-7-13-17
M2: 2-4-6-16
M3: 9-14-18-20
M4: 5-8-12-15
M5:11-23-24
M6: 19-21-22
*p=0.0140
****p<0.0001
3H-Palm % of Ctrl
siZDHHC Mixes
c
siZDHHC
Ctrl 9 14 18 20 Ctrl 8 5
d
****p<0.0001
siZDHHC
e
mPEG Alkyne
C16-azide
Palm 1 2 3 4 6 7 8 h
GPX4
HEK293T
HEK293T-KO-ZDHHC20
f
ZDHHC20-KO
Ctrl - short long
WB: myc ZDHHC20
TCE
g
***p=0.0012
ZDHHC20-KO
h
Ctrl H2O2
***p<0.0001
U2OS
i
*p=0.0274
**p=0.0045
**p=0.0015
****p<0.0001
Glutathione (µM)
siZDHHC20
j
**p=0.0069
***p=0.0002
****p<0.0001
Cell viability
(% of live cells normalized to siCtrl)
siCtrl
siZDHHC20
k
Homeostasis
Lipid peroxidation
ZDHHC20
PL-OO•
PL-OOH
Redox Defenses
p38
JNK
ZDHHC20L
ATF2
SETDB1
KAP1
ZNF354A
NRF2
FOXA1
SP1

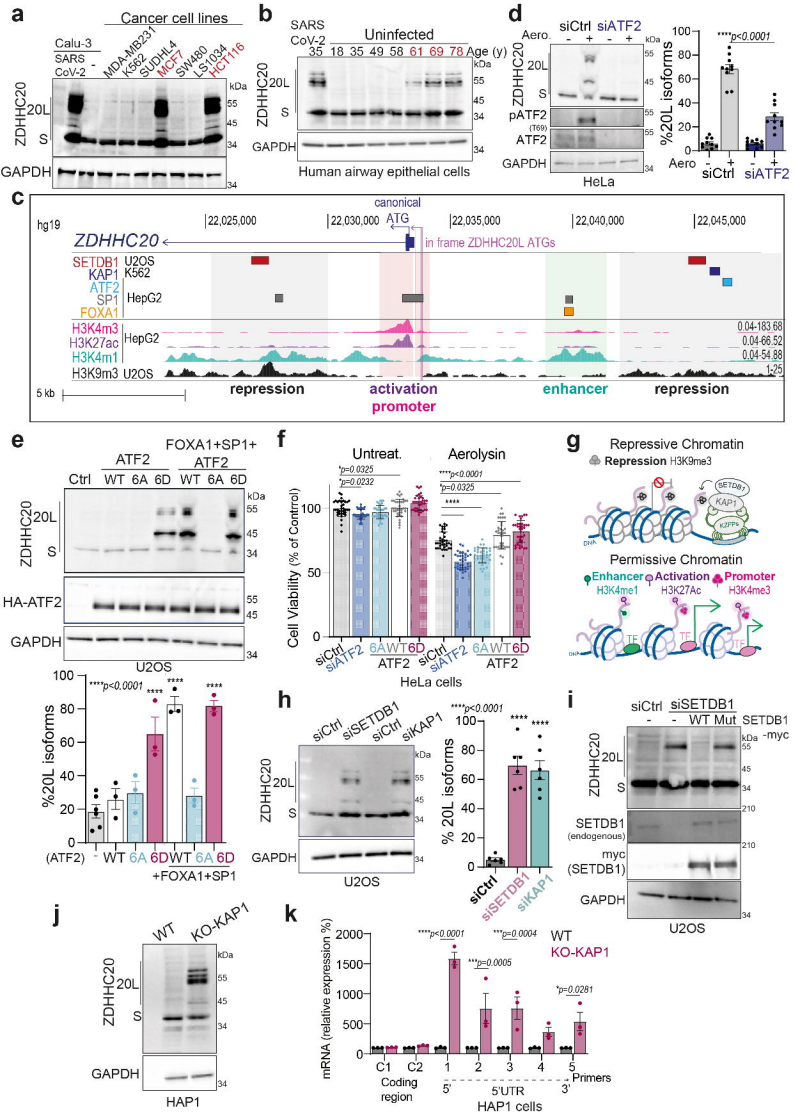
a
Cancer cell lines
Calu-3
SARS CoV-2
-
MDA-MB231
K562
SYDHL4
MCF7
SW480
LS1034
HCT116
ZDHHC20
20L
S
GAPDH
kDa
55
45
34
b
SARS CoV-2
Uninfected
35 18 35 49 58 61 69 78 Age (y)
Human airway epithelial cells
d
Aero.
siCtrl siATF2
pATF2 (T69)
ATF2
HeLa
%20L isoforms
****p<0.0001
c
hg19
22,025,000
22,030,000
22,035,000
22,040,000
22,045,000
canonical ATG
ZDHHC20
in frame ZDHHC20L ATGs
SETDB1 U2OS
KAP1 K562
ATF2
SP1 HepG2
FOXA1
H3K4m3
H3K27ac HepG2
H3K4m1
H3K9m3 U2OS
0.04-183.68
0.04-66.52
0.04-54.88
1-25
5 kb
repression
activation
promoter
enhancer
repression
e
Ctrl
ATF2
FOXA1+SP1+ ATF2
WT 6A 6D WT 6A 6D
HA-ATF2
U2OS
%20L isoforms
(ATF2)
+FOXA1+SP1
f
Untreat.
Aerolysin
Cell Viability (% of Control)
siCtrl siATF2 6A WT 6D siCtrl siATF2 6A WT 6D
ATF2
HeLa cells
g
Repressive Chromatin
Repression H3K9me3
SETDB1
KAP1
KZFPs
DNA
Permissive Chromatin
Enhancer H3K4me1
Activation H3K27Ac
Promoter H3K4me3
TF
h
siCtrl siSETDB1 siCtrl siKAP1
U2OS
% 20L isoforms
siCtrl siSETDB1 siKAP1
i
siCtrl siSETDB1
WT Mut SETDB1 -myc
SETDB1 (endogenous)
myc (SETDB1)
U2OS
j
WT KO-KAP1
HAP1
k
WT
KO-KAP1
mRNA (relative expression %)
C1 C2 1 2 3 4 5 Primers
Coding region
5' 5'UTR 3'
HAP1 cells

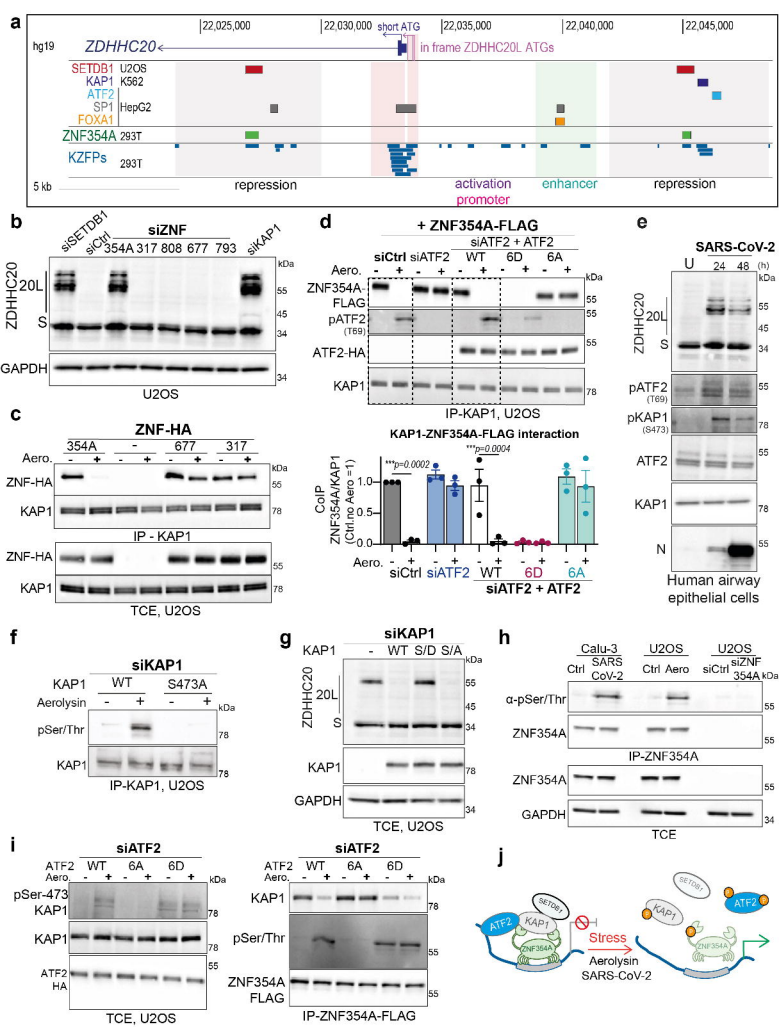
a
hg19
ZDHHC20
short ATG
in frame ZDHHC20L ATGs
22,025,000
22,030,000
22,035,000
22,040,000
22,045,000
SETDB1 U2OS
KAP1 K562
ATF2
SP1 HepG2
FOXA1
ZNF354A 293T
KZFPs 293T
5 kb
repression
activation promoter
enhancer
repression
b
siSETDB1
siCtrl
siZNF
354A 317 808 677 793
siKAP1
kDa
ZDHHC20
20L
S
GAPDH
U2OS
c
ZNF-HA
354A
677
317
Aero.
ZNF-HA
KAP1
IP - KAP1
TCE, U2OS
d
+ ZNF354A-FLAG
siCtrl siATF2
siATF2 + ATF2
WT 6D 6A
ZNF354A-FLAG
pATF2 (T69)
ATF2-HA
KAP1
IP-KAP1, U2OS
KAP1-ZNF354A-FLAG interaction
***p=0.0002
***p=0.0004
CoIP ZNF354A/KAP1 (Ctrl.no Aero.=1)
siCtrl siATF2 WT 6D 6A
siATF2 + ATF2
e
SARS-CoV-2
U 24 48 (h)
ZDHHC20
20L
S
pATF2 (T69)
pKAP1 (S473)
ATF2
KAP1
N
Human airway epithelial cells
f
siKAP1
KAP1 WT S473A
Aerolysin
pSer/Thr
KAP1
IP-KAP1, U2OS
g
siKAP1
KAP1 - WT S/D S/A
ZDHHC20
20L
S
KAP1
GAPDH
TCE, U2OS
h
Calu-3 U2OS U2OS
Ctrl SARS CoV-2 Ctrl Aero siCtrl siZNF 354A
α-pSer/Thr
ZNF354A
IP-ZNF354A
ZNF354A
GAPDH
TCE
i
siATF2
ATF2 WT 6A 6D
Aero.
pSer-473
KAP1
KAP1
ATF2 HA
TCE, U2OS
siATF2
ATF2 WT 6A 6D
Aero.
KAP1
pSer/Thr
ZNF354A FLAG
IP-ZNF354A-FLAG
j
SETDB1
ATF2
KAP1
ZNF354A
Stress
Aerolysin
SARS-CoV-2

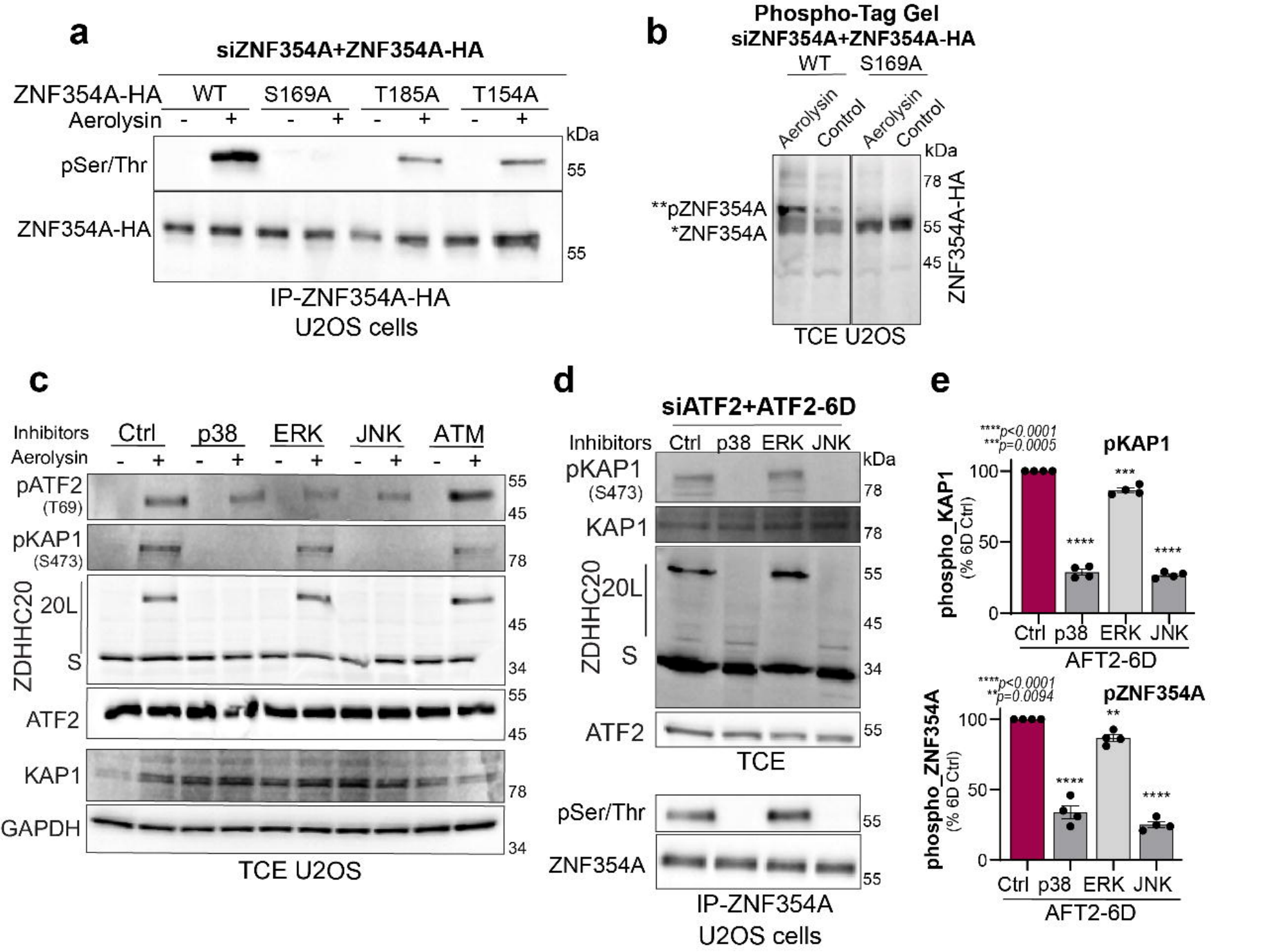
a
siZNF354A+ZNF354A-HA
ZNF354A-HA
WT
S169A
T185A
T154A
Aerolysin
- + - + - + - +
kDa
pSer/Thr
55
ZNF354A-HA
55
IP-ZNF354A-HA
U2OS cells
b
Phospho-Tag Gel
siZNF354A+ZNF354A-HA
WT
S169A
Aerolysin
Control
Aerolysin
Control
kDa
78
**pZNF354A
*ZNF354A
55
45
ZNF354A-HA
TCE U2OS
c
Inhibitors
Ctrl
p38
ERK
JNK
ATM
Aerolysin
- + - + - + - + - +
pATF2
(T69)
55
45
pKAP1
(S473)
78
ZDHHC20
20L
S
45
34
ATF2
55
45
KAP1
78
GAPDH
34
TCE U2OS
d
siATF2+ATF2-6D
Inhibitors
Ctrl
p38
ERK
JNK
kDa
pKAP1
(S473)
78
KAP1
78
ZDHHC20
20L
S
55
45
34
ATF2
55
TCE
pSer/Thr
55
ZNF354A
55
IP-ZNF354A
U2OS cells
e
****p<0.0001
***p=0.0005
pKAP1
phospho_KAP1
(% 6D Ctrl)
100
50
0
***
****
****
Ctrl
p38
ERK
JNK
AFT2-6D
****p<0.0001
**p=0.0094
pZNF354A
phospho_ZNF354A
(% 6D Ctrl)
100
50
0
**
****
****
Ctrl
p38
ERK
JNK
AFT2-6D

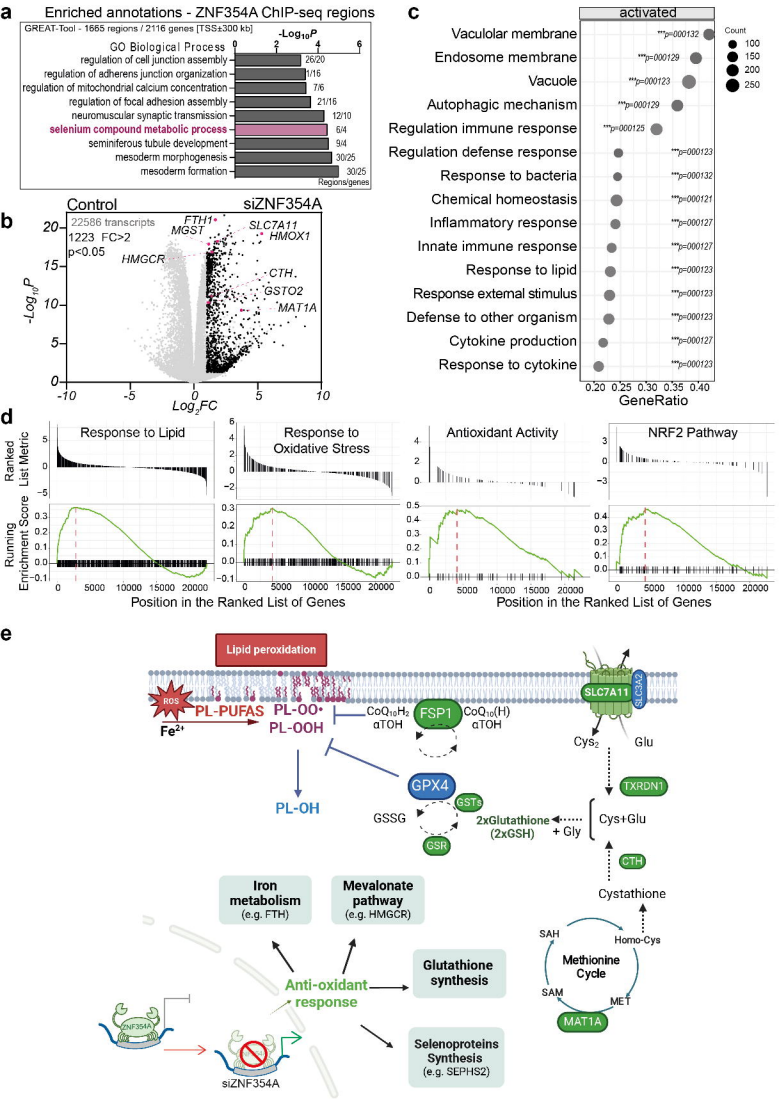
a
Enriched annotations - ZNF354A ChIP-seq regions
GREAT-Tool - 1665 regions / 2116 genes [TSS±300 kb]
GO Biological Process
-Log10P
0 2 4 6
regulation of cell junction assembly 26/20
regulation of adherens junction organization 11/16
regulation of mitochondrial calcium concentration 7/6
regulation of focal adhesion assembly 21/16
neuromuscular synaptic transmission 12/10
selenium compound metabolic process 6/4
seminiferous tubule development 9/4
mesoderm morphogenesis 30/25
mesoderm formation 30/25
Regions/genes
b
Control
siZNF354A
22586 transcripts
1223 FC>2
p<0.05
FTH1
MGST
SLC7A11
HMOX1
HMGCR
CTH
GSTO2
MAT1A
-Log10P
Log2FC
c
activated
Vaculolar membrane ***p=000132
Endosome membrane ***p=000129
Vacuole ***p=000123
Autophagic mechanism ***p=000129
Regulation immune response ***p=000125
Regulation defense response ***p=000123
Response to bacteria ***p=000132
Chemical homeostasis ***p=000121
Inflammatory response ***p=000127
Innate immune response ***p=000127
Response to lipid ***p=000123
Response external stimulus ***p=000123
Defense to other organism ***p=000123
Cytokine production ***p=000127
Response to cytokine ***p=000123
Count
100
150
200
250
0.20 0.25 0.30 0.35 0.40
GeneRatio
d
Response to Lipid
Response to Oxidative Stress
Antioxidant Activity
NRF2 Pathway
Ranked List Metric
Running Enrichment Score
Position in the Ranked List of Genes
Position in the Ranked List of Genes
e
Lipid peroxidation
ROS
PL-PUFAS
PL-OO•
PL-OOH
Fe2+
PL-OH
CoQ10H2
αTOH
FSP1
CoQ10(H)
αTOH
SLC7A11
SLC3A2
Cys2
Glu
GPX4
GSTs
GSSG
GSR
2xGlutathione
(2xGSH)
+ Gly
TXRDN1
Cys+Glu
CTH
Cystathione
Iron metabolism
(e.g. FTH)
Mevalonate pathway
(e.g. HMGCR)
Glutathione synthesis
Anti-oxidant response
Selenoproteins Synthesis
(e.g. SEPHS2)
SAH
Homo-Cys
Methionine Cycle
SAM
MET
MAT1A
ZNF354A
siZNF354A

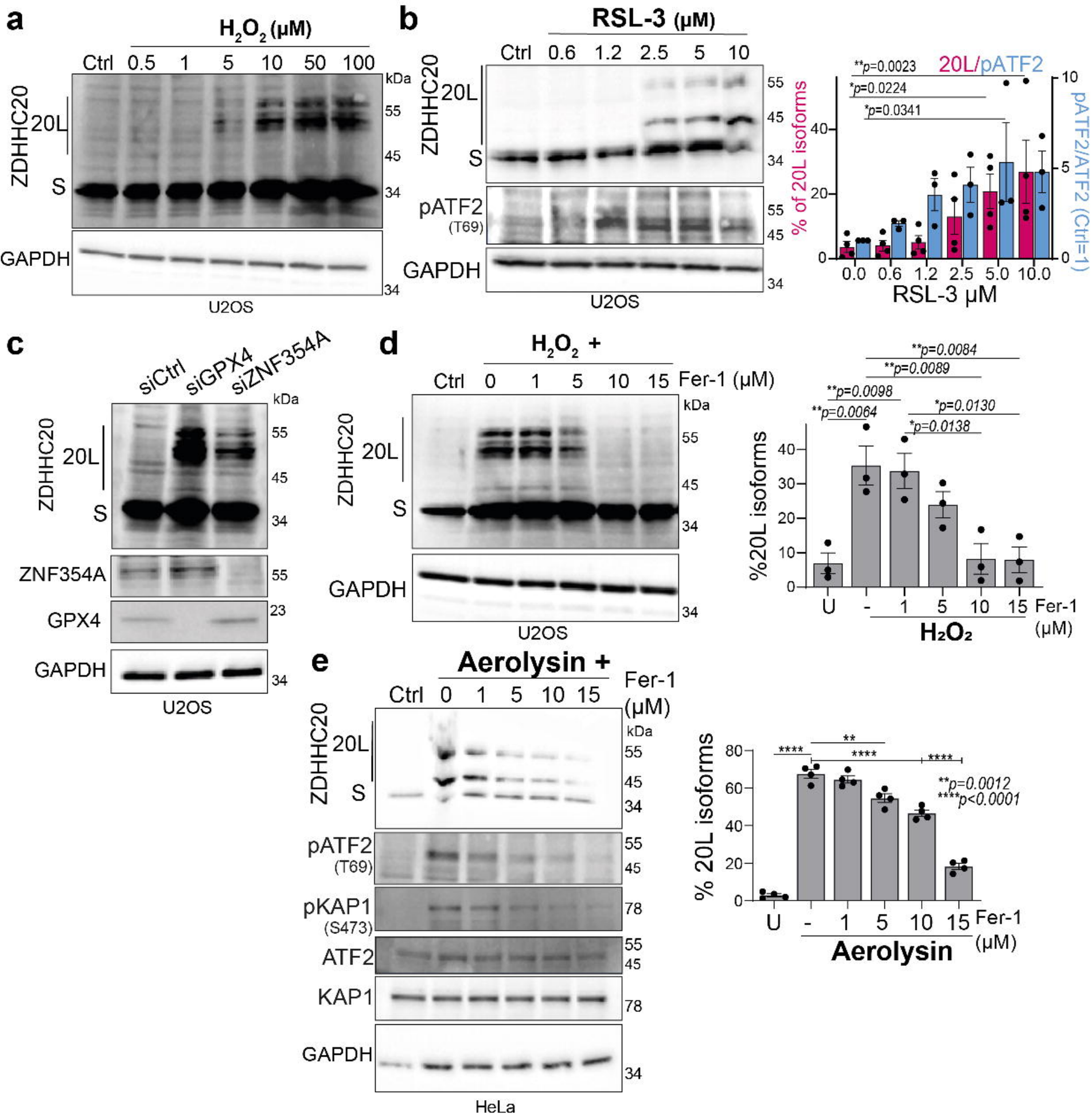
a
H2O2 (μM)
Ctrl 0.5 1 5 10 50 100
ZDHHC20
20L
S
GAPDH
kDa
55
45
34
34
U2OS
b
RSL-3 (μM)
Ctrl 0.6 1.2 2.5 5 10
ZDHHC20
20L
S
pATF2
(T69)
GAPDH
55
45
34
55
45
34
U2OS
20L/pATF2
**p=0.0023
*p=0.0224
*p=0.0341
% of 20L isoforms
pATF2/ATF2 (Ctrl=1)
0.0 0.6 1.2 2.5 5.0 10.0
RSL-3 μM
c
siCtrl siGPX4 siZNF354A
ZDHHC20
20L
S
ZNF354A
GPX4
GAPDH
kDa
55
45
34
55
23
34
U2OS
d
H2O2 +
Ctrl 0 1 5 10 15 Fer-1 (μM)
ZDHHC20
20L
S
GAPDH
kDa
55
45
34
34
U2OS
**p=0.0084
**p=0.0089
**p=0.0098
**p=0.0064
*p=0.0130
*p=0.0138
%20L isoforms
U - 1 5 10 15 Fer-1 (μM)
H2O2
e
Aerolysin +
Ctrl 0 1 5 10 15 Fer-1 (μM)
ZDHHC20
20L
S
pATF2
(T69)
pKAP1
(S473)
ATF2
KAP1
GAPDH
kDa
55
45
34
55
45
78
55
45
78
34
HeLa
****
**
****
****
**p=0.0012
****p<0.0001
% 20L isoforms
U - 1 5 10 15 Fer-1 (μM)
Aerolysin

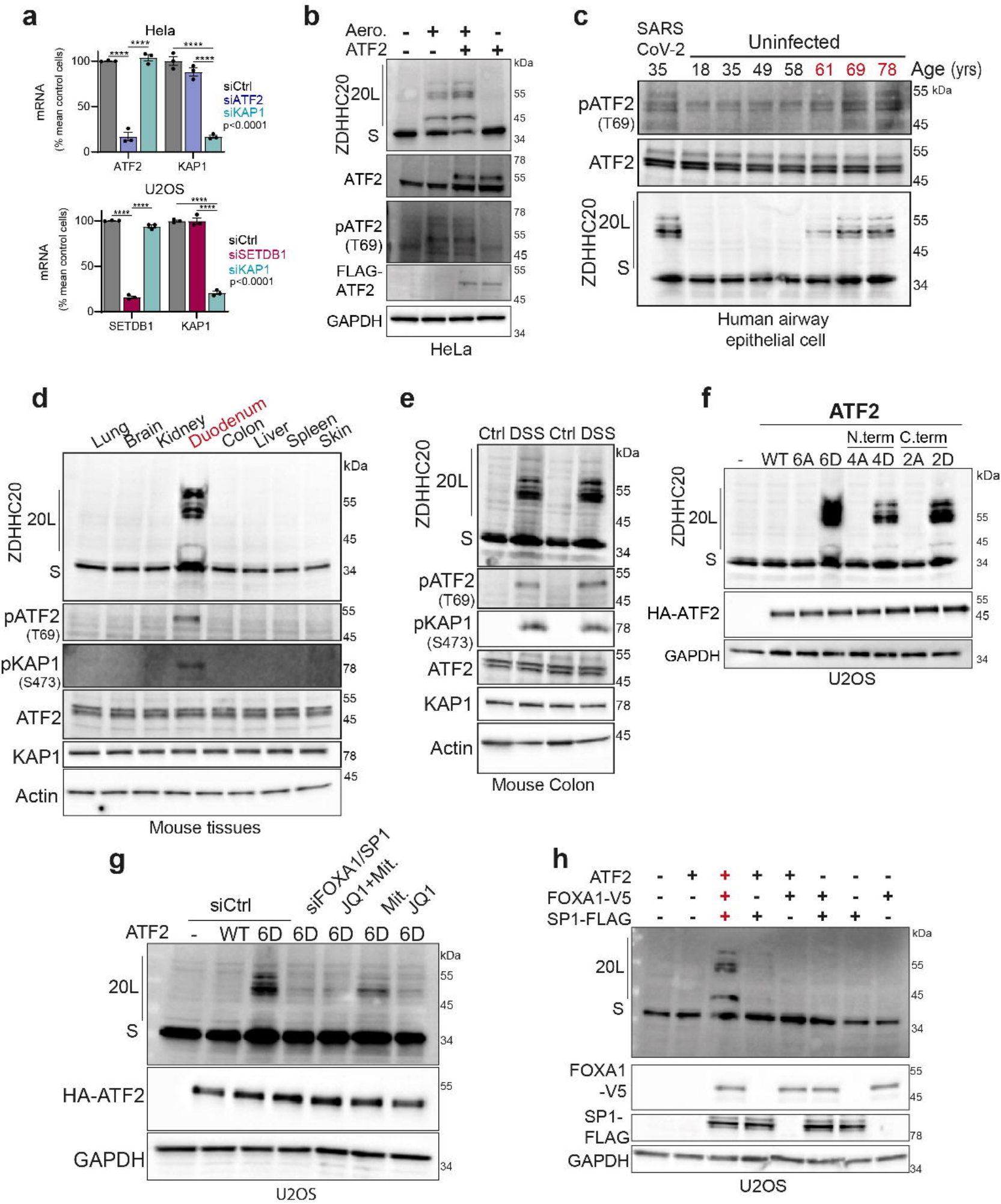
a
Hela
mRNA (% mean control cells)
siCtrl
siATF2
siKAP1
p<0.0001
ATF2
KAP1
U2OS
siCtrl
siSETDB1
siKAP1
p<0.0001
SETDB1
KAP1
b
Aero.
ATF2
ZDHHC20
20L
S
ATF2
pATF2 (T69)
FLAG-ATF2
GAPDH
HeLa
c
SARS CoV-2
Uninfected
35 18 35 49 58 61 69 78 Age (yrs)
pATF2 (T69)
ATF2
ZDHHC20
20L
S
Human airway epithelial cell
d
Lung Brain Kidney Duodenum Colon Liver Spleen Skin
ZDHHC20
20L
S
pATF2 (T69)
pKAP1 (S473)
ATF2
KAP1
Actin
Mouse tissues
e
Ctrl DSS Ctrl DSS
ZDHHC20
20L
S
pATF2 (T69)
pKAP1 (S473)
ATF2
KAP1
Actin
Mouse Colon
f
ATF2
N.term C.term
- WT 6A 6D 4A 4D 2A 2D
ZDHHC20
20L
S
HA-ATF2
GAPDH
U2OS
g
siCtrl
siFOXA1/SP1
JQ1+Mit.
Mit.
JQ1
ATF2 - WT 6D 6D 6D 6D 6D
20L
S
HA-ATF2
GAPDH
U2OS
h
ATF2
FOXA1-V5
SP1-FLAG
20L
S
FOXA1 -V5
SP1-FLAG
GAPDH
U2OS

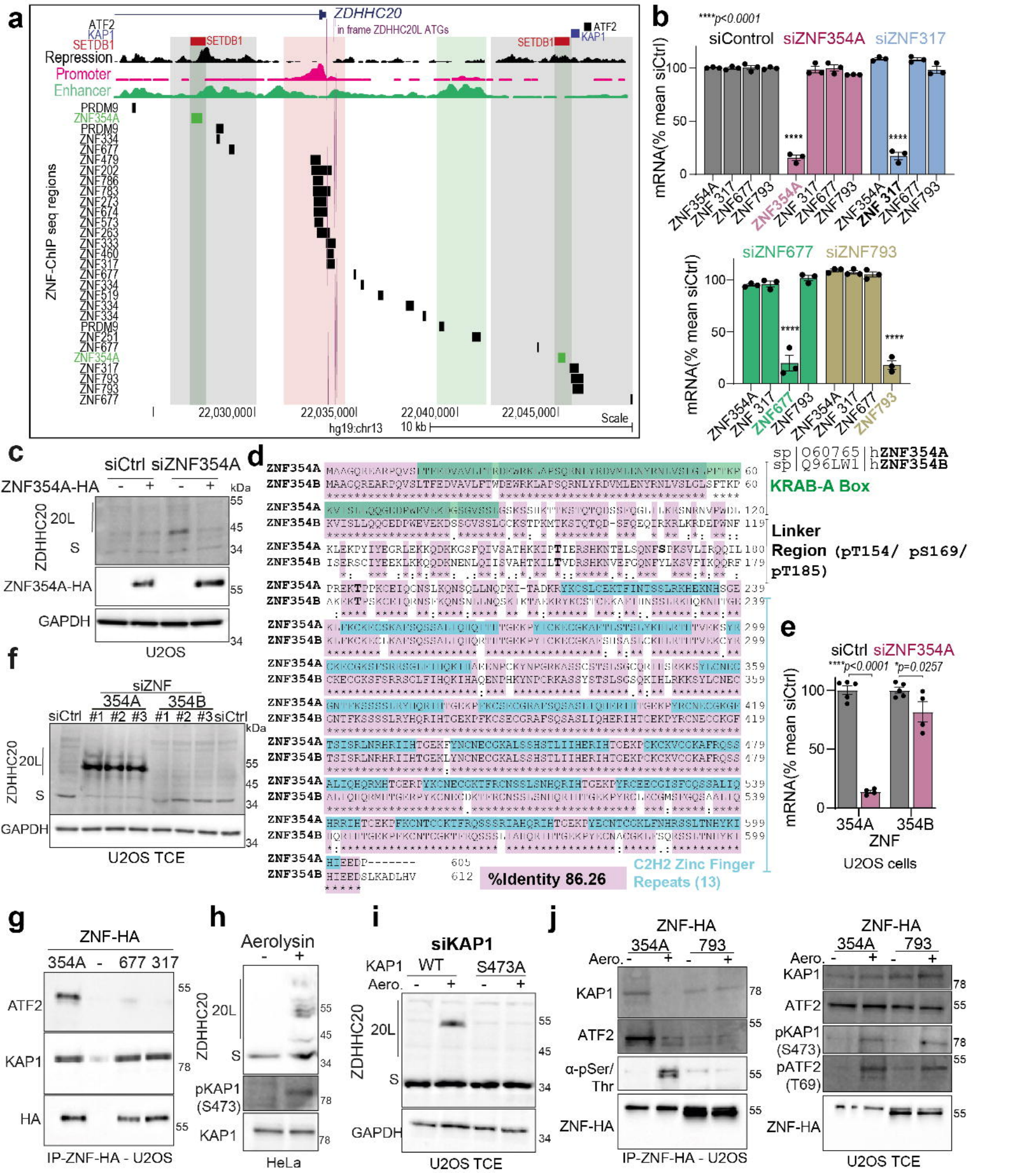
a
ZDHHC20
in frame ZDHHC20L ATGs
ATF2
KAP1
SETDB1
Repression
Promoter
Enhancer
PRDM9
ZNF354A
ZNF-ChIP seq regions
22,030,000
22,035,000
22,040,000
22,045,000
hg19:chr13
10 kb
Scale
b
****p<0.0001
siControl siZNF354A siZNF317
mRNA(% mean siCtrl)
siZNF677 siZNF793
c
siCtrl siZNF354A
ZNF354A-HA
ZDHHC20
20L
S
GAPDH
U2OS
d
sp|O60765|hZNF354A
sp|Q96LW1|hZNF354B
KRAB-A Box
Linker Region (pT154/ pS169/ pT185)
C2H2 Zinc Finger Repeats (13)
%Identity 86.26
e
siCtrl siZNF354A
****p<0.0001 *p=0.0257
mRNA(% mean siCtrl)
354A 354B
ZNF
U2OS cells
f
siZNF
354A 354B
siCtrl #1 #2 #3 #1 #2 #3 siCtrl
ZDHHC20
20L
S
GAPDH
U2OS TCE
g
ZNF-HA
354A - 677 317
ATF2
KAP1
HA
IP-ZNF-HA - U2OS
h
Aerolysin
ZDHHC20
20L
S
pKAP1 (S473)
KAP1
HeLa
i
siKAP1
KAP1 WT S473A
Aero.
ZDHHC20
20L
S
GAPDH
U2OS TCE
j
ZNF-HA
354A 793
Aero.
KAP1
ATF2
α-pSer/ Thr
ZNF-HA
IP-ZNF-HA - U2OS
pKAP1 (S473)
pATF2 (T69)
U2OS TCE

a

Gene	Gene Name	TSS Distance to ZNF354A peak(s)	Seleno- protein	Redox/Sel function	LiftOver (mouse)
GLRX	Glutaredoxin-1	-24514	no	*S*-(de)glutathionylation	-33670
GPX6	Glutathione peroxidase 6	47542	yes	reduction of hydrogen peroxide.	30098
MAT1A	Methionine Adenosyltransferase 1A	-28062, -16487	no	methionine cycle (synthesis GHS)	n.d.
SELB/EEFSEC	Eukaryotic Elongation Factor, Selenocysteine-TRNA Specific	194202	yes	Sec.tRNA elongation factor	152742
SELS	Selenoprotein S	-12179	yes	reductase	-13661
SEPHS2	Selenophosphate Synthetase 2	15386	yes	synthesis of selenophosphate	13010
SEPP1 (SELP)	Selenoprotein P, Plasma, 1	-121809, -52889	yes	Se transporter protein	n.d.
SEPSECS	Sep (O-Phosphoserine) TRNA:Sec (Selenocysteine) TRNA Synthase	-71731	yes	Selenocysteine synthase	-69778
SLC7A11 (XCT)	Solute Carrier Family 7 (Anionic Amino Acid Transporter Light Chain, Xc- System), Member 11	-114554	no	glutamate-cystine antiporter	n.d.
TXNIP	Thioredoxin-interacting protein (TXNIP)	-1296	no	binds and regulates thioredoxin	-1239
TXNRD1	Thioredoxin Reductase 1	72592	yes	thioredoxinreductase	26264
TXNRD3	Thioredoxin Reductase 3	-35307,65219	yes	thioredoxinreductase	n.d.

Retrieved by GREAT / Manual Curated

b

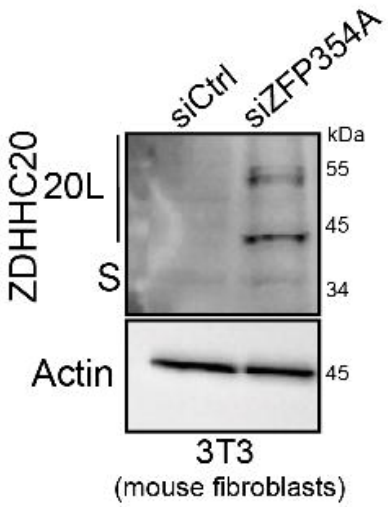

c

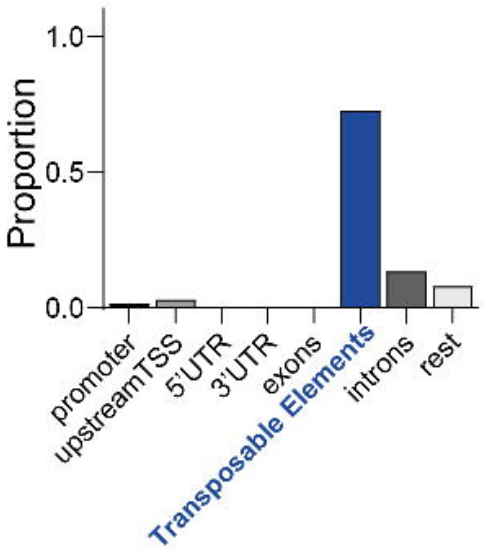

d

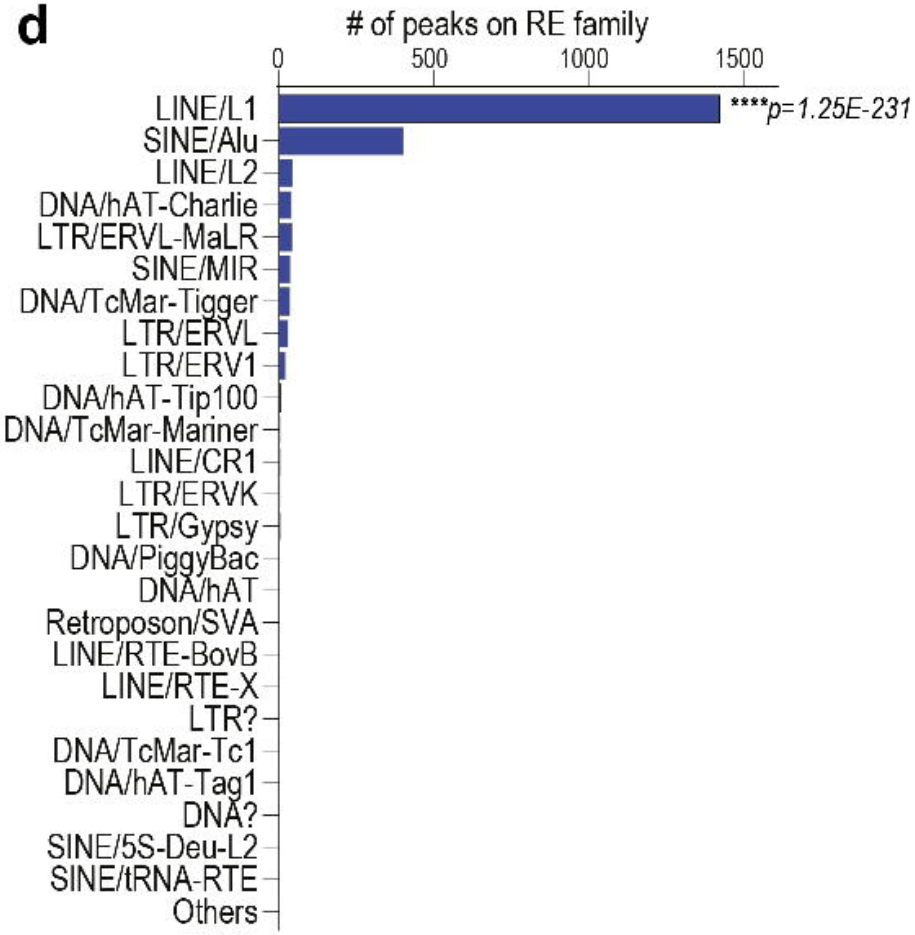

e

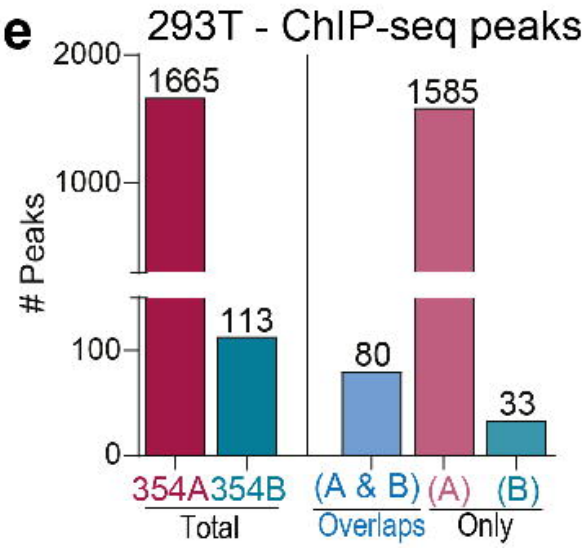

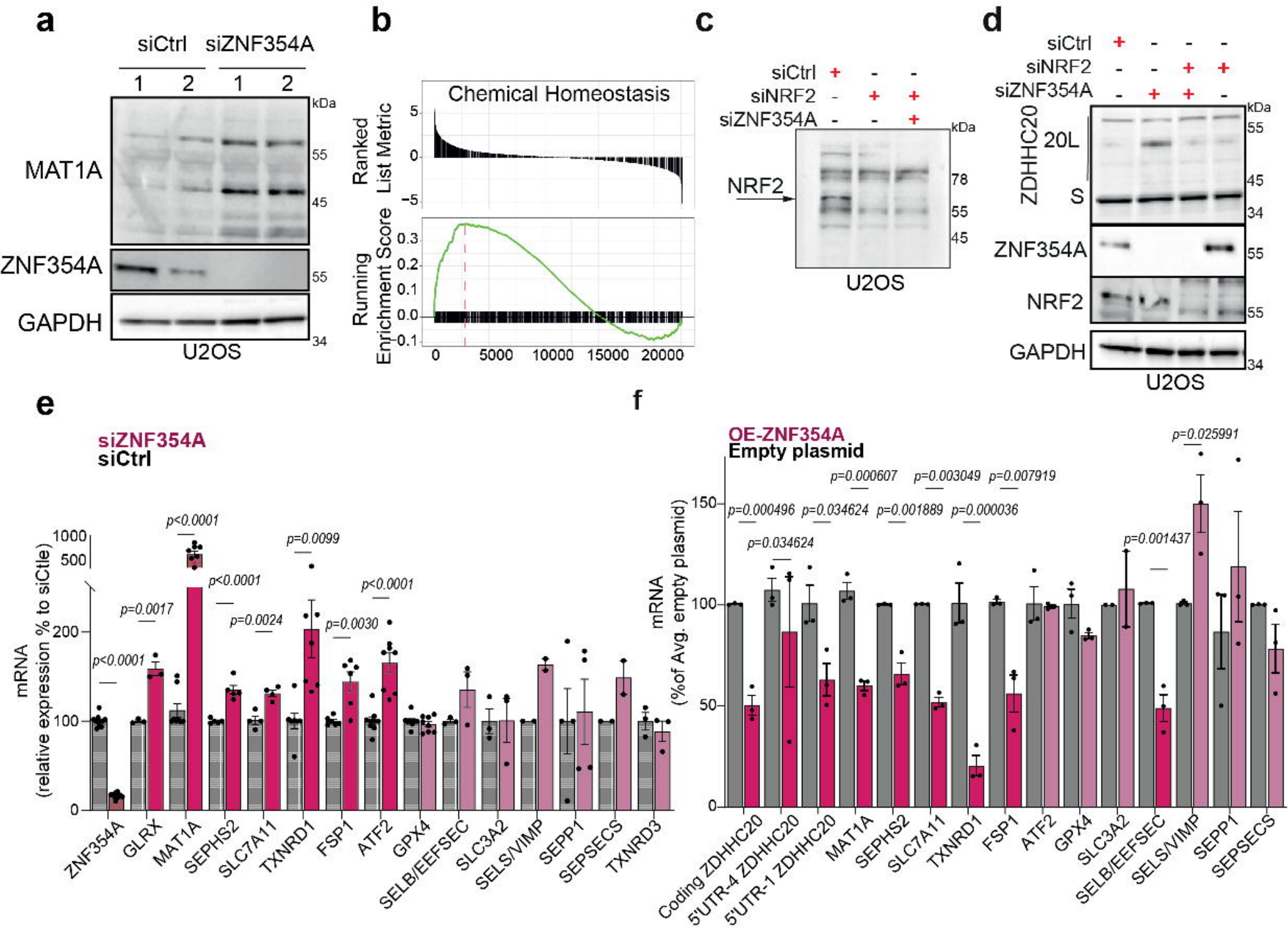
a
siCtrl
siZNF354A
1
2
1
2
kDa
MAT1A
55
45
ZNF354A
55
GAPDH
34
U2OS
b
Chemical Homeostasis
Ranked List Metric
5
0
−5
Running Enrichment Score
0.3
0.2
0.1
0.0
−0.1
0
5000
10000
15000
20000
c
siCtrl
siNRF2
siZNF354A
kDa
NRF2
78
55
45
U2OS
d
siCtrl
siNRF2
siZNF354A
kDa
ZDHHC20
20L
S
55
45
34
ZNF354A
55
NRF2
55
GAPDH
34
U2OS
e
siZNF354A
siCtrl
mRNA (relative expression % to siCtle)
1000
500
200
100
0
p<0.0001
p=0.0017
p<0.0001
p=0.0024
p=0.0099
p=0.0030
p<0.0001
ZNF354A
GLRX
MAT1A
SEPHS2
SLC7A11
TXNRD1
FSP1
ATF2
GPX4
SELB/EEFSEC
SLC3A2
SELS/VIMP
SEPP1
SEPSECS
TXNRD3
f
OE-ZNF354A
Empty plasmid
mRNA (%of Avg. empty plasmid)
150
100
50
0
p=0.000496
p=0.034624
p=0.034624
p=0.000607
p=0.001889
p=0.003049
p=0.000036
p=0.007919
p=0.001437
p=0.025991
Coding ZDHHC20
5'UTR-4 ZDHHC20
5'UTR-1 ZDHHC20
MAT1A
SEPHS2
SLC7A11
TXNRD1
FSP1
ATF2
GPX4
SLC3A2
SELB/EEFSEC
SELS/VIMP
SEPP1
SEPSECS

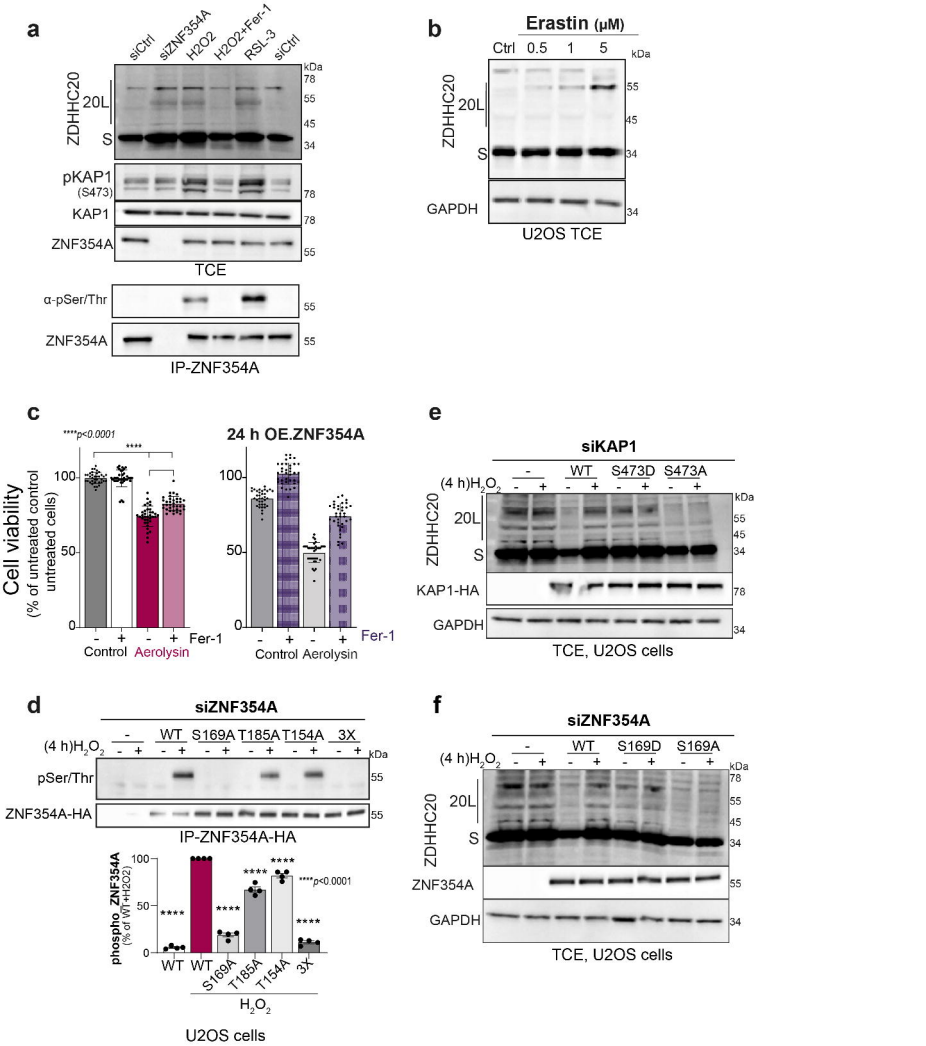
a
siCtrl
siZNF354A
H2O2
H2O2+Fer-1
RSL-3
siCtrl
kDa
ZDHHC20
20L
S
78
55
45
34
pKAP1
(S473)
KAP1
ZNF354A
TCE
α-pSer/Thr
ZNF354A
IP-ZNF354A
b
Erastin (μM)
Ctrl 0.5 1 5
kDa
ZDHHC20
20L
S
GAPDH
U2OS TCE
c
****p<0.0001
24 h OE.ZNF354A
Cell viability
(% of untreated control
untreated cells)
Fer-1
Control Aerolysin
Control Aerolysin
d
siZNF354A
(4 h)H2O2
WT S169A T185A T154A 3X
pSer/Thr
ZNF354A-HA
IP-ZNF354A-HA
phospho_ZNF354A
(% of WT+H2O2)
****p<0.0001
WT WT S169A T185A T154A 3X
H2O2
U2OS cells
e
siKAP1
(4 h)H2O2
WT S473D S473A
ZDHHC20
20L
S
KAP1-HA
GAPDH
TCE, U2OS cells
f
siZNF354A
(4 h)H2O2
WT S169D S169A
ZDHHC20
20L
S
ZNF354A
GAPDH
TCE, U2OS cells

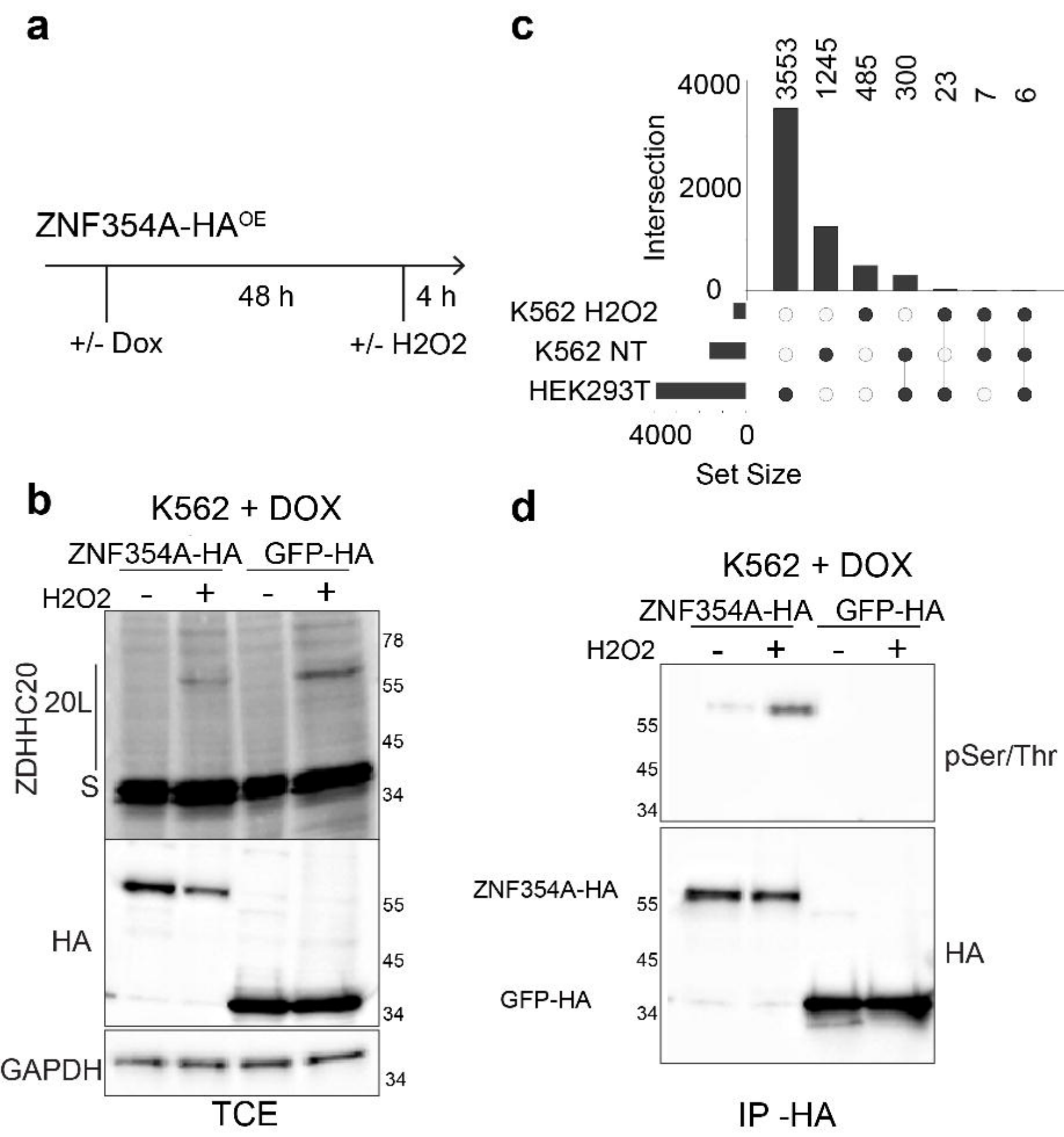
a
ZNF354A-HA^OE
48 h
4 h
+/- Dox
+/- H2O2
c
3553
1245
485
300
23
7
6
4000
2000
0
Intersection
K562 H2O2
K562 NT
HEK293T
4000
0
Set Size
b
K562 + DOX
ZNF354A-HA
GFP-HA
H2O2
-
+
-
+
ZDHHC20
20L
S
78
55
45
34
HA
55
45
34
GAPDH
34
TCE
d
K562 + DOX
ZNF354A-HA
GFP-HA
H2O2
-
+
-
+
55
45
34
pSer/Thr
ZNF354A-HA
55
45
34
HA
GFP-HA
IP -HA

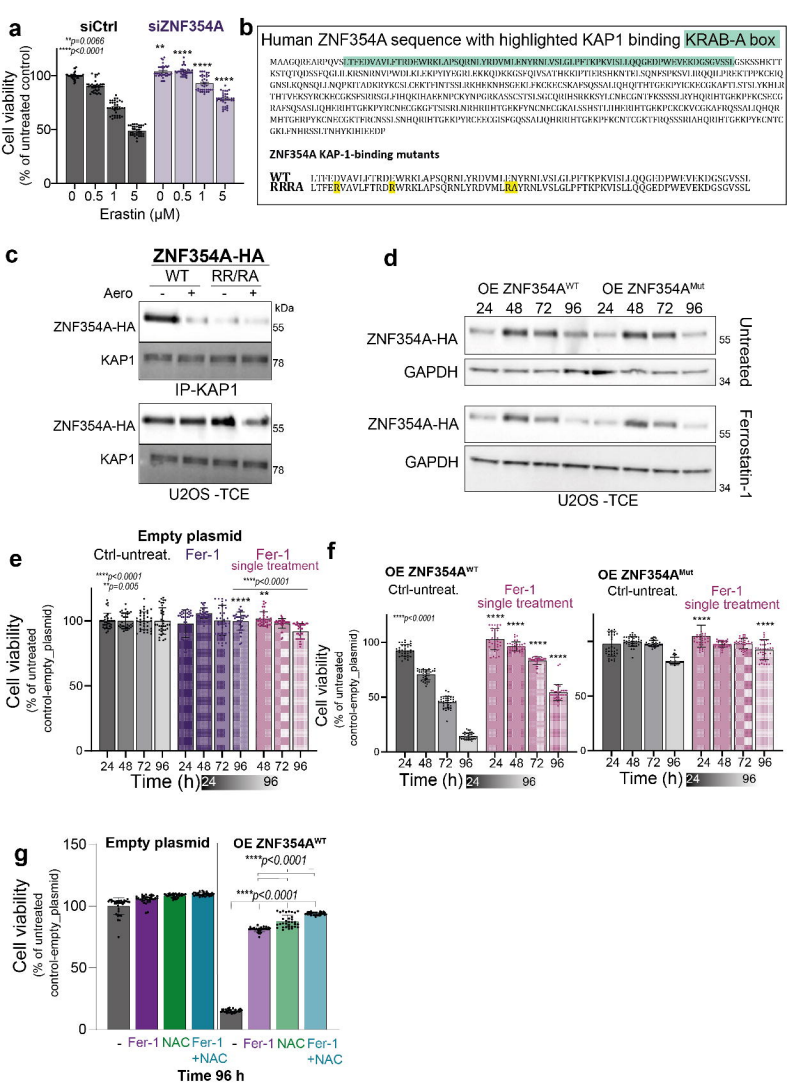
a
siCtrl
siZNF354A
**p=0.0066
****p<0.0001
Cell viability
(% of untreated control)
Erastin (μM)
b
Human ZNF354A sequence with highlighted KAP1 binding KRAB-A box
ZNF354A KAP-1-binding mutants
WT
RRRA
c
ZNF354A-HA
WT
RR/RA
Aero
kDa
ZNF354A-HA
KAP1
IP-KAP1
U2OS -TCE
d
OE ZNF354A^WT
OE ZNF354A^Mut
ZNF354A-HA
GAPDH
Untreated
Ferrostatin-1
U2OS -TCE
e
Empty plasmid
Ctrl-untreat.
Fer-1
Fer-1 single treatment
****p<0.0001
***p<0.005
Cell viability
(% of untreated control-empty_plasmid)
Time (h)
f
OE ZNF354A^WT
OE ZNF354A^Mut
Ctrl-untreat.
Fer-1 single treatment
g
Empty plasmid
OE ZNF354A^WT
****p<0.0001
Fer-1
NAC
Fer-1 +NAC
Time 96 h